# Manufacturing and Fatigue Behavior of Thick Glass/Epoxy Composite Beams

Wen Xiong

A Thesis

In

The Department

Of

Mechanical and Industrial Engineering

Presented in Partial Fulfillment of the Requirements

For the Degree of

Master of Applied Science (Mechanical Engineering) at

Concordia University

Montreal, Quebec, Canada

July 2016

CONCORDIA UNIVERSITY
School of Graduate Studies

This is to certify that the thesis prepared

By: Wen Xiong

Entitled: Manufacturing and Fatigue Behavior of Thick Glass/Epoxy Composite Beams

and submitted in partial fulfillment of the requirements for the degree of

Master of Applied Science (Mechanical Engineering)

complies with the regulations of the University and meets the accepted standards with respect to originality and quality.

Signed by the final examining committee:

Dr. Ramin Sedaghati, Chair

Dr. Martin Pugh, MIE Examiner

Dr. Michelle Nokken, External Examiner

Dr. Suong Van Hoa Supervisor

Approved by _____
Chair of Department or Graduate Program Director

_____
Dean of Faculty

Date July 20, 2016

# Abstract

Fiber-reinforced composite materials have been widely used for manufacturing load-bearing dynamic components in aerospace. One example is the helicopter's main rotor yoke. Yokes need to be rigid and sufficiently flexible to survive many blade flexing and revolutions. To understand and improve the fatigue life of rotor yoke, a flexural fatigue behavior study was done on the thick glass/epoxy laminate with bolted holes through the thickness. 80 plies unidirectional and cross-ply specimens were manufactured by hand lay-up. The effect of debulking process was discussed. A suitable bagging and curing procedure was used to achieve uniform and acceptable thick glass/epoxy laminates for mechanical tests. The unidirectional and cross-ply specimens were tested on a clamped-clamped fatigue bending fixture. For each of the stacking sequences, test specimens were subjected to four deflection levels. All flexural fatigue tests were conducted under displacement control at 3Hz, with an R-ratio of 0.1 (single sided bending). Thermography was used to record the surface temperature increase, focusing on the crack initiation area. A crack was detected by four ways: sound, visual observation, load drop and thermography. Thermography was found to be an effective in-situ delamination detection method. A 20% reduction of initial load was taken as failure. The cross-ply specimens initiated delaminations more easily than unidirectional specimens. However, the cross-ply specimens had slower crack propagation rate. The unidirectional specimens did not initiate delaminations (at same thickness position) but had shear-out cracks (at different thickness positions) at displacements lower than 20mm. The fatigue lives were up to $10^6$ cycles. When subjected to the displacement lower than 21mm, the cross-ply specimens had fatigue life up to $10^6$ cycles. For both stacking sequences, the delamination initiated around the second bolted hole area.

# Acknowledgments

This work is under the framework of the CRIAQ COMP 509-INTL project, entitled “Bell flex beam flappability optimization”. This project is funded and supported by Bell Helicopter Textron Canada Ltd., the Natural Sciences and Engineering Research Council of Canada (NSERC), and the Consortium for Research and Innovation in Aerospace in Quebec (CRIAQ). It is an international collaboration work with Indian Institute of Science. I would like to acknowledge Bell Helicopter for their material support and technique instructions.

I would like to take this opportunity to express my sincere gratitude to my supervisor Prof. Dr. Suong. V. Hoa for his guidance, encouragement and support throughout this work. It is a great honor for me to work with him. His wide knowledge and invaluable advice make this journey easier for me.

I would like to thank Dr. Daniel Rosca, Mr. Heng Wang and all the colleagues in our research group for their assistances, unconditional support and precious friendship.

I would also like to thank the examining committee for reading this thesis and for providing critical comments.

Last but not least, the deepest appreciation is expressed to my parents for their endless love and support throughout my overseas studies as a graduate student.

# Table of Contents

**Chapter 1. Introduction and Literature Review ..... 1**

**1.1. Manufacturing of composite laminates: ..... 1**

1.1.1. Optimal manufacturing process of thick fiber-reinforcement thermoset matrix composite laminates ..... 2

1.1.2. Optimal manufacturing process of thick composite flex beams used in rotorcraft industries ..... 4

**1.2. Fatigue behavior of fiber-reinforced polymer composite (FRC) materials ..... 5**

1.2.1. Fatigue behavior of tapered laminates ..... 7

**1.3. Through-thickness properties characterization ..... 14**

**1.4. Stress distribution of composite laminate due to bolted joints ..... 20**

**1.5. Summary ..... 24**

**1.6. Thesis Motivation and Objective ..... 25**

**Chapter 2. Manufacturing of thick glass/epoxy beams ..... 27**

**2.1. Materials ..... 27**

**2.2. Specimen fabrication ..... 27**

**2.3. Quality control ..... 32**

2.3.1. TGA (Thermo Gravimetric Analysis) and DSC (Differential Scanning Calorimetry) ..... 32

2.3.2. Thickness measurement ..... 35

2.3.3. Fiber volume fraction ..... 35

2.3.4. Void content ..... 37

2.3.5. Results and discussion ..... 40

**2.4. Specimen preparations for flexural fatigue test ..... 45**

**2.5. Summary ..... 47**

**Chapter 3. Flexural Fatigue Test ..... 48**

**3.1. Flexural fatigue test set-up** ..... **48**

**3.2. Results and discussion** ..... **53**

3.2.1. Flexural fatigue behavior of $[0]_{80}$ specimens ..... 56

3.2.1.1 Deflection level 1: 61% ..... 58

3.2.1.2 Deflection level 2: 65% ..... 60

3.2.1.3 Deflection level 3: 70% ..... 63

3.2.1.4 Deflection level 4: 75% ..... 67

3.2.1.5 Discussion ..... 70

3.2.2. Flexural fatigue behavior of $[0/90]_{20s}$ specimens ..... 71

3.2.2.1 Deflection level 1: 45% ..... 73

3.2.2.2 Deflection level 2: 54% ..... 76

3.2.2.3 Deflection level 3: 63% ..... 78

3.2.2.4 Deflection level 4: 72% ..... 81

3.2.2.5 Discussion ..... 84

3.2.3. Failure mode ..... 84

3.2.4. Crack distribution at the damaged section ..... 87

**3.3. Summary** ..... **91**

**Chapter 4. Conclusion** ..... **94**

**Chapter 5. Contribution and Future Work** ..... **96**

**List of papers:** ..... **97**

**Reference:** ..... **98**

# List of Figures

Figure 1.1. Bell M407 Main Rotor Hub [24] ..... 7

Figure 1.2. Configuration of the baseline symmetric laminate investigated in [32] ..... 9

Figure 1.3 Strain-cycle results for a thick $[(\pm 45)3/0n*/027/0n*/(\pm 45)3]$ laminate with n=1,2,4; plies dropped at the surface of 0 deg stack [33] ..... 10

Figure 1.4 Comparison of strain-cycle results for a thick $[(\pm 45)3/02*/027/02*/(\pm 45)3]$ laminate and a thin $[(\pm 45)3/02*/09/02*/(\pm 45)3]$ laminate; 2 plies dropped at the surface of 0 deg stack [33] ..... 10

Figure 1.5 Comparison of strain-cycle results for surface $[(\pm 45)3/02*/027/02*/(\pm 45)3]$ and internal $[(\pm 45)3/09/02*/09/02*/09/(\pm 45)3]$ double ply drops [33] ..... 11

Figure 1.6 Flexbeam specimen cut from a full size rotor hub flexbeam[34] ..... 12

Figure 1.7 Initial delamination at ply-ending 311 and three possible paths of delamination growth [36] ..... 13

Figure 1.8. Fracture surface at the failed section: a) lay-up 0 b)lay-up 0/90 and c) Lay-up QI [38] ..... 16

Figure 1.9. Specimens subjected to different loading conditions[39] ..... 17

Figure 1.10. Unidirectional composite element, (a) loaded along principal material axes and (b) loaded along an off-axis direction[40] ..... 17

Figure 1.11. Failure patterns of woven carbon/epoxy specimens under through-thickness compression at various angles φ [40] ..... 18

Figure 1.12. Failure patterns of unidirectional specimens loaded in through-thickness compression at various angles φ [40] ..... 18

Figure 1.13. Failure modes of fibrous composite mechanical joints: (a) tension failure; (b) shear-out failure and (c) bearing failure [48] ..... 21

Figure 1.14. Shear stress distributions of the composite bolt joint of the $[90_2/0_8]_S$ laminate with initial clamping pressure of (a) 0 (b) 35MPa ..... 23

Figure 1.15. Fatigue life diagrams of the composite bolted joint for the $[90_2/0_8]_S$ laminate with respect to the bolt clamping pressure ..... 23

Figure 2.1. Proposed configuration of the thick flex beam (dimension in inches) ..... 27

Figure 2.2. Photographs of specimen fabrication steps ..... 28

Figure 2.3. Cure cycle of thick E773-S2 glass fiber laminate .....30
Figure 2.4. Locations of obtained test coupons for DSC and TGA .....33
Figure 2.5. TGA test result of a cured specimen .....34
Figure 2.6 Typical DSC test result of a cured specimen .....34
Figure 2.7. Locations of obtained test coupon for resin weight fraction and density test .....37
Figure 2.8. Sartorius balance and density determination kit .....40
Figure 2.9. Schematic drawing of old bagging assembly .....42
Figure 2.10. Resin bleeding condition by using initial bagging assembly .....43
Figure 2.11. Resin bleeding condition by using modified bagging assembly .....43
Figure 2.12. Microscopic image in $50\times$ magnification of the laminate debulking every 8 plies for 10 minutes .....44
Figure 2.13. Microscopic image in $50\times$ magnification of the laminate debulking every 4 plies for 10 minutes .....44
Figure 2.14. Microscopic image in $50\times$ magnification of the laminate debulking every 3 plies for 5 minutes .....45
Figure 2.15. Bagging assembly of buffer pad bonding .....46
Figure 2.16. Cure cycle of adhesive film 163-2M .....46
Figure 3.1. Flexural fatigue test machine with clamped-clamped loading fixture .....48
Figure 3.2. Schematic drawing of specimen at zero displacement (Dimensions in inches) .....50
Figure 3.3. Schematic drawing of specimen at 0.73 inches displacement .....51
Figure 3.4. Typical thermal images of the test specimen at the periods without delamination (left) and with delamination (right) .....55
Figure 3.5. Investigated crack area .....55
Figure 3.6. Sectioning of failed specimen at (a) different X positions and (b) different Y positions .....56
Figure 3.7. Load reduction ratio ($F/F_0$) versus the number of cycles for $[0]_{80}$ specimens .....57
Figure 3.8. Load reduction ratio ($F/F_0$) and temperature increase at 61% deflection level .....59
Figure 3.9. Typical crack caused by the shear-out failure of bolted joint at cross-section of $X3 = 4.05"$ .....59
Figure 3.10. Schematic drawing of shear-out cracks of unidirectional specimen at 61% deflection level .....60
Figure 3.11. Load reduction ratio ($F/F_0$) and temperature increase at 65% deflection level .....62
Figure 3.12. Schematic drawing of shear crack of unidirectional specimen at 65% deflection level .....62
Figure 3.13. The through-thickness distribution of shear-out cracks on each sectioned piece of specimens at 61% and

65% deflection levels ..... 63
Figure 3.14. Load reduction ratio ($F/F_0$) and temperature increase at 70% deflection level ..... 65
Figure 3.15. The load drop at the first delamination for unidirectional laminate at 70% deflection level ..... 66
Figure 3.16. Delamination location on the side surface at 70% deflection level ..... 66
Figure 3.17. Load reduction ratio ($F/F_0$) and temperature increase at 75% deflection level ..... 68
Figure 3.18. The load drop at the first delamination for unidirectional laminate at 75% deflection level ..... 69
Figure 3.19. Crack location on the side surface of specimen tested at 75% deflection level ..... 69
Figure 3.20. Crack propagations at 75% deflection level ..... 70
Figure 3.21. Load reduction ratio ($F/F_0$) versus the number of cycles for $[0/90]_{20s}$ specimens ..... 72
Figure 3.22. Load reduction ratio ($F/F_0$) and temperature increase at 45% deflection level ..... 74
Figure 3.23. Crack location on the side surface of tested specimen at 45% deflection level ..... 74
Figure 3.24. Schematic drawing of the zig-zag shaped failure at the mid-plane of the cross-ply specimen ..... 75
Figure 3.25. Surface crack propagations at 45% deflection level ..... 75
Figure 3.26. Load reduction ratio ($F/F_0$) and temperature increase at 54% deflection level ..... 77
Figure 3.27. Crack location on the side surface of tested specimen at 54% deflection level ..... 77
Figure 3.28. Surface crack propagations at 54% deflection level ..... 78
Figure 3.29. Load reduction ratio ($F/F_0$) and temperature increase at 63% deflection level ..... 79
Figure 3.30. The load drop at the first delamination for cross-ply laminate at 63% deflection level ..... 80
Figure 3.31. Crack location on the side surface of tested specimen at 63% deflection level ..... 80
Figure 3.32. Surface crack propagations at 63% deflection level ..... 81
Figure 3.33. Load reduction ratio ($F/F_0$) and temperature increase at 72% deflection level ..... 82
Figure 3.34. Crack location on the side surface of tested specimen at 72% deflection level ..... 83
Figure 3.35. Surface crack propagations at 72% deflection level ..... 83
Figure 3.36. Shear-out failure mode of unidirectional specimens at 61% and 65% deflection levels ..... 86
Figure 3.37. Digital images of the cracks of $[0]_{80}$ specimen at sections of $Y = 0.75"$ (left) and $X = 0.5"$ (right) ..... 86
Figure 3.38. Microscopic images of the cracks of $[0]_{80}$ specimen on the XZ surface (left) and YZ surface (right) ..... 87
Figure 3.39. Digital images of the cracks of two $[0/90]_{20s}$ specimens at section $Y = 0.75"$ ..... 87
Figure 3.40. Microscopic image of the crack of $[0/90]_{20s}$ specimen ..... 87

Figure 3.41. Crack through-thickness distribution of two unidirectional specimens at 75% deflection level .....89

Figure 3.42. Crack 3D distribution of unidirectional specimen at 75% deflection level .....89

Figure 3.43. Transverse crack through-thickness distribution of cross-ply specimens at 72% deflection level .....90

Figure 3.44. Transverse crack distribution along X direction of two cross-ply specimens at 72% deflection level....90

Figure 3.45. Transverse crack distribution along X direction of cross-ply specimens at 63% deflection level.....91

Figure 3.46. Crack 3D distribution of cross-ply specimen at 72% deflection level.....91

Figure 3.47. Cycles to first crack of $[0]_{80}$ and $[0/90]_{20s}$ test specimens at different displacements .....92

Figure 3.48. Fatigue life diagram of $[0]_{80}$ and $[0/90]_{20s}$ test specimens at different displacements .....93

# List of Tables

Table 2.1. Bill of materials used in thick composite laminate manufacturing .....29

Table 2.2. Quality results of unidirectional and cross-ply thick specimens .....40

Table 3.1. Four displacement deflection levels of $[0]_{80}$ specimens .....52

Table 3.2. Four displacement deflection levels of $[0/90]_{20s}$ specimens .....52

Table 3.3. Summary of fatigue test results .....93

# Chapter 1. Introduction and Literature Review

## 1.1. Manufacturing of composite laminates:

There are many types of composite manufacturing techniques available depending on various product requirements for quality and cost: Hand lay-up, Autoclave curing, Filament winding, Pultrusion, Liquid composite molding and Thermoplastic composite processing. With increasing demand for the composite manufacturing industry, many new techniques have been developed. For aerospace industry, Autoclave processing is the most commonly used technique for high quality products. It combines the hand lay-up or machine lay-up of pre-impregnated laminates with subsequent treatment in an autoclave at elevated temperature and pressure. The whole curing process can be programmed. The high consolidation pressure involved in the autoclave can ensure high fiber volume fraction of the final product, which leads to further improvement in mechanical properties [1]. Additionally, the high-pressure environment facilitates the removal of voids in the part. The presence of voids has a crucial effect on the mechanical properties of finished composite parts, manifested by a reduction in strength and fracture toughness [2].

In recent years, attempts to apply thick composite laminates to structural components in aerospace industry are growing fast. The significant thickness (about 6mm or more) makes the manufacturing process more difficult and the through-thickness properties play more important roles in the performance of the whole structures. The influence of thickness on temperature cannot be neglected. The conventional curing cycle provided by the manufacturer is no longer proper for manufacturing thicker composite parts. In thicker composite laminates, the heat

generation and dissipation are different from those of thin laminates [3]. Due to the low thermal conductivity of the matrix, heat generated in the mid-thickness area cannot be dissipated to the surrounding environment as quickly as heat generated from areas close to the surface. As such, the reactions in all parts of the laminate do not start simultaneously as happens in the thin laminate. Therefore, using conventional curing cycles for thicker laminate may result in temperature overshoot at the center of the laminate. This can lead to matrix degradation when the temperature exceeds the degradation temperature of the matrix, non-uniform cure and consolidation, and it also induces residual thermal stress.

### 1.1.1. **Optimal manufacturing process of thick fiber-reinforcement thermoset matrix composite laminates**

Studies on the curing behaviour of thick thermoset composite laminate mainly concentrate on two aspects: one is the prediction of reaction kinetics in the process such as heat transfer and resin flow. Another issue is considering the evolution of mechanical properties during the reaction, mainly about the thermal residual stresses generated during the curing. The numerical models were developed from one or two-dimensional finite difference analysis to three-dimensional finite element analysis. Bogetti and Gillespie [4] developed a two-dimensional cure simulation analysis of thick thermoset composites and predicted the temperature and degree of cure distributions. Twardowski et al.[5] compared the experimental temperature profiles of a thick graphite/epoxy composite part (>5cm) to the results predicted by a one-dimensional simulation. It was concluded that viscosity never reached low values simultaneously through the thickness in laminates in excess of 10cm. Hojjati and Hoa [6] constructed a model law for curing thermosetting composites based on the dimensionless parameters. It was possible to predict the temperature and degree of cure distributions of a thick

composite. Kim [7] came up with an idea of adding cooling and reheating steps to reduce the temperature overshoot during cure. The simulation was done by the finite difference method (FDM) to predict the temperature distribution in the laminate during the cure. However, the analysis assumed that the temperature distribution in the plane of laminate was uniform and that thermal properties were constant. The neglect of heat transfer in the planar direction may lead to a certain extent of errors. To obtain more accurate results for curing thick laminates, Oh [8] provided a three-dimensional transient heat transfer finite element analysis model for curing a 20mm thick glass/epoxy laminate in autoclave. A comparison for predicting resin pressure at the center of laminate was made between one-dimensional and three-dimensional flow simulation. It showed that one-dimensional flow analysis had a much longer time to complete the consolidation. Because the permeability of a unidirectional prepreg in the fiber direction was about one order larger than that in the transverse direction, the flow in the fiber direction could shorten the consolidation time. The importance of applying three-dimensional simulation model was proved. In this model, the tools and vacuum bag assembly were also considered to get a more comprehensive internal heat generation during the curing process. Young [9] discussed the effect of compacting forces and cure cycles on the consolidation degree for thick composite laminates. Based on achieving the optimal curing cycle of thick composite laminate, Olivier and Cavarero [10] also compared the longitudinal tensile characteristics between thin and thick (31.5mm) carbon/epoxy laminates in order to prove the validity of the optimized cure cycle. The study pointed out that the main variation in longitudinal characteristics is influenced by the experimental conditions, high clamping pressure during the tensile test. Ruiz and Trochu [11] built a model based on Classical laminated Plate Theory (CLT) to predict residual stresses during the curing of composite laminates. The model evaluated the through-thickness strain and

stresses as a function of the thermo-chemical evolution of the material.

### 1.1.2. **Optimal manufacturing process of thick composite flex beams used in rotorcraft industries**

For the manufacturing large and intricate rotorcraft components such as thick composite flex beams/yokes, cavity molding, a process similar to compression molding, is a candidate in real rotorcraft manufacturing industries. In cavity molding process, a platen press is used to apply heat and pressure to rigid tooling and thereby entice the prepreg within to cure into the shape of the confine of an internal cavity. This method can be very effective in solving the difficulties associated with high resin viscosities. However, when attempting to manufacture thick composites with varying cross-sections using cavity molding process, numerous problems need to be considered such as exothermic reactions and exothermal build-up in the center of thick parts, premature curing and degradation of thin parts. Bheemreddy et al. [12] developed a mathematical two-dimensional cure and flow models for glass/epoxy flex beam composite parts manufactured by using cavity molding. Temperature distribution and degree of cure of flex beam had been calculated during cure cycle. Curing of various cross-sections did not occur simultaneously and uniformly. The variation of preform permeabilities and compaction pressure with fiber volume fraction were also simulated. Bheemreddy et al. [13] also expanded their work for three-dimensional application. To optimize the cavity molding process, neural networks based model was developed and integrated with finite element model. Artificial Neural Networks (ANNs), are a family of statistical learning algorithms inspired by the biological nervous system, and are extensively used to solve a wide range of complex scientific engineering problems. ANN can also be trained to provide solutions for non-linear and multi-dimensional problems without knowing problem nature. With this self-organizing

capability, ANN had been applied to composite field. Zhang and Friedrich [14] and Kadi [15] gave reviews about the applications of ANN in composite research field. Rai [16] and Jahhromi et al. [17] applied ANN for composite cure process and rheology modeling. In Jahromi's study, an optimized multi-linear-stage cure cycle was achieved by using ANN.

In industries, the cavity molding is widely used in manufacturing tapered structure. However, from the experience of industry, the damage in thick region caused by the load introduction is more serious than that in the tapered region. In this study, the research focus is on thick laminate in uniform thickness with load introductions.

## 1.2. Fatigue behavior of fiber-reinforced polymer composite (FRC) materials

Once a material is used for the manufacturing of an engineering component, not only the fundamental properties such as the strength and stiffness should be taken into account, but also the question of how long this material will sustain under the fatigue conditions, which is the original concept of life in the engineering field. Since the early 1800s, the reduction of strength and the subsequent failure of materials subjected to the repeated loading have been known as the phenomenon of fatigue. In homogeneous materials, fatigue behavior can be expressed by self-similar single crack growth. The most typical material having that common failure mechanism is metal. The fatigue behavior of composite materials is more complicated and unpredictable due to the internal microstructures, and the anisotropic characteristics in their strength and stiffness. Due to deficiencies in the understanding of fatigue damage mechanisms and fatigue life prediction methodologies for composite materials, composite structures are often overdesigned. The consequent damage of fatigue in composite materials has four basic failure mechanisms: matrix cracking, delamination, fiber breakage and interfacial debonding. The different failure modes are combined with complicated stress fields, the inherent

anisotropies and non-linear behaviors [18]. The fatigue life models are mainly divided into three categories: Fatigue life models, using S-N curves to predict the total fatigue life; Phenomenological based models, describing the reduction of macroscopically observable properties, usually are residual strength or stiffness; Progressive damage models, predicting the evolution of actual damage features, such as matrix cracks or delaminations. To determine fatigue life, there are two common approaches: A) Constant stress cycling results in loss of strength. B) Constant amplitude cycling results in loss of stiffness. The design requirements determine the utilization of each approach. Fatigue behavior under various loading conditions was widely investigated on composite parts with smaller thickness. The prediction methods of the fatigue driven delamination growth had been widely developed [19]. Several standard testing procedures have been developed to characterize the delamination resistance of fiber-reinforced-polymer-matrix composites under fatigue cyclic loads. S. Stelzer et al. [20, 21] developed a standard procedure on mode I delamination fatigue crack growth. A.J.Brunner et al. [22] attempted to develop the mode II in-plane fatigue shear test procedure by using three point bending end notched flexure and two point bending end loaded split in a round robin.

In the aeronautical industry, fiber reinforced composites are beneficial in controlling the inevitable vibration of the aircraft during flights because they are lighter than metals and inherently well-damped. They also have a long fatigue life, even being subjected under stresses close to the static fracture strength. Fiber-reinforced composite materials have been used for manufacturing load-bearing dynamic components in aerospace. One example is the main rotor blade and tail rotor flex beam spar in a helicopter. The rotor blades in helicopter are usually very thin and flexible compared with the wings of conventional aircrafts. The forces acting upon them are greater and more rapidly varying. The yoke is a primary structural component

connecting the blades to the mast as shown in Figure 1.1. Yokes support the rotating loads and the vibration bending loads of flapping blades. Therefore, they need to be rigid and sufficiently flexible. As such the yokes must have long fatigue lives to survive from many blade revolutions. A tapered configuration fabricated by glass fiber or other composite materials meet the requirements [23]. For the fatigue behavior of thicker composite parts, the research work has been mainly on the tapered composite structure, which consists of a thinner part, a ply-drop part and a thicker part.

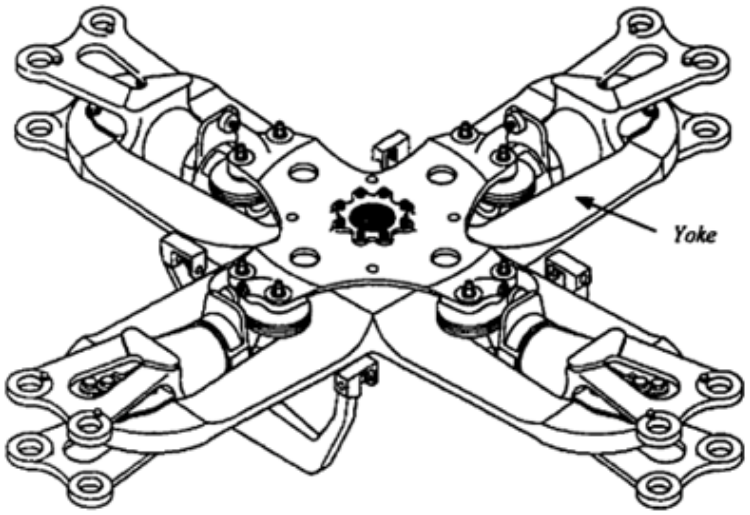


Figure 1.1. Bell M407 Main Rotor Hub [24]

### 1.2.1. **Fatigue behavior of tapered laminates**

In composite structures, the transition in thickness is achieved by terminating or dropping plies either internally or externally. From concern of susceptibility to delamination, internally dropped plies are preferable [25]. The techniques of achieving tapered structure have been widely discussed [26]. A lot of research work had been done on the fatigue behavior

investigation and life prediction of tapered laminates using laboratory test. In earlier work [27, 28], linear tapered laminates were tested under cyclic tension load to investigate delamination. For all tested glass/epoxy and graphite/epoxy laminates, delamination followed a similar pattern. It initiated in the form of a crack behind the resin pocket at the tip of the dropped-ply. As the loading continued, delaminations grew stably through the tapered region toward the thick region. FE model was built to include the initial tension crack, the resin pocket and the delamination propagation. The interlaminar normal stresses showed sharp peaks at the dropped-ply locations and juncture between the thin and tapered regions. The strain energy release rates were calculated by using VCCT (Virtual crack closure technique). Under the tension cyclic loading, the initial delamination growth was almost completely Mode I regardless of the material type. However, when the delaminations grew into the thick region, it became primarily Mode II.

In the ply-drop region, interlaminar stress was commonly shown to be the main reason causing delamination [29-31]. Many structural parameters had effects on delamination at dropped plies. To better understand the interlaminar stress field in laminates with ply drops, two fundamental mechanisms have been identified based on the force and moment equilibrium: the termination effect and the offset effect [32]. The load transfer from the terminated ply group to the continuous plies caused the termination effect. The offset effect was caused by the load redistribution in the outer continuous ply group through an offset in the through-thickness direction from the undropped area to ply-dropped area. This offset in the through thickness direction occurred because the outer continuous plies were angled in the drop-off region. The various ply groups are shown in Figure 1.2. In this study, five structural parameters were investigated: the stiffness of terminated ply group, the location of the terminated ply group in

through-thickness direction, the taper angle, the number of terminated plies and the lay-up sequence of the terminated ply group. The magnitude and distribution of interlaminar stresses varied obviously with those five parameters. By using the trends of the parameters affecting the two fundamental mechanisms, one could identify the configurations or loading conditions that more likely induced delamination because of the higher interlaminar stress. The overall interlaminar stress field could be analyzed through the fundamental mechanisms.

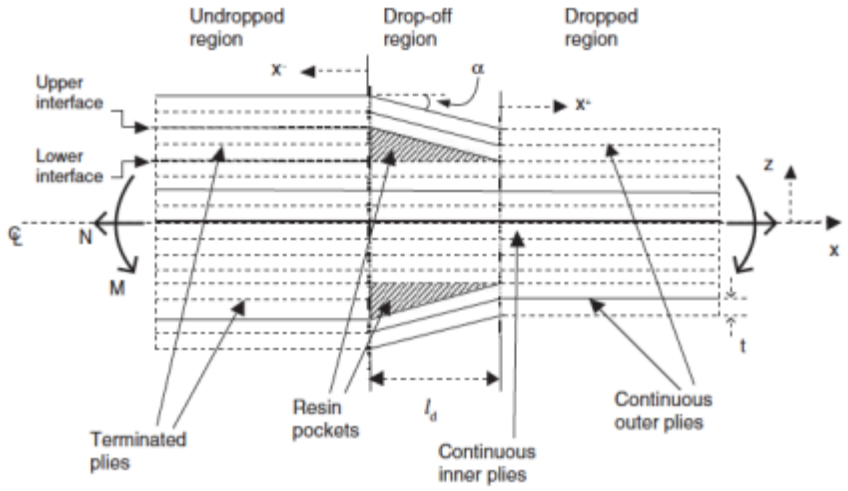


Figure 1.2. Configuration of the baseline symmetric laminate investigated in [32]

Daniel.D et al. compared the delamination resistance of thin and thick composite laminates with ply-drop under fatigue loading [33]. Thin laminates (<4mm) in the base configuration $[\pm 45/0_9/\pm 45]$ were tested under tensile, compressive and reversed fatigue loading. Thick laminates (10-13mm) in the base configuration $[(\pm 45)_3/0_{27}/(\pm 45)_3]$ were tested only under compressive fatigue loading. The dropped plies were 0 degree plies, designated 0*. The $\pm 45$ plies were glass/epoxy, while 0 plies were carbon/epoxy. Maximum compressive strain-cycle curves varied with different parameters: the number of plies drop at one location, overall thickness and ply drop location through thickness. As shown in Figure 1.3-1.5, the influence of

overall thickness is less evident than the others. Laminate with single ply drop showed better performance. The interior drops appeared to perform slightly better than surface drops at higher cycles. The results indicated that delamination at ply drops under fatigue loading could initiate at relatively low applied strain levels. Delaminations and ply drop geometries were also modeled in this study.

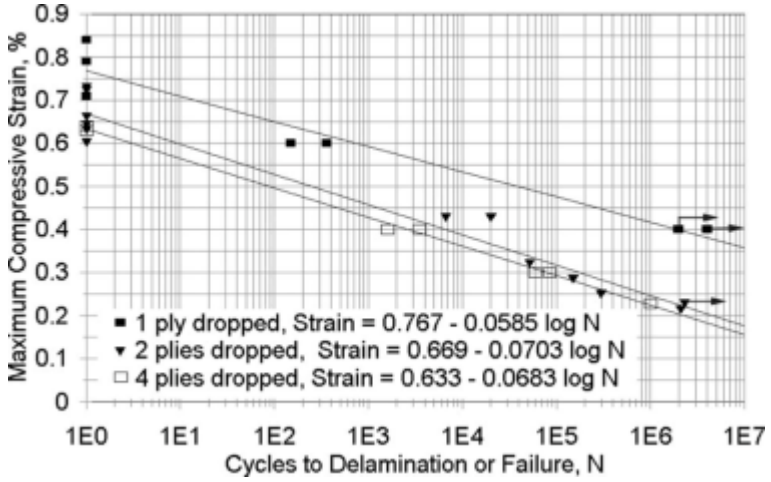


Figure 1.3 Strain-cycle results for a thick $[(\pm 45)_3/0_n^*/0_{27}/0_n^*/(\pm 45)_3]$ laminate with n=1,2,4; plies dropped at the surface of 0 deg stack [33]

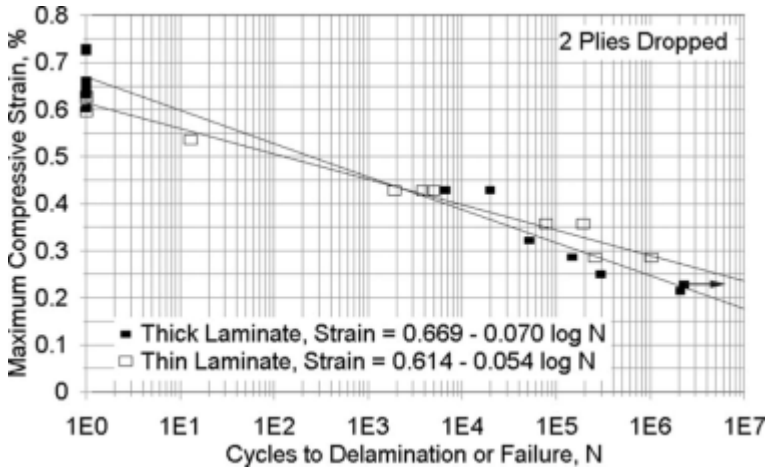


Figure 1.4 Comparison of strain-cycle results for a thick $[(\pm 45)_3/0_2^*/0_{27}/0_2^*/(\pm 45)_3]$ laminate and a thin $[(\pm 45)_3/0_2^*/0_9/0_2^*/(\pm 45)_3]$ laminate; 2 plies dropped at the surface of 0 deg stack [33]

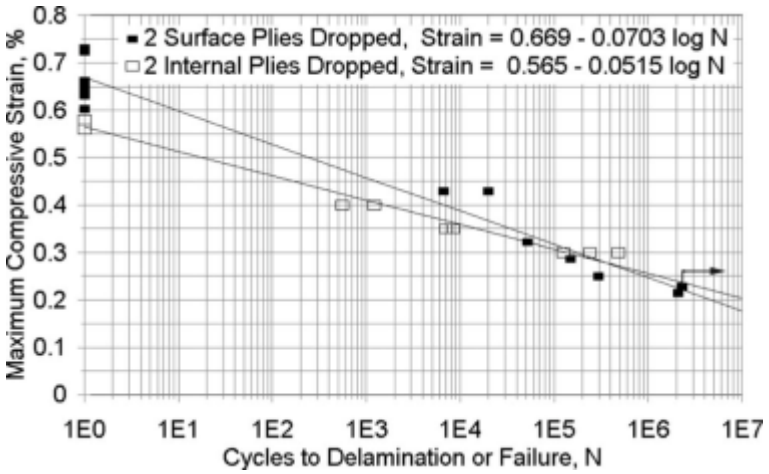


Figure 1.5 Comparison of strain-cycle results for surface $[(\pm 45)_3/0_2^*/0_{27}/0_2^*/(\pm 45)_3]$ and internal $[(\pm 45)_3/0_9/0_2^*/0_9/0_2^*/0_9/(\pm 45)_3]$ double ply drops [33]

To simulate the loading experience of a rotor hub flexbeam in flight, nonlinear tapered glass/epoxy specimens were cut from a full-size helicopter rotor hub (as shown in Figure 1.6) and were tested under combined constant axial tension and cyclic transverse bending conditions [34]. A 2D FE model was created to represent the flexbeam lay-up, geometry and loading conditions. Strain energy releasing rates associated with the delamination growth were calculated for various configurations. Different FE codes were used for the analysis. In nonlinear tapered laminates under combined tension-cyclic bending loading, the delamination started at the ply-drop nearest the surface of the flexbeam. It initially propagated toward the tapered region at the interfaces in a stable manner. As loading continued, some specimens failed catastrophically, delaminating along the entire length. Some specimens continued to delaminate at multiple interfaces without catastrophic failure. The dominating mode had similar behavior as that of linear tapered laminates. Double-cantilever beam tests data and strain energy release rates were combined to generate a curve predicting fatigue failure by unstable delamination.

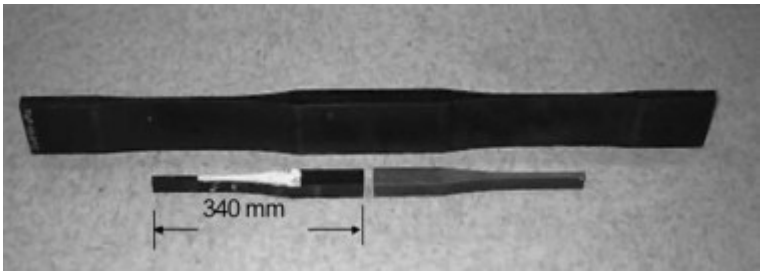


Figure 1.6 Flexbeam specimen cut from a full size rotor hub flexbeam[34]

Murri, G.B. et al. also studied the graphite/glass epoxy hybrid tapered part under the combined axial tension and cyclic transverse bending conditions[35]. Two types of code had been adopted to build a 2D model for simulating delamination growth in the flexbeam: ANSYS and ABAQUS. Results from two models had some variation. There was only one coupon test so not sufficient results were available for comparison. The authors continued this study with improved analysis models and experimental results[36]. Coupon-size specimens were cut from the outboard taper region of the flexbeam from a real tail rotor. Specimens had non-linear taper structure and were symmetric about the midplane. The thick end of the specimen has 129 plies and the thin end had 39 plies. The fatigue test was controlled to a desired maximum surface strain ($\varepsilon_{max}$), with an R-ratio ($\varepsilon_{min}/\varepsilon_{max}$) of approximately R=0.1, it was not a fully-reversed loading. The frequency was 3Hz. The specimens were inserted into the lower grip of the axial-tension bending machine (ATB). The thick end was completely within the fixed bottom grip. The bottom of the tapered region was flush with the top of the lower grip. The initial delamination occurred at the location between the tip of dropped ply nearest surface (ply-drop 311 as shown in Figure 1.7) and the adjacent resin rich area. For the delamination growth, there were three possible paths (as shown in Figure 1.7). Two cracks grew along the interface toward the thick part. One short delamination initiated ahead of the resin pocket along the interface,

grew toward the thin region. The delamination firstly grew along interface bl. This delamination pattern was typical for all tested flexbeam coupons. The finite element models simulated the delamination growth along the primary interfaces and yielded identical strain energy release rate values. The analyzed results suggested that the initial delamination from the resin rich area toward the thick region was dominated by mode II. A fracture-mechanics methodology was used to generate a curve relating the maximum surface strain with fatigue life from the opening of the crack at ply-drop tip to the delamination onset. The required strain energy release rate was from mode II End Notched Flexure tests. The calculation was on the base of assuming the existence of an initial crack at the ply-drop tip. Therefore, the number of cycles causing this initial crack to form was not included in this calculation. In this flexbeam coupon tests, a crack from ply-drop tip without delamination growth was never observed. It was deduced that the matrix cracking and delamination onset happened simultaneously.

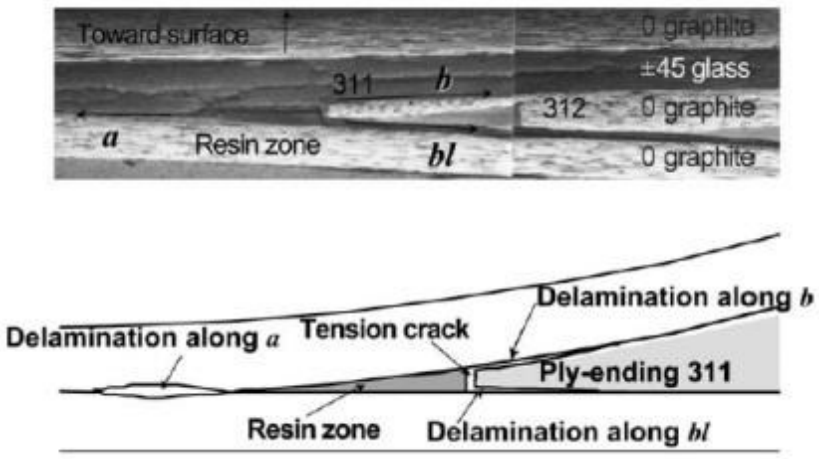


Figure 1.7 Initial delamination at ply-ending 311 and three possible paths of delamination growth [36]

Lalonde did a set of static and fatigue tests under beamwise bending loads on specimens cut out from actual Bell Helicopter M407 main rotor yoke, which was made of laminated

glass/epoxy composite material [24]. Delamination failure of the yoke under static and fatigue loading conditions was investigated both experimentally and analytically. The model was able to predict the location of initial static failure but yielded about 50% error for the fatigue load prediction.

PM Pawar and R Ganguli [37] investigated the effects of three key damage modes in composite helicopter rotor blades on various properties such as stiffness, frequencies, deflection, root forces, root moments and strains. The damage modes discussed included: matrix cracking, debonding/delamination and fiber breakage. The composite rotor blade was modeled as a thin wall composite beam. The change in shear strains measured from various locations of the composite beam increased with the increasing of damage level along the blade length. From the plots of all three damage modes, it was found that the shear strain could be a very useful indicator of damage location and damage level.

From the literature work on the fatigue behaviour investigations on the tapered structure, it was found out that the initial damage occurred at the ply drop locations. The initial delamination growth from the tip of the ply-drop toward the thick region is dominated by mode II.

## 1.3. Through-thickness properties characterization

As the thick composites are used more in structural components applications, the through-thickness (TT) characterization of composite laminate becomes critical. For thin laminates, the through thickness laminate property was assumed to be zero with little loss of accuracy for simplification. However, when it comes to thick laminate, the out-of-plane stress components must be taken into consideration.

S.Vali-shariatpanahi [38] performed two sets of through-thickness tests on three types of

balanced lay-up carbon fiber reinforced polymer laminate with the thickness of 25mm. One set of test was to determine the through-thickness modulus. The other set of test was to determine through-thickness strength of material by performing through-thickness tension. Unidirectional, cross-ply and Quasi-isotropic laminates were made for each set of test. From the stress-strain curve results and failure pattern observation of through-thickness tensile tests, it was concluded that the failure type during tensile test largely depended on the interaction between fiber directions and matrix. This could highly affect the through-thickness material properties of laminate. The failure sections are shown in Figure 1.8. The crack in unidirectional laminate propagates up and down to cause the matrix fracture and final failure. The through-thickness strength of UD laminates is related to the matrix strength and fiber resistance. In 0/90 laminate, failures occur in both 0 and 90 directions as well as in the matrix. The crack grows not only through matrix but it propagates between plies. The crack can find the lower energy path fairly easily through the thickness with few jumps over a couple of plies. It results in lower through-thickness strength of 0/90 laminate compared to the UD laminate. The jump of crack and delaminations are even more obvious in QI laminate. The QI laminates showed the lowest strength.

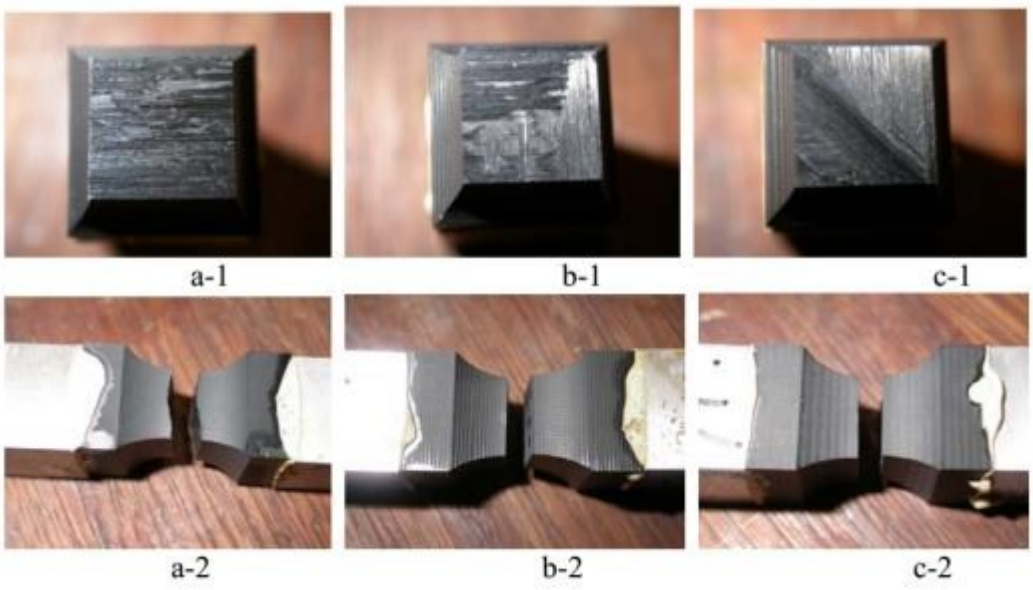


Figure 1.8. Fracture surface at the failed section: a) lay-up 0 b)lay-up 0/90 and c) Lay-up QI [38]

P.M Schubel and I.M Daniel [39] [40] did a series of tests (tension, compression and shear) on characterizing the through-thickness mechanical properties of unidirectional and texile carbon/epoxy laminate with the thickness of 25mm. Waisted, straight-sides and V-notched specimens with designed fixture as shown in Figure 1.9 were used for tensile, compressive and shear load applications respectively. The specimen orientation was characterized by two angles as shown in Figure 1.10, an angle θ between the projection of the loading axis on the 1–2 plane and the 1-axis, and an angle φ between the loading z-axis and the 3-axis. The through-thickness off-axis tensile tests on woven specimens were performed at various angles ($\theta = 0°, \varphi = 0°, 7.5°, 15°, 22.5°, 30°, 45°$). All failures were interlaminar. Similar tests were also conducted in compression with various angles. All failures were interlaminar as shown in Figure 1.11. Figure 1.12 shows the failure patterns of unidirectional laminates subjected to through-thickness compressive loading at various angles φ. The failure plane in these specimens were found to be at $20°$ with the loading direction. Compared with the theoretical

failure predictions by maximum stress, Tsai-Wu and Tsai-Hill criteria, the experimental results had the best fit with a partially interactive criterion developed at Northwestern University (NU) [40]. NU criterion was an interlaminar failure criterion based on maximum strain criterion. This criterion was shown to have excellent agreement with through-thickness experimental results, especially those involving interlaminar shear and compression[41].

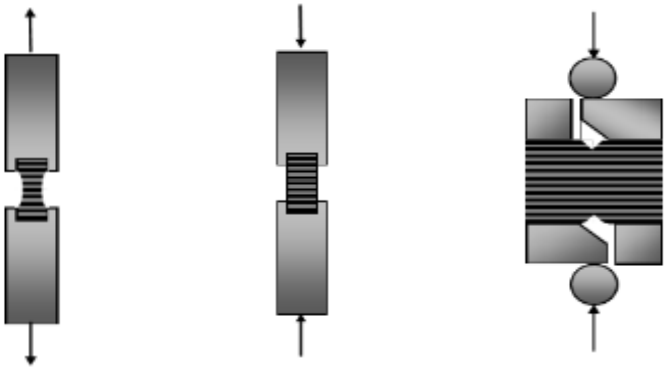

Figure 1.9. Specimens subjected to different loading conditions[39]

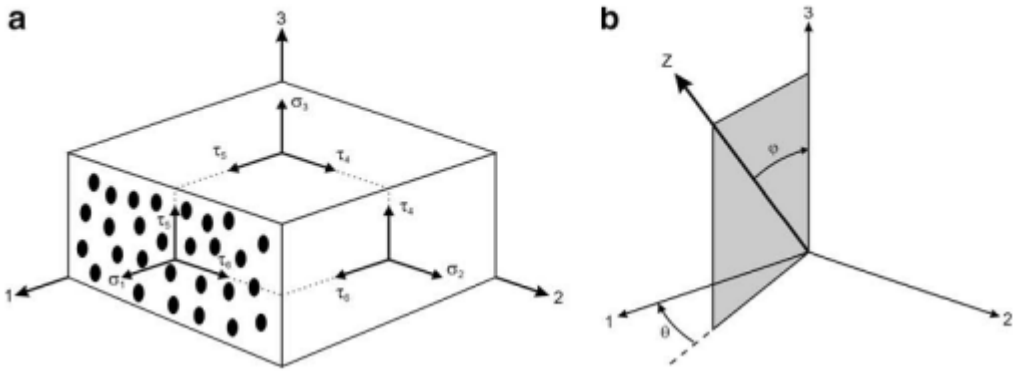


Figure 1.10. Unidirectional composite element, (a) loaded along principal material axes and (b) loaded along an off-axis direction[40]

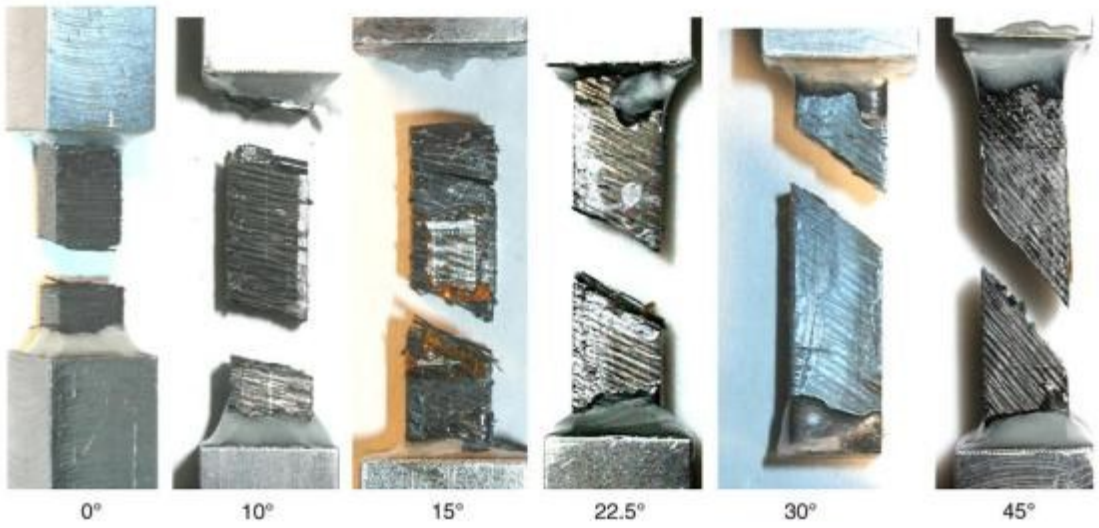


Figure 1.11. Failure patterns of woven carbon/epoxy specimens under through-thickness compression at various angles φ [40]

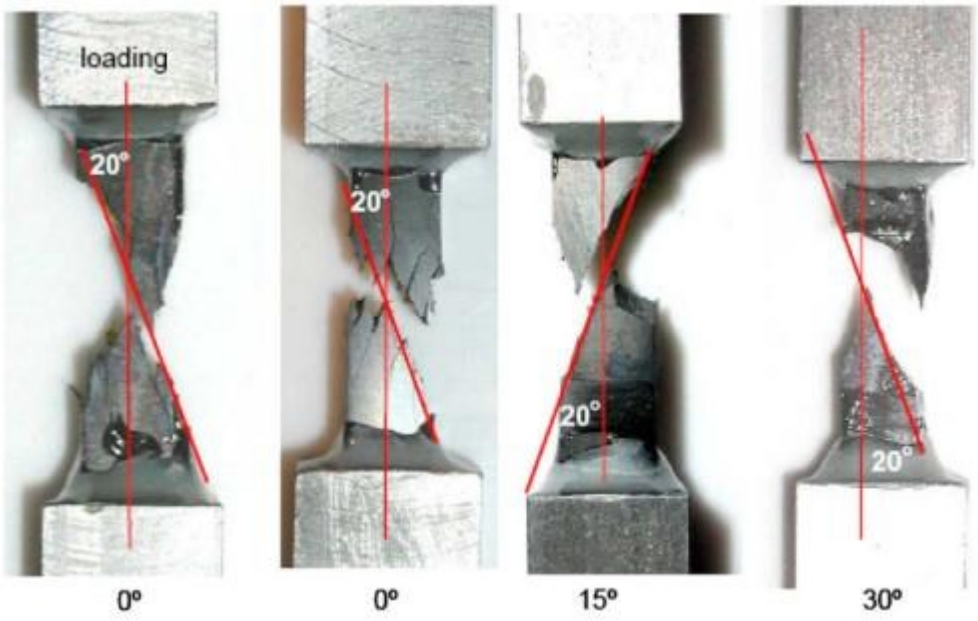


Figure 1.12. Failure patterns of unidirectional specimens loaded in through-thickness compression at various angles φ [40]

NU criterion was also expanded to use in quasi-static and dynamic failure under compression [42]. The dynamic testing was performed under high-strain rate conditions. The

experimental results for both static and dynamic had good agreement with NU criterion. Reuben. A. et al. [43] also did dynamic test on a thick (58mm) E-glass/Vinyl ester laminate to determine the dynamic through-thickness tensile strength by using a split Hopkinson pressure bar (SHPB).

Park and Lee [44] did through-thickness compression tests on carbon/phenolic composite laminates. The study showed two kinds of failure mode after compression test: horizontal splitting and angular splitting. The horizontal splitting was caused by the delamination between plies. The angular splitting was due to the matrix cracking and the fiber breakage. They also showed the effects of thickness on the through-thickness compressive strength (TTCS) of a carbon/phenolic woven composite. The TTCS values were similar for 12mm laminate and 24mm laminates. Moreover, the effect of lay-up angles was also investigated in this study.

To further analyze the TTCS influence factors, Kim et al. [45] measured the TTCS with respect to weave type, stacking sequence and specimen cutting direction. Cubic specimens and cylindrical specimens were both used in the tests. There were three weave types: unidirectional, plain and twill. The stacking sequences for each type of laminate were: $[0]_{8n}$, $[0/90]_{4n}$ and $[-45/0/45/90]_{ns}$. When the specimens were fabricated with unidirectional prepregs, the cross-ply stacking sequence yielded the highest TTCS of about 1.4GPa, while the TTCS of $[0]_{80}$ was only 200MPa. The TTCS of specimen $[-45/0/45/90]_{10s}$ was 1.2GPa. For the other specimens fabricated with woven prepregs, the magnitude of the TTCS of woven composite specimen was about 800MPa regardless of stacking sequence. They were lower than that of the unidirectional specimen. When woven specimen was loaded, the fiber waviness caused large in-plane deformations of each ply. Those deformations could induce relatively higher interlaminar shear stresses than those of the specimens fabricated from the unidirectional prepregs. The failure

modes were also discussed. For unidirectional specimens, $[0]_{80}$ had the lowest TTCS and the transverse matrix cracking of plies was the main failure mechanism. For all other cross-ply and angle-ply specimens with higher TTCS, the cross piles and angle plies impeded the propagation of transverse matrix cracking across the plies. The fiber breakage and interlaminar shear failure caused the final fracture.

Besides the research about the through-thickness (TT) response on uniaxial loading (compression), several authors had also conducted combined compressive and shear loading on off-axis prismatic thick samples [46] or compression and torsion on short hollow cylinder samples [47]. However, the state of stress from those kinds of samples was not uniform and the response showed large dependency on the boundary conditions (such as the contact friction).

## 1.4. Stress distribution of composite laminate due to bolted joints

In aircraft industries, bolted joint is considered to be a common way to connect composite structures. Design of composite joint has received attention due to the complex nature of stress field in the vicinity of joint. A variety of failure modes can occur. The stress concentration near the bolted holes could initiate delamination or other types of damage, which reduce the strength of the structure and induce final failure of the whole part.

There are three basic failure modes associated with composite bolted joint: net-tension, shear-out and bearing, depending on the laminate lay-up and joint geometry as shown in Figure 1.13. Net-tension is the tension failure of matrix and fiber due to the stress concentration. Shear-out failure always results from the shear failures of the matrix and fiber. Bearing mode failure is caused by the contact compressive stresses at the joint boundary. Fiber micro-buckling, matrix cracking, fiber-matrix shearing and delamination may occur due to the compressive stresses.

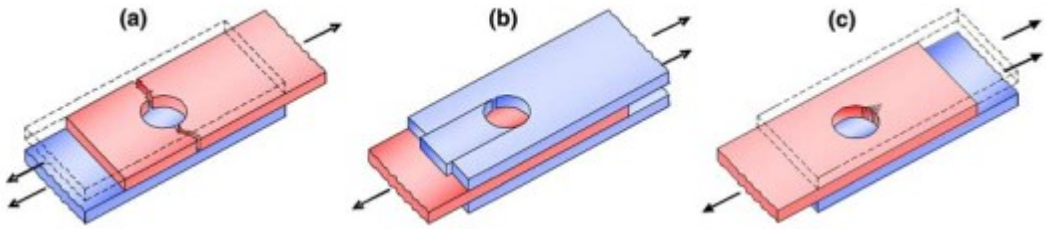


Figure 1.13. Failure modes of fibrous composite mechanical joints: (a) tension failure; (b) shear-out failure and (c) bearing failure [48]

The damage initiation and evolution of laminate with bolted joint configuration depend on a number of factors: clamping torque, washer size and the friction coefficient between washer and the laminate. U.A. Khashaba et al. [49] examined the effects of washer size and tightening torque of bolted joint on the performance of a thin laminate. The experimental results showed that under the same tightening torque, the stiffness of the laminate increased with the decrease of washer size. For various tightening torque, the bearing strength of the bolted holes with same size washers increased with the increasing tightening torque. The failure modes of tested specimens with bolted holes mostly followed similar sequence: delamination between $0°, 90°$ and $\pm 45°$ layers due to their different strains under the compressive bearing load, net-tension failure mode for $90°$ layers, shear-out failure mode for $0°$ layers, catastrophic bearing failure for $\pm 45°$ layers.

The Quasi-isotropic pattern is proposed as one of the most optimal choices of composite bolted joint due to the highest strength. However, this pattern is seldom used under general loads, such as bending, compressive and tensile loads because of the low longitudinal strength and stiffness. Tae Seong Lim et al. [48] investigated the static and fatigue life characteristics of the composite bolted joint for the laminate $[\pm\theta/0_8]_s$ $(\theta = 45°, 60°, 90°)$. When the $[\pm 90°/0_8]_s$

specimens with bolted joints were subjected to zero clamping pressure and 35MPa clamping pressure, the specimen with higher clamping pressure had increasing fatigue life. From the shear stress distribution analysis of the $[90°_2/0_8]_s$ laminate bolted joints as shown in Figure 1.14. The maximum shear stress occurred in the washer area where the through-thickness compression was applied. The fatigue failure was propagated through the shear crack. When the through-thickness compressive stress was applied in the maximum shear stress region, the washer area, the crack opening displacement was reduced by the Poisson's ratio effect. Therefore, the crack propagation was retarded by applying clamping force. For the fatigue tests of $[\pm\theta/0_8]_s$ laminates, it was found that the fatigue stress characteristics were not affected by the outer plies when the same bolt clamping pressure was applied, although their static strengths of were different. The stress versus fatigue life diagram of the bolted joint for the $[90°/0_8]_s$ laminates is shown in Figure 1.15. The major factor of failure was shear crack.

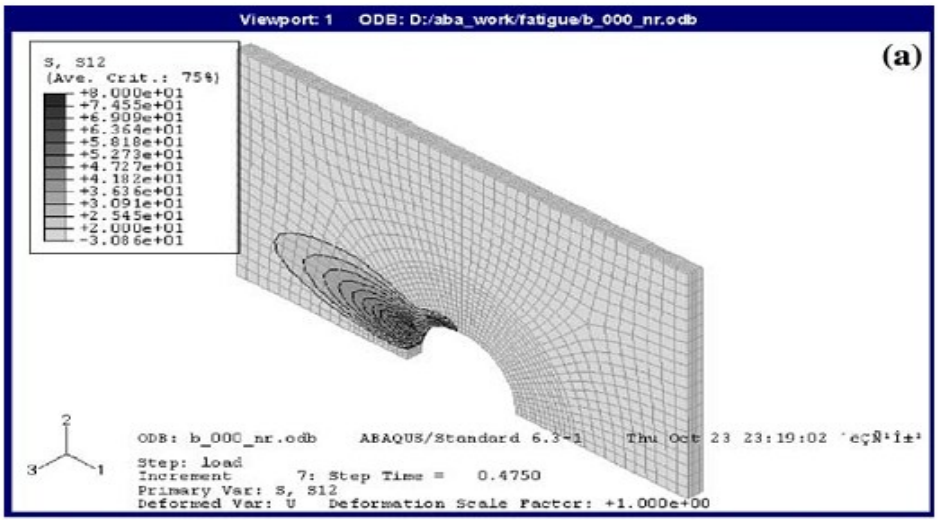

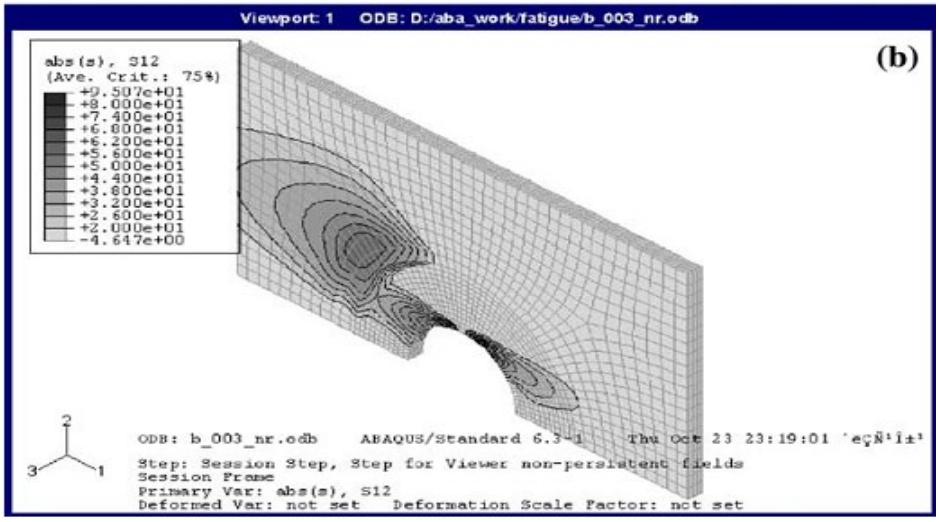


Figure 1.14. Shear stress distributions of the composite bolt joint of the $[90_2/0_8]_S$ laminate with initial clamping pressure of (a) 0 (b) 35MPa

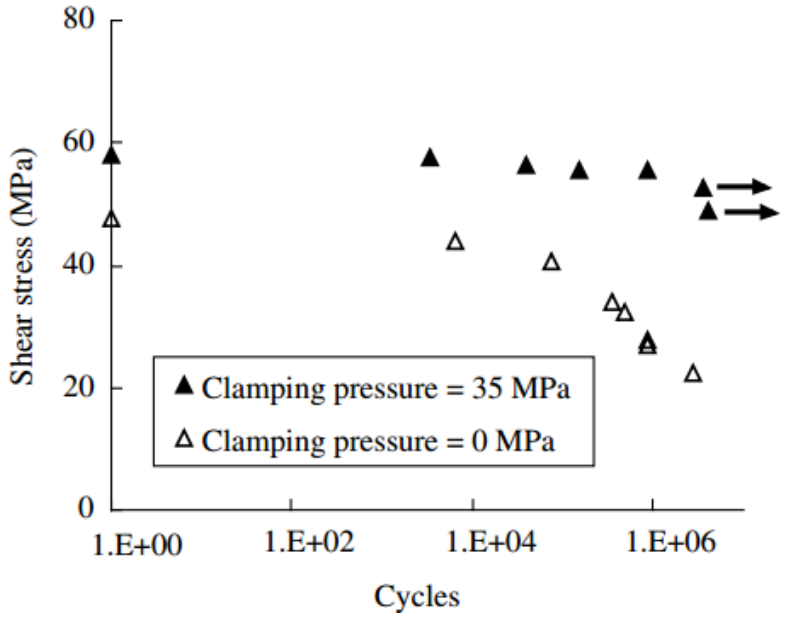


Figure 1.15. Fatigue life diagrams of the composite bolted joint for the $[90_2/0_8]_S$ laminate with respect to the bolt clamping pressure

All the above work on bolted hole effect was focused on thin laminates. For thick laminate,

Gorjipoor Alireza [50, 51] studied the stress and strain distribution around the joint inside the thick laminate. Effects of washer size and clamping torque on the structural behaviour were discussed.

## 1.5. Summary

In the literature, for the fabrication of thick composite laminates, the optimized curing process had been studied. From the experimental aspects, the critical steps during the bagging procedure of thick laminates that differ from that of thin laminates have been less discussed. For the fatigue behavior of thick composite laminate, extensive studies have been carried out about the tapered laminate, mainly concentrated on the application of helicopter rotor blade. When the tapered structure was subjected to the cyclic loadings, the area between the tip of ply-drop and the adjacent resin pocket was more likely to initiate the crack. Delamination propagated along the interface to thick area of the tapered structure laminate. The failure is dominated by mode II. Interlaminar shear stress is the main cause of delamination. However, the fatigue failure mode of the thicker part of the tapered structure was not investigated. The tests of thicker laminate were mostly done on the through-thickness response under various static loading conditions or high strain rate dynamic loading condition. Under the compressive load, the transverse matrix crack is the main failure mode of unidirectional sample. The cross-ply specimens failed by fiber breakage and interlaminar shear. As a common method of assembly, the bolted joint in composite laminate with uniform thickness had become a research focus. The effect of the various parameters of the bolt had been investigated, especially on thin laminate. It has been shown that the clamping force through bolted joint can increase the fatigue life of the specimen. For thicker laminate with bolted holes, the delamination onset and propagation under fatigue loading need to be investigated further.

## 1.6. Thesis Motivation and Objective

From the literature survey, the dropped plies inside the tapered structure give rise to discontinuity and stress concentration, which is the source of delamination onset, leading to premature failure and therefore limiting the useful life. The other is the significant thickness of the laminate. It raises more challenges in both manufacturing and stress analysis. The bolted joints are commonly used to hold a structure in aerospace industry. The introduced bolted load has high potential to initiate the cracks.

Over the past few years, a significant amount of work has been done on the fatigue behavior investigations on tapered composite beams in industry. It was found out that the cracks seem to occur in the thicker part of the beam rather than the thinner part. Both the significant thickness and load introduction are considered to have influences on the fatigue life of the part. In order to understand and provide a good explanation to the observed fatigue behavior of the tapered composite beam, it is of interest to understand the fatigue behavior of thick composite beam with uniform thickness subjected to flexural fatigue loading. Bolted holes are drilled as the load introductions. This project is a group work, which includes three parts: a) temperature distribution and thermal residual stress of thick laminate, b) quasi-static behavior of thick laminate with the effect of bolted holes, c) flexural fatigue behavior of thick laminate with the effect of bolted holes. The overall objective of this project is to predict the fatigue failure of thick composite beams with the load introduction through the bolted holes. Numerical model and experimental works for validating the model are being developed in the meantime. This thesis is focused on the experimental aspect, which includes following objectives:

- To manufacture 80 plies glass/epoxy composite laminates with bolted holes with two

basic stacking sequences $[0]_{80}$ and $[0/90]_{20s}$.

- To observe the flexural fatigue behavior of $[0]_{80}$ and $[0/90]_{20s}$ subjected to clamped-clamped loading condition.
- To provide the information of crack initiation and fatigue life at different deflection levels for numerical studies.

# Chapter 2. Manufacturing of thick glass/epoxy beams

## 2.1. Materials

In this study, CYCOM E773/S-2 prepreg has been used to make the specimens. S-2 glass fiber offers better performance where high strength, high stiffness, high temperature resistance and fatigue resistance are needed.

## 2.2. Specimen fabrication

A particular configuration used in this study was proposed by the industrial partner, as shown in Figure 2.1. The manufacturing process included five steps: Hand lay-up, curing, edge trimming, bolted holes drilling and buffer pad bonding. Figure 2.2 presented the images of sample after each major step.

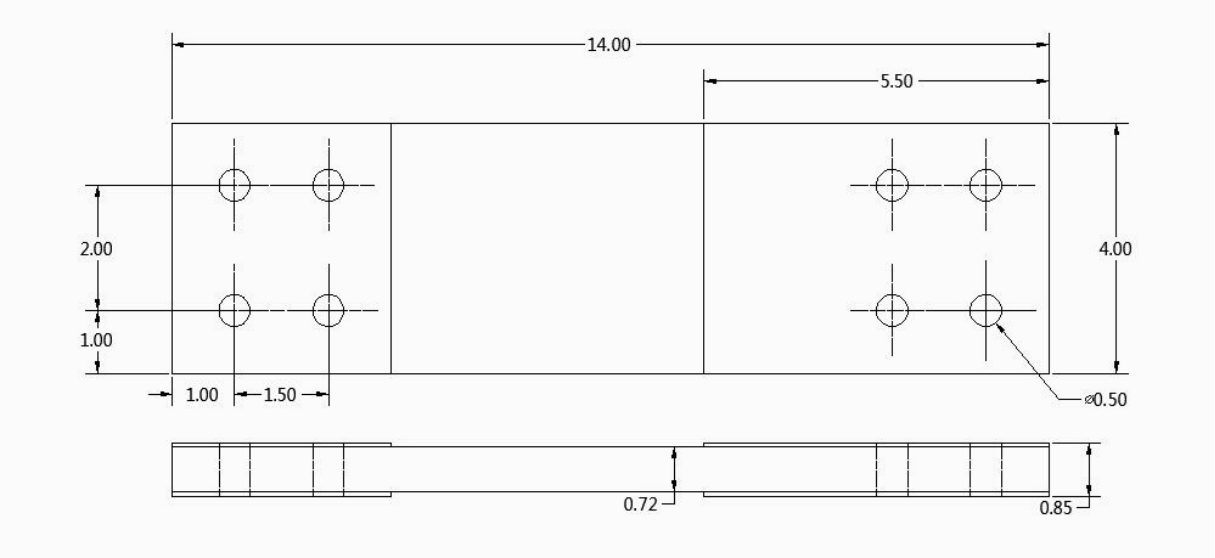


Figure 2.1. Proposed configuration of the thick flex beam (dimension in inches)

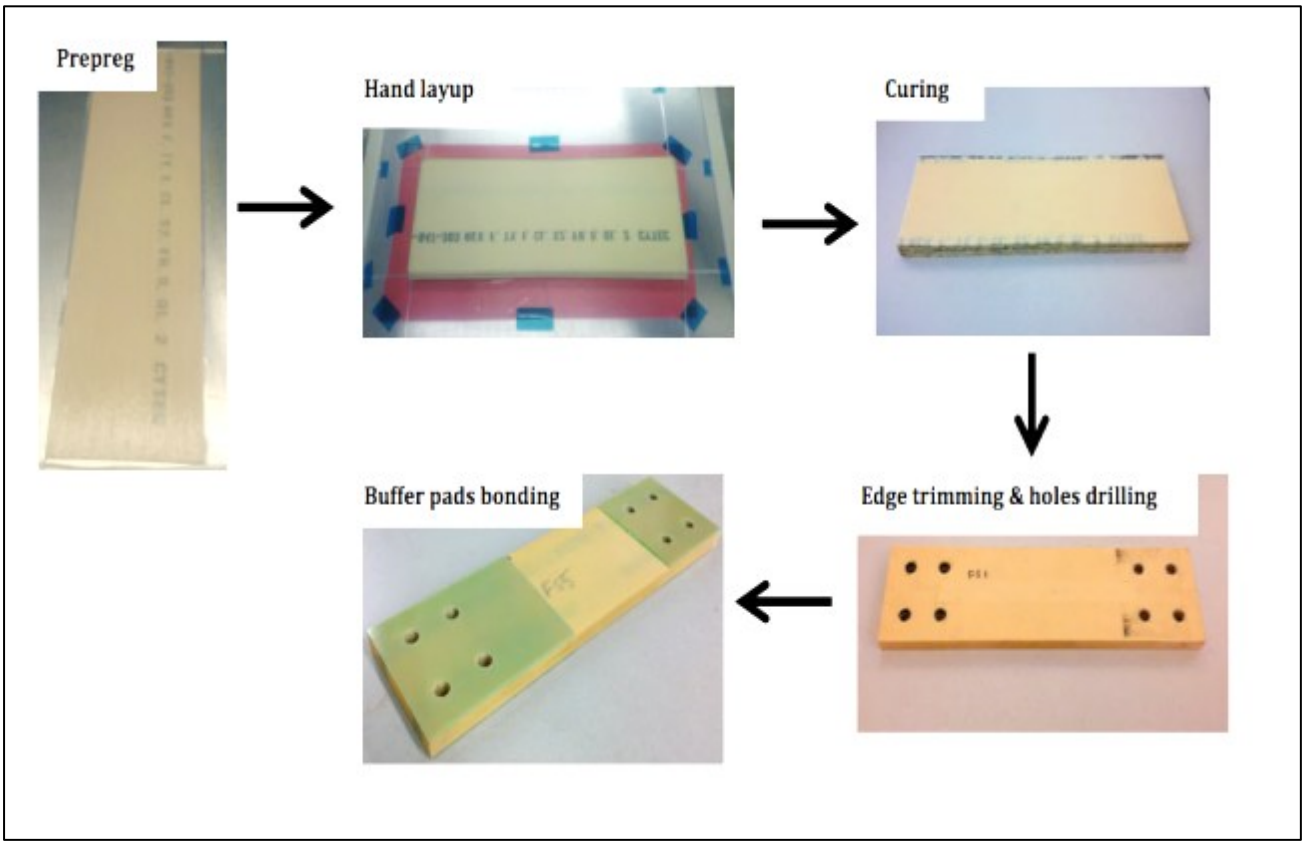


Figure 2.2. Photographs of specimen fabrication steps

In this study, 80 layers of prepregs were used for all specimen configurations. Two types of stacking sequence were fabricated: $[0]_{80}$ and $[0/90]_{20s}$.

The required size of specimen for the mechanical test was 14" × 4". In order to reduce the inaccuracies, larger size laminas of 16" in length by 6" in width were cut for the hand lay-up. The procedure of lay-up is shown as follows:

1) The aluminum tool surface was cleaned by acetone and coated by release agent (770-NC Frekote) beforehand for easy removal of the part after curing.
2) Every 3 plies were debulked under 28 inches Hg vacuum for 5 minutes until finishing the whole stack. The effect of debulking is discussed later.

3) The whole assembly was bagged with the use of materials as shown in Table 2.1.

| Material | Size/Type |
|---|---|
| **Aluminum tool plate** | 6061-T6 Aluminum<br>24”x 20”x ¼” (Length, width, thickness) |
| **Aluminum caul plate** | 6061-T6 Aluminum<br>16”x 6”x ¼” (Length, width, thickness) |
| **Rubber dam** | High Temperature Silicone Rubber Strips<br>(McMASTER-CARR)<br>6.5” x 1” x ½”<br>16.5” x 1” x ½” |
| **Porous releasing film** | AIRTECH 5200B (Blue P3) |
| **Non-porous releasing film** | AIRTECH A4000R |
| **Breather** | AIRTECH Ultra High Temperature 800<br>It is a non-woven blended fiberglass breather. One layer can provide good breathing to 800°F (427°C) |
| **Teflon tape** | AIRTECH Flashbreaker 2 |
| **Vacuum bag sealant tape** | AIRTECH 200Y |
| **Bagging film** | AIRTECH Wrightlon 7400<br>It is designed for the max temperature to 400°F (204°C) |
| **Edge breather** | Glass fabric (McMASTER-CARR) |
| **Bleeding strings** | Glass fabric (ARMTEX) |

Table 2.1. Bill of materials used in thick composite laminate manufacturing

ASC autoclave (up to 800F/300psi) was utilized in this study. Two vacuum pumps are installed in the autoclave. One is to apply necessary compaction pressure to the part and the other is for vacuum state detection. In this curing cycle as shown in Figure 2.3, the laminate was heated up from room temperature to 170 °F at 2 °F/$min$ and pressurized the autoclave to 10 psig. Then the laminate was held for 80 minutes at 170 °F. At the end of the dwell time, the autoclave pressure was raised to 90 pisg. At this point, the vacuum was vented and the laminate temperature was raised to 275 °F at 2 °F/$min$. The laminate was held for 90 minutes at this temperature and then cooled down at 3 °F/$min$. When the maximum temperature was less than 125 °F and the autoclave pressure reduced to ambient, it was defined as "finish" by computer.

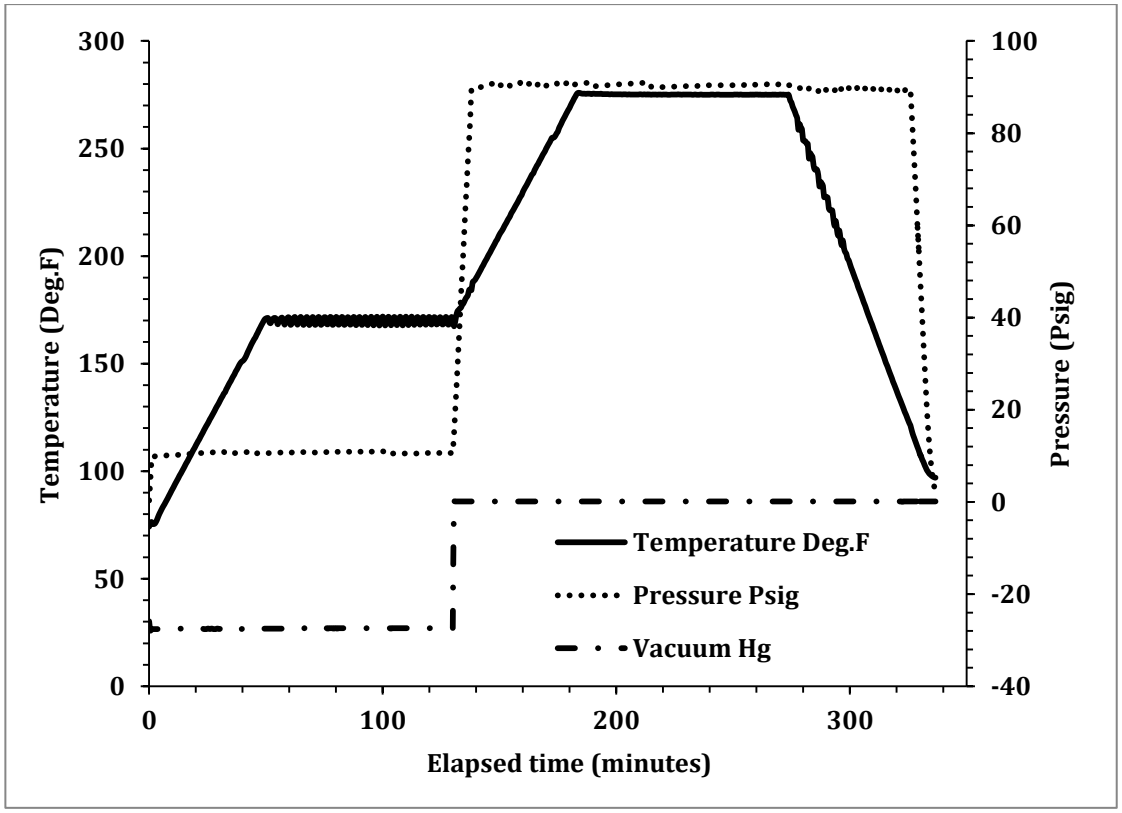


Figure 2.3. Cure cycle of thick E773-S2 glass fiber laminate

During the curing process, the vacuum was vented at the end of the first dwell period. At the same time, the autoclave pressure was raised to 90 psig. This is a common practice for preventing void formation. Upon initial heating, the resin has low viscosity like a liquid. The vapor or gases that may be contained inside the resin intend to grow to bubbles of certain size, depending on the pressure in the resin (surrounding the bubbles). If the pressure is high enough, the vapor of gases cannot form into large bubbles [3]. Continuing pulling vacuum leads to more resin flow out of the laminate. Fiber network becomes load bearing and can have a significant effect on the overall flow behavior of the laminate. One of the consequences is the reduction in resin pressure, which causes voids in the matrix. Therefore, venting the vacuum before raising the temperature and pressure can ensure the resin pressure never drops below the absolute pressure. Several studies had also proved the necessity of this step. F.Y.C. Boey and S.W.Lye [52] indicated that the magnitude of vacuum also had effects on the void content. However, they did not point out the effects of vacuum application duration in curing cycle on the void formation. From that point, Hoda Koushyar [53] compared cure cycles with throughout vacuum and cure cycles with partial vacuum application for manufacturing carbon/epoxy thin laminate. The void content increased significantly when vacuum was kept throughout the cure cycle. This trend was even dominant for center locations of the panel. Furthermore, when the vacuum was held throughout the whole cycle, the density and fibre volume fraction had more variations. For this project, the temperature distribution in 80 plies unidirectional specimen by using the same cure cycle in Figure 2.3 was investigated in[54]. A 30°F temperature overshoot occurred at the center of the laminate. The highest temperature 325 °F was much lower than the matrix degradation temperature 437°F (which was determined in the following TGA test).

Cured specimens were trimmed to the specified size $14" \times 4"$ by using diamond saw with

cooling water. Four bolted holes on each side of sample were drilled by using 1/2" end mill in the machine shop. The qualities of every drilled hole could not ensure to be exactly the same. This may have effects on the mechanical tests.

## 2.3. Quality control

Compared with thin laminates (less than 6mm), thick laminates have more issues. Due to the significant thickness, temperature distribution and resin flow conditions are closely related to cure cycle and bagging procedure, which in turn, affect the sample quality and mechanical behavior. In reality, even for manufacturing samples with the same stacking sequence and procedure, qualities of each sample cannot be guaranteed to be exactly the same. Quality control tests are necessary to ensure that all the samples have acceptable qualities and uniform properties. A series of tests had been done: TGA (Thermo Gravimetric Analysis), DSC (Differential Scanning Calorimetry), thickness measurements, matrix digestion and density measurements.

### 2.3.1. TGA (Thermo Gravimetric Analysis) and DSC (Differential Scanning Calorimetry)

In order to perform TGA (TA Q50) and DSC (TA Q10) tests, the full size specimen was sectioned into small coupons. The locations of the coupons are indicated with squares in

Figure 2.4. For both TGA and DSC test, the required amount of sample for test is no more than 10mg. It was taken from the sectioned coupons by using a hand saw and a scissor. TGA test was carried out on the cured sample to determine the degradation point of the epoxy. Figure 2.5 shows the typical result of TGA test. The degradation started from about 225.30℃. DSC test

was performed to check the degree of cure of the finished part. The test coupon was placed into the aluminum hermetic pan and lid assembly. Heat-cool-heat cycle was chosen as the testing procedure. The second heat line as indicated in Figure 2.6 was used as a baseline. The heat flow profiles of every tested specimen followed the typical trend as shown in Figure 2.6. In the heat flow profile, the first heat line of cured specimen matched very well with the baseline. No exothermic reactions occurred in the first heating period. It means that the sample was fully cured.

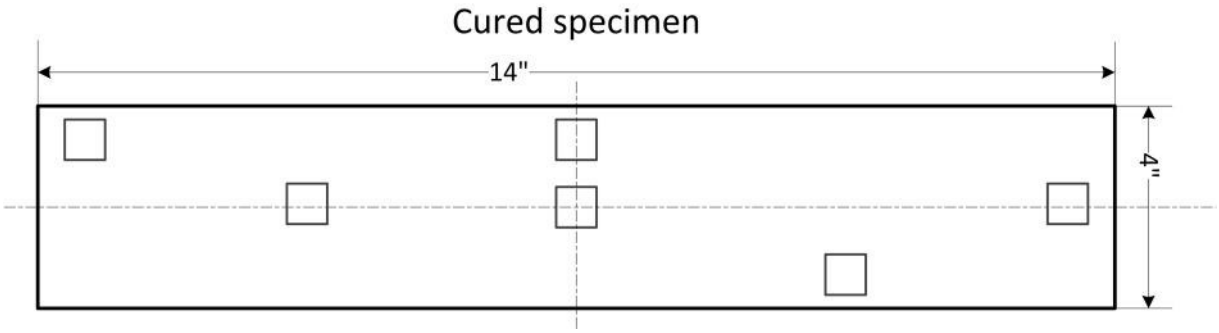


Figure 2.4. Locations of obtained test coupons for DSC and TGA

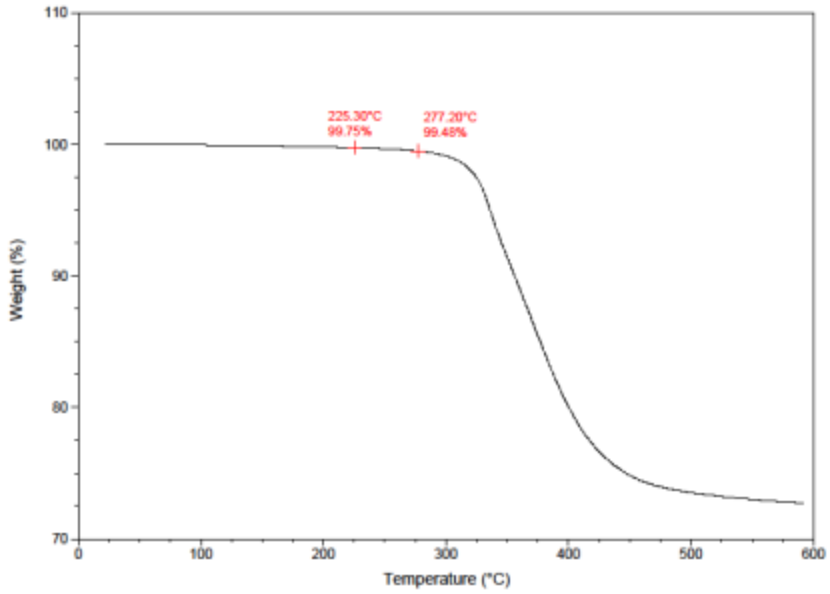


Figure 2.5. TGA test result of a cured specimen

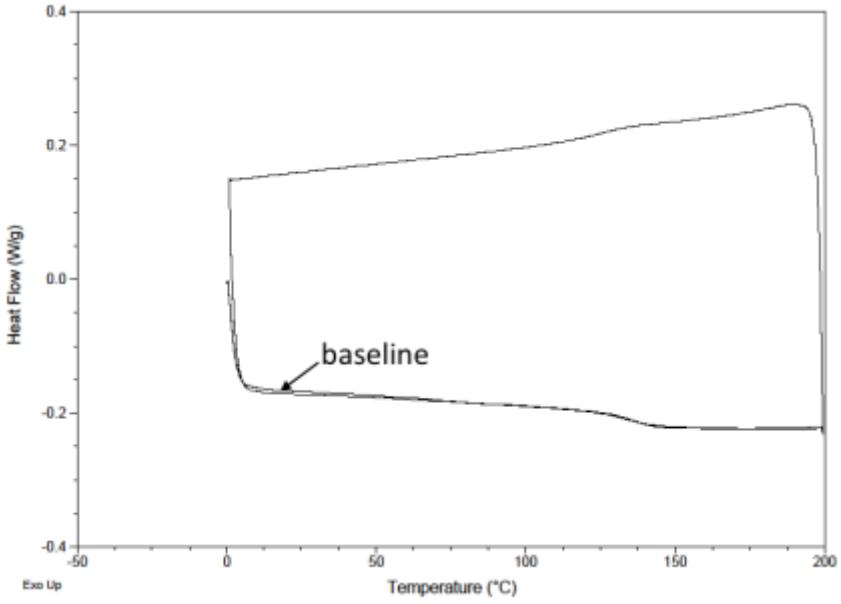


Figure 2.6 Typical DSC test result of a cured specimen

2.3.2. **Thickness measurement**

Micrometers and calipers were used to measure the thickness of different locations throughout the specimen. The average thickness of unidirectional specimens was $0.725" \pm 0.012"$. The result was based on the measurements on 5 specimens. The average thickness of 5 cross-ply specimens was $0.729" \pm 0.010"$. For each specimen, the thicknesses at different locations were measured. The coefficient of variation was between 0.5% to 1.2%.

2.3.3. **Fiber volume fraction**

According to ASTM D2584-11 "Standard Test for Ignition Loss of Cured Reinforced Resins"[55], resin weight content for each sample can be determined. Apparatus used in this test included: porcelain crucible (50ml capacity, Fisherbrand 965-L), electric muffle furnace (Thermolyne 1400 Furnace, up to 1200℃), thermocouple (capable of detecting temperature no more than 800℃), and desiccator. All tests were conducted in the standard laboratory condition. Samples were prepared and tested in the following steps:

1) Crucibles were cleaned by acetone and heated in the muffle furnace at room temperature to 600℃ for 2 hours.
2) The crucibles were cooled down to room temperature in a desiccator and weight to stabilize to nearest 0.1mg.
3) The test coupons were sectioned into size $0.5" \times 0.75"$. They were taken from the trimmed edges as shown in Figure 2.7.
4) Test coupons were cleaned by alcohol and placed inside the desiccator for 1 day before doing the ignition test.

5) The weight of each coupon was indicated by $W_1$. The coupon was heated to 600℃ for 7 hours.
6) The coupon was cooled down to room temperature and placed in a desiccator overnight.
7) The residue weight was indicated as $W_2$.

The ignition loss of each coupon was calculated as follows:

$$\text{Ignition loss, weight \%} = [(W_1-W_2)/W_1]*100$$

Where,

$W_1$ = weight of sample, g, and

$W_2$ = weight of residue, g.

For each manufactured full size specimen, ignition tests were conducted with 6 test coupons taken from various locations of the sample, and the average number was calculated. The fiber volume fraction can be calculated as follows:

$$V\% = (D \times W_{fiber}\%)/[(D \times W_{fiber}\%) + (d \times W_{resin}\%)]$$

Where,

D = density of resin ($1.28 g/cm^3$)

d = density of reinforcement ($2.49\ g/cm^3$)

$W_{resin}\%$ = Ignition loss = resin weight fraction

$W_{fiber}\%$ = 1-$W_{resin}\%$ = fiber weight fraction

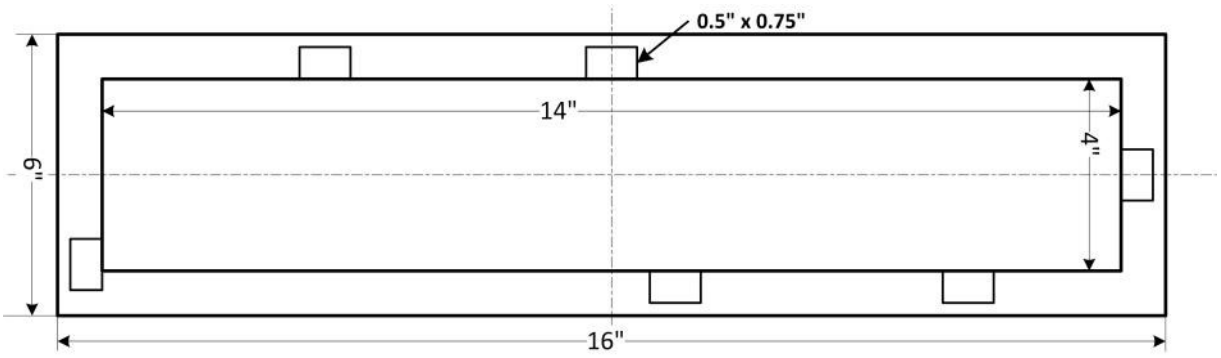


Figure 2.7. Locations of obtained test coupon for resin weight fraction and density test

### 2.3.4. **Void content**

In this study, the void content was determined by the density measurement method. According to ASTM D2734-09 "Standard Test Methods for Void Content of Reinforced Plastics"[56], using the results from ignition test, void content was calculated by comparing theoretical density and measured density. Theoretical density of the composite was calculated as follows:

$$T = 100/(\frac{R}{D} + \frac{r}{d})$$

where:

T = theoretical density

R = resin in composite, weight % (Ignition test)

D = density of resin ($1.28 g/cm^3$)

r = reinforcement in composite, weight % (Ignition test)

d = density of reinforcement ($2.49\ g/cm^3$)

Measured density was determined by Density determination kit. The void content can be calculated as follows:

$$V = 100(T_d - M_d)/T_d$$

where:

V = void content, volume %

$T_d$= theoretical composite density

$M_d$ = measured composite density.

To determine the $M_d$ (measured composite density), Sartorius density determination kit and balance (Max 220g, d=0.1mg) were used, as shown in Figure 2.8. The size of the coupon used in this test was the same as the one in ignition test: $0.5" \times 0.75"$. The Archimedean principle is applied to determine the specific gravity of the solid with this measuring device. When the solid is immersed in a liquid, it is subjected to the force of buoyancy. The value of this force is the same as the weight of the liquid replaced by the volume of the solid. With the balance, the weight of solid in air as well as in water can be measured. To determine the density of composite, distilled water was used as the liquid causing buoyancy. For the accuracy requirement to determine void content in the sample, following errors were considered. First, the density of distilled water varies with the temperature. Second, sample is subjected to air buoyancy while weighting in the air. Third, when sample is immersed in water, the two attached wires in the pan hanger assembly causes additional buoyancy. Fourth, the air bubbles on the sample surface. To correct these errors, the troubleshooting steps proceeded as follows [57]. First, a thermometer was used in the device kit to get the correspond density in actual temperature of water. Second, the air buoyancy was corrected by the following formula:

$$\rho = \frac{W(a)*[\rho(fl)-\rho(a)]}{W(a)-W(fl)} + \rho(a) \text{ [57]}$$

Where,

W(a)= weight of sample in air, g

W(fl)= weight of sample in water, g

$\rho(a)$= density of air, $g/cm^3$

$\rho(fl)$=density of water, $g/cm^3$

Where $\rho(a) = 0.0012 g/cm^3$= Density of air under standard conditions. A volume of 1cm$^3$ of air has a weight of approximately 1.2mg. Third, a correction factor was used in the following formula for the depth of immersing error:

$$\rho = \frac{W(a)*[\rho(fl)-\rho(a)]}{0.99983*[W(a)-W(fl)]} + \rho(a) \text{ [57]}$$

This correction factor is determined exclusively by the geometry of the measuring device set up, so the larger device beaker (76mm) in the kit was used in this test. Fourth, the surface of each test coupon was polished to reduce the surface tension thereby removing the air bubbles on the surface.

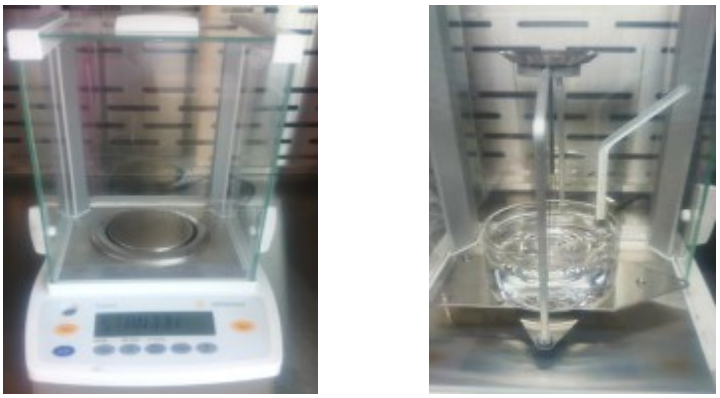

Figure 2.8. Sartorius balance and density determination kit

### 2.3.5. **Results and discussion**

Table 2.2 presents the test results of resin weight fraction and density, the calculated results of fiber volume fraction and void content by applying the fabrication procedure presented in Table 2.2. Each test values of $[0]_{80}$ represented the average of 12 specimens. The test values of $[0/90]_{20s}$ represented the average of 8 specimens. From the table, it is seen that the manufactured specimens had uniform fiber volume fraction, density and low void contents.

| Sample | Resin weight fraction (Experimental results) | Fiber volume fraction (Calculated from experiments) | Measured density (g/cm$^3$) (Experimental results) | Void content (Calculated from experiments) |
|---|---|---|---|---|
| $\mathbf{[0]_{80}}$ | 32.33 ± 0.72% | 51.83 ± 0.8% | 1.90 ± 0.01 | 1.0 ± 0.1% |
| $\mathbf{[0/90]_{20s}}$ | 32.34 ± 0.85% | 51.82 ± 0.98% | 1.89 ± 0.01 | 1.1 ± 0.1% |

Table 2.2. Quality results of unidirectional and cross-ply thick specimens

The quality of the specimen largely depends on the manufacturing procedure, in particular the resin distribution. Poor bagging process leads to more resin loss, which changed the original fibre volume proportion and resulted in higher density. Actually, the total amount of fibre was fixed in the Prepreg. The relative increase in fiber volume fraction due to the significant loss of resin meant that some of the dry fibre could not be sufficiently wet by resin, which may cause voids inside the sample. Non-uniform distribution of resin affected the mechanical property of final product. Two major factors are discussed as follows: resin bleeding and debulking.

First, in the curing process, the four edges of the laminate tend to slope under the combined effects of consolidation pressure and resin flowing. In the meantime, resin could easily flow out under low viscosity circumstance. It led to dry fibres existence and reduced thickness for the finishing part. In order to improve this, rubber dams were used to prevent unexpected resin loss. On the other hand, the prepreg pieces were all cut by hand, the size of every piece was not perfectly the same. There were inevitable small gaps existing between the mold and prepreg stack, which might also be the source of resin bleeding. Figure 2.9 shows the initial bagging assemblies. Figure 2.10 shows the large amount of resin bleeding from the gaps by using this bagging assembly, which resulted in a reduced thickness from 0.73" before curing to 0.60" after curing. Figure 2.11 shows the resin bleeding condition by applying the modified bagging procedure. After measuring the thickness of the cured sample, the amount of resin loss was shown to be unaffected to the final thickness.

Secondly, debulking process is an essential and important step when laying up the prepregs into a significant thickness. This process had two functions, assuring good packing and removing part of the entrapped air before curing. Different debulking periods were applied during the lay-up process. The different void conditions from microscopic images in Figure

2.12 to Figure 2.14 were due to three debulking process: debulked every 8 plies for 10 minutes; debulked every 4 plies for 10 minutes and debulked every 3 plies for 5 minutes. When the debulking process was performed for every 8 plies, it could not achieve the aim of removing entrapped air. Large size of voids still existed. After reducing the member of layers to 3 and 4 for each debulking time, the irregular shape of voids could be effectively removed and also the size of voids decreased significantly. For the consideration of quality and efficiency, in the final procedure, the debulking was performed for every 3 plies for 5 minutes. It was investigated that the large size voids had a detrimental effect on the static flexural and flexural fatigue failure of unidirectional carbon fiber composite [58].

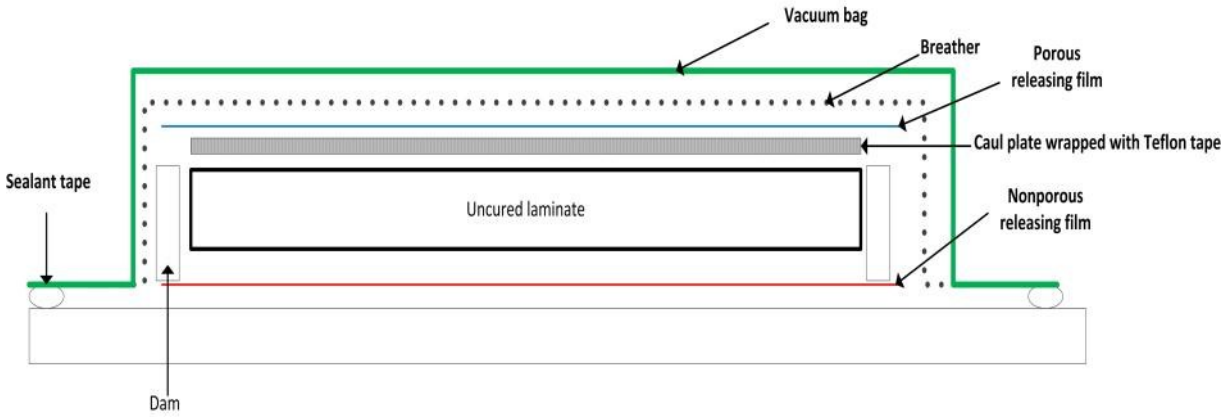


Figure 2.9. Schematic drawing of old bagging assembly

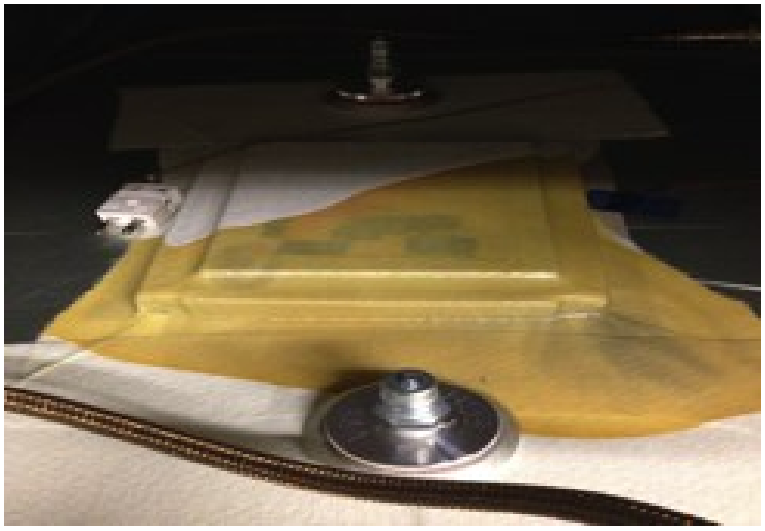

Figure 2.10. Resin bleeding condition by using initial bagging assembly

Figure 2.11. Resin bleeding condition by using modified bagging assembly

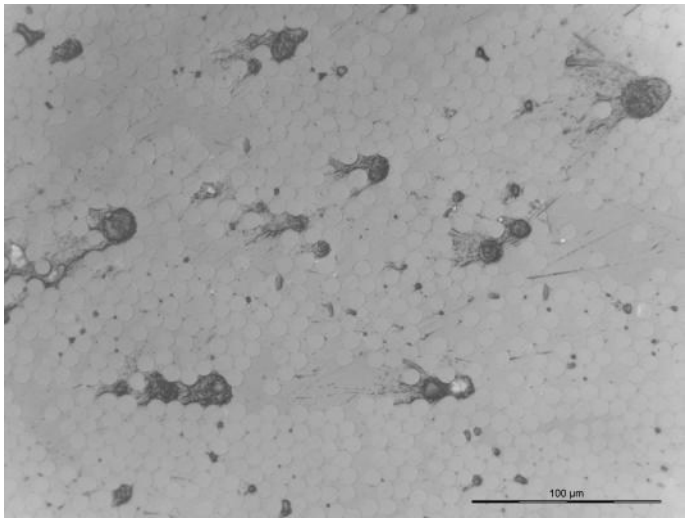


Figure 2.12. Microscopic image in $50\times$ magnification of the laminate debulking every 8 plies for 10 minutes

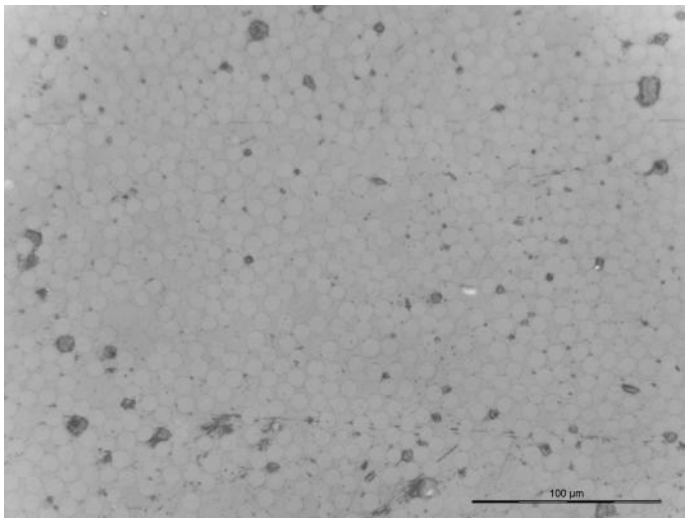


Figure 2.13. Microscopic image in $50\times$ magnification of the laminate debulking every 4 plies for 10 minutes

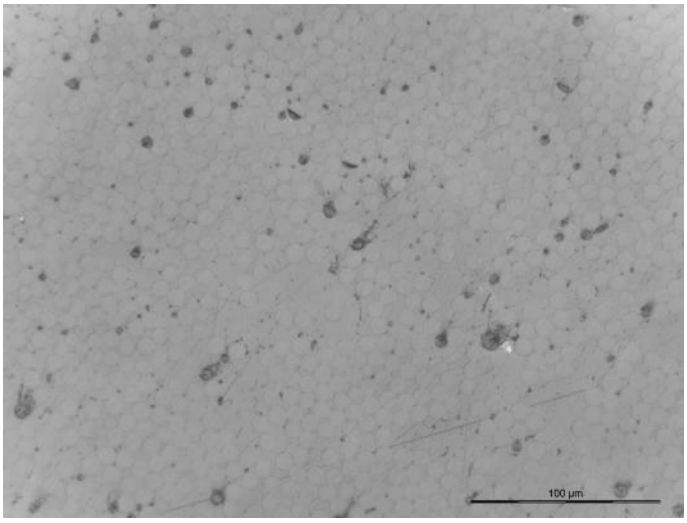


Figure 2.14. Microscopic image in $50\times$ magnification of the laminate debulking every 3 plies for 5 minutes

## 2.4. Specimen preparations for flexural fatigue test

In order to reduce the stress concentrations at the grips on the fatigue test machine, buffer pads were bonded. At the fixed end, the length of buffer pads on the top and bottom surfaces is $5.5"$. At the loaded end, the length is $3.5"$.

Materials and tools used in the buffer pad bonding process include the following: 120 grit sand paper, electric sheet sander, 3M Scotch-Weld Structural Adhesive Film AF 163-2M, ultra high temperature grade G-7 Garolite sheet ($\frac{1}{16}"$ thick), diamond saw, bagging materials and films are the same as in hand lay-up procedure. G-7 tab and adhesive film were cut into sizes of $5.5" \times 4"$ and $3.5" \times 4"$. The sheet sander with a 120 grit sand paper was used to roughen the areas on the sample and the tabs that were to be bonded. The surfaces were wiped cleaned with alcohol and allowed to thoroughly air dry. Then the adhesive film was applied onto the sample surface and the G-7 tabs were placed on the adhesive film. The whole assembly was bagged as indicated in Figure 2.15 and cured with the cycle shown in Figure 2.16. The bonding

performance of buffer pads may have influence on when they will break during the bending test. The hole drilling through buffer pads followed the same procedure as discussed previously.

Before performing the fatigue test, two side surfaces of the specimen were painted in white color for better observation of cracks.

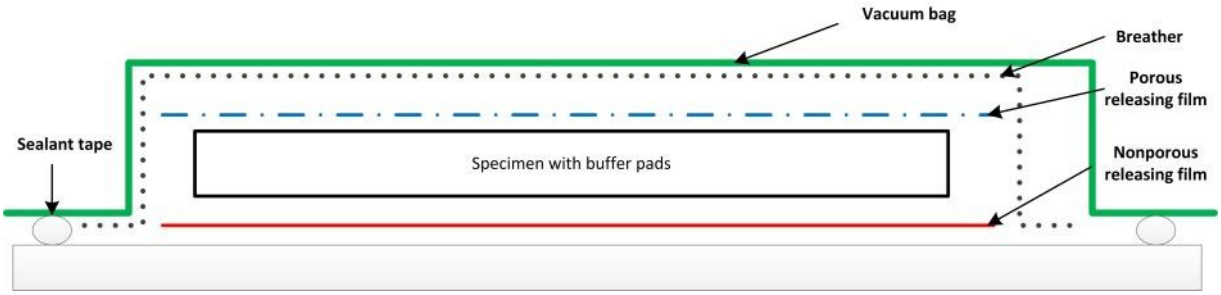


Figure 2.15. Bagging assembly of buffer pad bonding

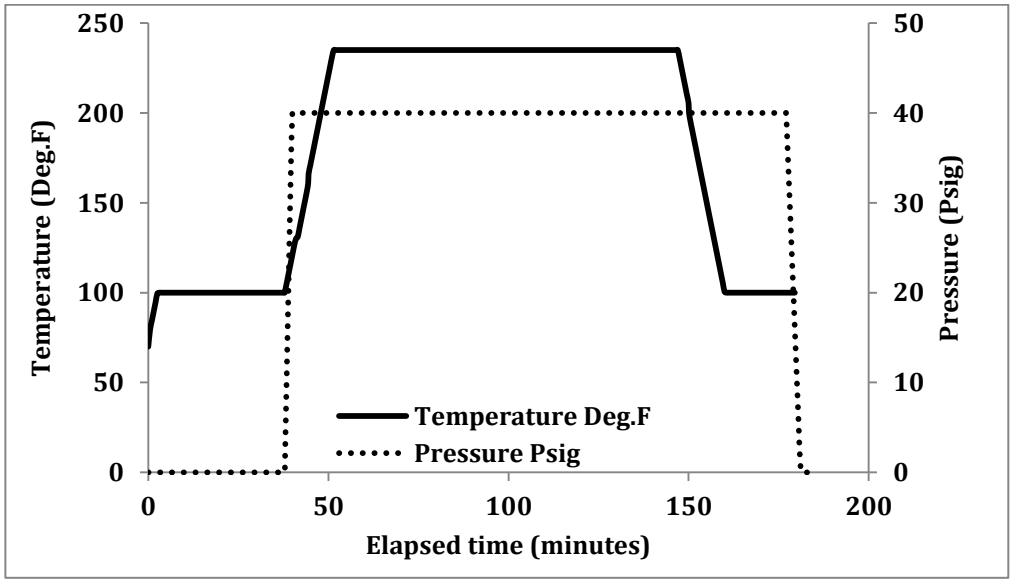


Figure 2.16. Cure cycle of adhesive film 163-2M

## 2.5. Summary

In this chapter, the manufacturing procedure for thick glass fiber epoxy composite laminates was discussed. In the literature on the manufacturing of thick composite laminate, the main focus was on developing optimized curing cycle from a theoretical approach. In this study, various debulking processes were investigated, which made a difference on the void distribution. It was shown that performing debulking process after every 3 layers for 5 minutes was the most effective and efficient. A series of quality tests were conducted to verify the specimen quality. However, it is very difficult to make the properties of every location over the whole specimen exactly the same due to the variability of composite material. It may have influences on the fatigue behavior.

# Chapter 3. Flexural Fatigue Test

## 3.1. Flexural fatigue test set-up

Flexural fatigue tests were performed on a flexural fatigue test machine developed and built at Concordia Center for Composites [59]. It has a maximum loading capacity of 50kN. The maximum displacement capacity is ±50mm. As shown in Figure 3.1, the fixture for mounting the specimen is able to hold the specimen in the horizontal direction in the form of cantilever beam. Test specimen is bolted down to the test rig at the fixed end. At the loaded end, the test specimen is clamped to the spherical ball joint. The ball joint is connected to the actuator. A pure cantilever bending fixture was also available[60]. It was unstable in the fatigue test so this fixture was not applied in this study.

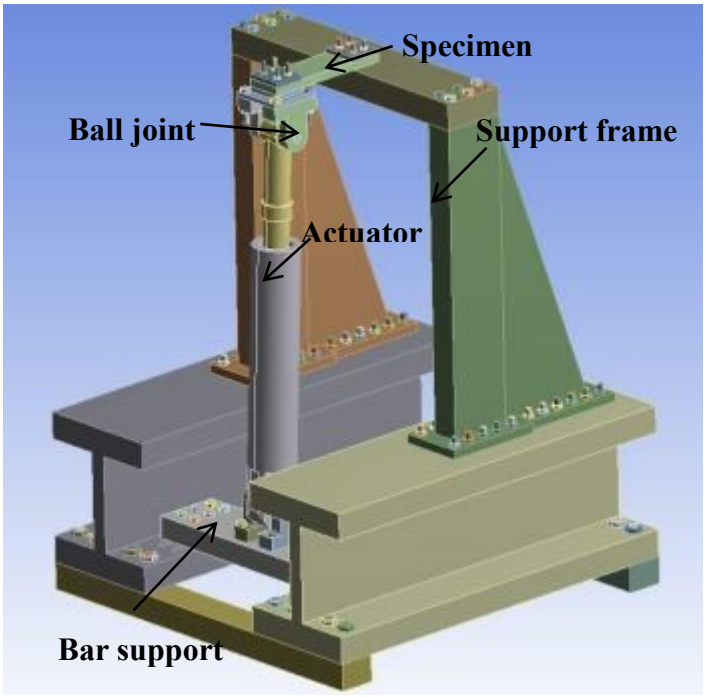


Figure 3.1. Flexural fatigue test machine with clamped-clamped loading fixture

All fatigue tests in the present work had a cyclic displacement ratio of 0.1. Test specimens were loaded upwards at a frequency of 3Hz. The top surface of the test specimen is always under compression while the bottom surface is under tension. The tests are controlled by the imposed displacement of the actuator. When the specimen is in the unloaded position as shown in Figure 3.2, a point B at a distance of 12.25" from the fixed end has a corresponding point A at the ball joint. When the actuator OA is extended, point A is supposed to move up vertically. However, due to the requirement that segment AB remains perpendicular to the length direction of the specimen, segment OA and segment AB rotate about the vertical axis. In Figure 3.3, segment OA becomes OA' and segment AB becomes A'B'. The actuator extension D = OA'-OA. The displacement of the specimen U depends on the rotation angles of the ball joint and the actuator. The angles change as the actuator extends. A calibration formula for the investigated test fixture is provided giving the relationship between the actuator extension and the resulting vertical displacement of the specimen [61].

For a point on the mid-plane at the location of the loaded end (point B), x=12.25 inches,

$$U = -0.0585D^2 + 0.9738D \quad \text{(unit in inches)}$$

$$\mathrm{Y} = -0.002303X^2 + 0.9738X \quad \text{(unit in mm)}$$

In Figure 3.3, when the actuator extends D = OA'-OA = 0.8", the resulting vertical displacement of point B on mid-plane of the specimen calculated by the given formula is 0.73". For the formula with unit in mm, Y is the specimen displacement while X is the actuator extension.

When the actuator is extended from the zero position in Figure 3.2 for $\mathrm{D} = 0.8"$

(X=20mm), the resulting U is 0.73" (Y=18.6mm) as shown in Figure 3.3. In the following discussions, the displacement refers to the displacement of the specimen U (Y).

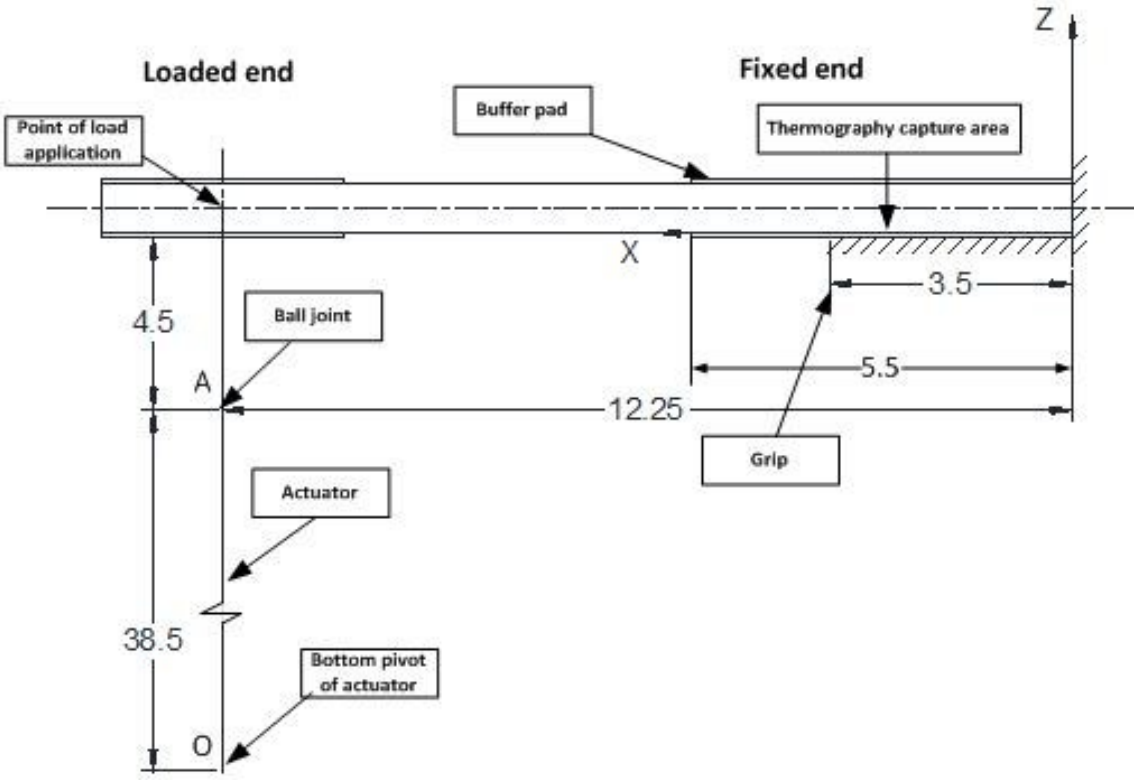


Figure 3.2. Schematic drawing of specimen at zero displacement (Dimensions in inches)

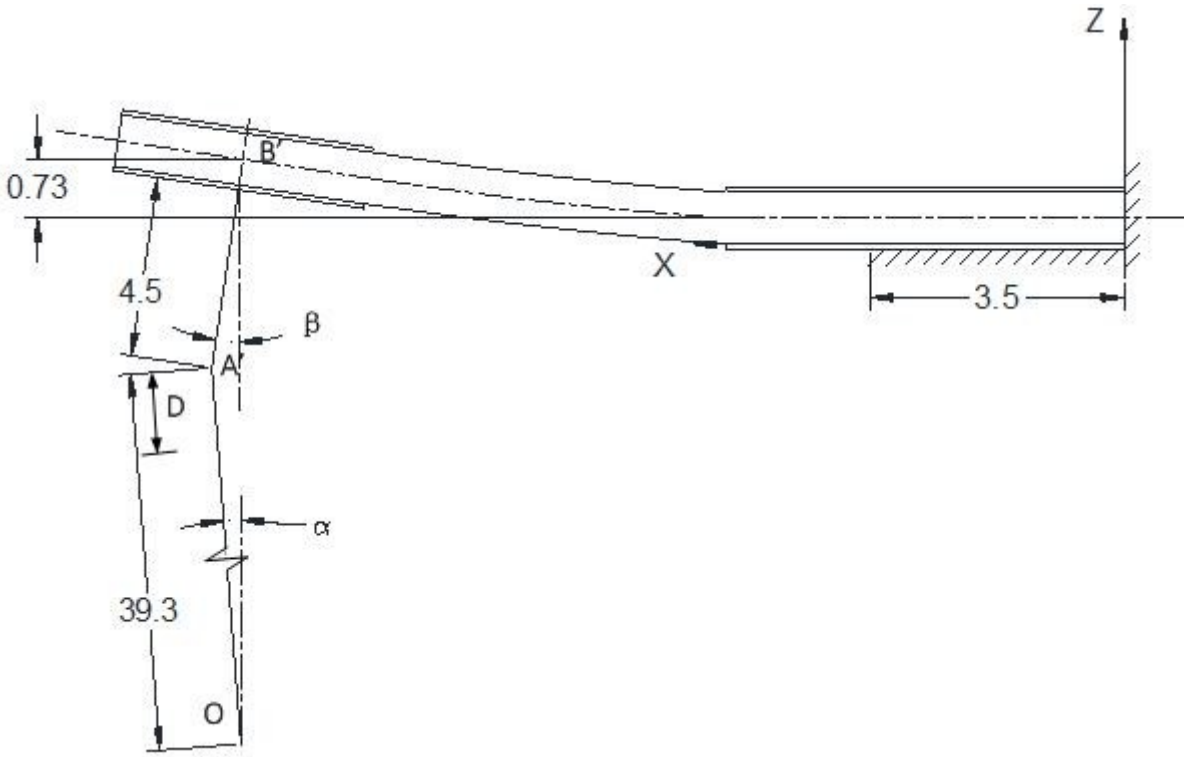


Figure 3.3. Schematic drawing of specimen at 0.73 inches displacement

At the beginning of the tests, the specimens were initially loaded upward at 1mm/sec to the minimum displacement. A single-sided cyclic bending test was performed. The necessary load to impose the constant displacement was continuously recorded with MTS control system. Due to the bending stiffness degradation of the sample, this load decreased during the fatigue life. A 20% reduction of the initial load was used as a failure criterion [64]. A $10^6$ cycles of fatigue was defined as a run out. The flexural fatigue tests were performed on two types of specimens: $[0]_{80}$ and $[0/90]_{20s}$. For each stacking sequence, four deflection levels (percentage of the static ultimate displacement) were conducted. The ultimate displacements were determined in the static tests [61]. $U_{ult}$ is the ultimate displacements in the static bending failure tests. $U_{min}$ and $U_{max}$ are the minimum displacement and maximum displacement in the

fatigue test respectively. R-ratio is the ratio of minimum displacement with maximum displacement. The deflection level is the percentage of the maximum displacement to the ultimate displacement. The $U_{ult}$ of unidirectional specimen and cross-ply specimen was 30.5mm and 39.1mm respectively [61]. The four deflection levels and corresponding displacements of each stacking sequence are shown in Table 3.1 and Table 3.2. As the ultimate displacement of the unidirectional specimen was smaller than that of the cross-ply specimen [61], the resulting deflection levels for unidirectional specimen were larger.

| **$U_{ult}$: 30.5mm** | **Displacement of specimen $[0]_{80}$ (mm)** | | | |
|---|---|---|---|---|
| **$U_{min}$** | 1.9 | 2.1 | 2.3 | 2.4 |
| **$U_{max}$** | 18.6 | 20.0 | 21.5 | 22.8 |
| **R-ratio** | 0.1 | 0.1 | 0.1 | 0.1 |
| **Level** | 61% | 65% | 70% | 75% |

Table 3.1. Four displacement deflection levels of $[0]_{80}$ specimens

| **$U_{ult}$: 39.1mm** | **Displacement of specimen $[0/90]_{20s}$ (mm)** | | | |
|---|---|---|---|---|
| **$U_{min}$** | 1.8 | 2.2 | 2.6 | 3.0 |
| **$U_{max}$** | 17.7 | 21.1 | 24.6 | 28.0 |
| **R-ratio** | 0.1 | 0.1 | 0.1 | 0.1 |
| **Level** | 45% | 54% | 63% | 72% |

Table 3.2. Four displacement deflection levels of $[0/90]_{20s}$ specimens

When a laminate is subjected to repeated loads, mechanical energy is dissipated due to

viscous damping. As the thermal conductivity of a composite material is low, especially for glass fiber reinforced composites, the generated heat cannot be dissipated easily, which results in a temperature increase. When a crack occurs, the strain energy is released to create two surfaces. And also, there may be a sound. The relative motion between two damaged surfaces can generate a certain amount of heat which results in temperature increase. In this study, an infrared thermal camera was utilized to track the temperature evolution of the test specimen during the fatigue tests. Recordings were focused on one of the side surfaces of the fixed end as shown in Figure 3.2.

## 3.2. Results and discussion

The flexural fatigue behavior of $[0]_{80}$ and $[0/90]_{20s}$ specimens are illustrated from following aspects: the maximum bending load degradation, temperature evolution at the crack area, crack propagation and distribution.

- Maximum bending load degradation

For the displacement controlled fatigue test, the loads at both maximum and minimum displacements were recorded from the data acquisition system. The load at maximum displacement decreased when damage occurred in the specimen. The load reduction ratios ($F/F_0$) are plotted with the number of cycles.

- Temperature evolution at the crack area

For the temperature evolutions in the specimens, software called Researcher IR was used to record and analyse the thermography data. From the recordings, the temperatures at specific point, line or area could be extracted with the corresponding frames, absolute time and relative time. As shown in Figure 3.4, wherever a delamination occurred, a significant line with higher

temperature was indicated from the thermography. When the delamination occurred inside the specimen, the location with highest temperature was selected. Some test specimens did not delaminate during the whole fatigue test, from the experience of delaminated specimen, the temperature measurements were taken on the area with higher possibility of delamination. With the known frequency (3Hz) of the fatigue test, the relative time was converted to the relevant number of cycles multiplying by 3. The temperature increase was plotted with the number of cycles. In the following discussion, the load degradation curves and the temperature evolution curves of each deflection level were plotted in the same figures to demonstrate the fatigue damage behavior.

- Crack propagation and distribution

The side surfaces (XZ plane as shown in Figure 3.5) of the test specimens were painted in white color for the observation of crack initiation and propagation. When a crack initiated or propagated on the side surface, the number of cycles was recorded. After the tests, the lengths of the cracks were measured by caliper. For reference, the coordinates and the locations of bolted holes are indicated in Figure 3.5. To inspect the inside damage of the tested specimens, specimens were sectioned along X or Y directions after the fatigue test as shown in Figure 3.6. A crack may initiate within the specimen or at the edge. The occurrence of a crack on the side surface may or may not correspond to a crack initiation.

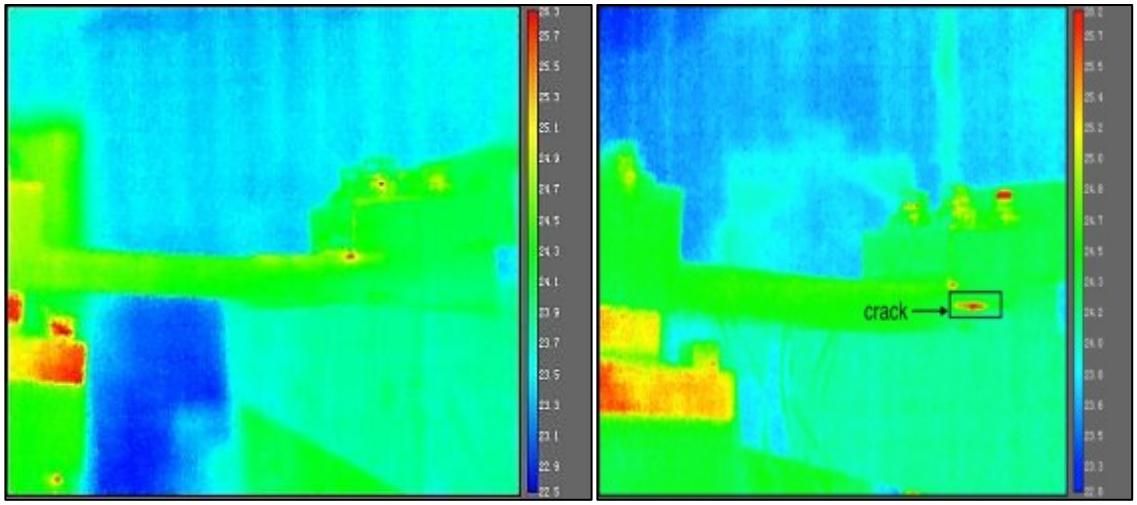


Figure 3.4. Typical thermal images of the test specimen at the periods without delamination (left) and with delamination (right)

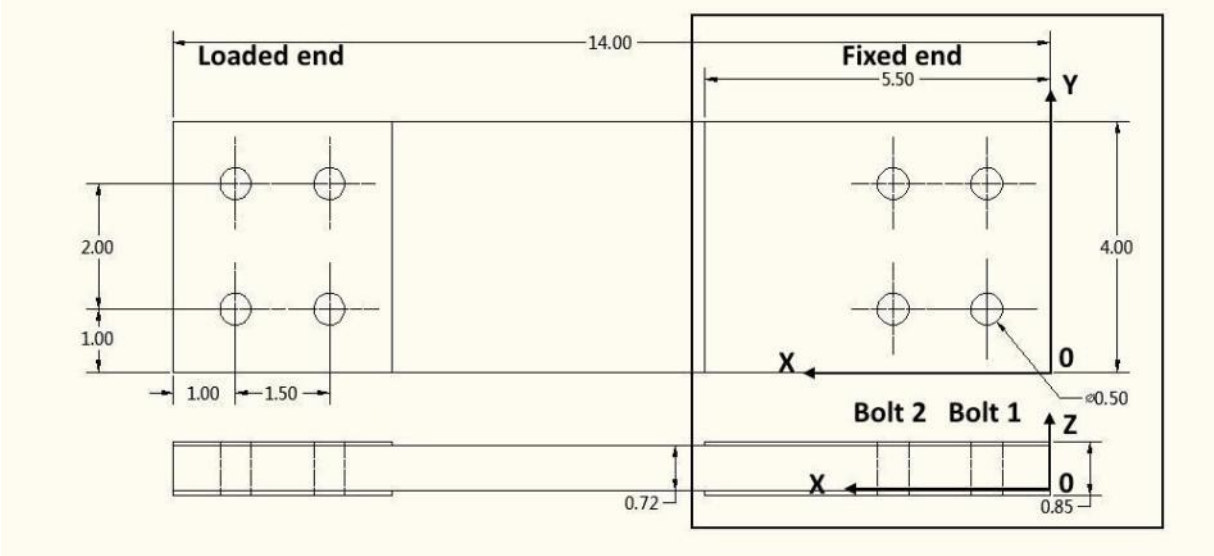


Figure 3.5. Investigated crack area

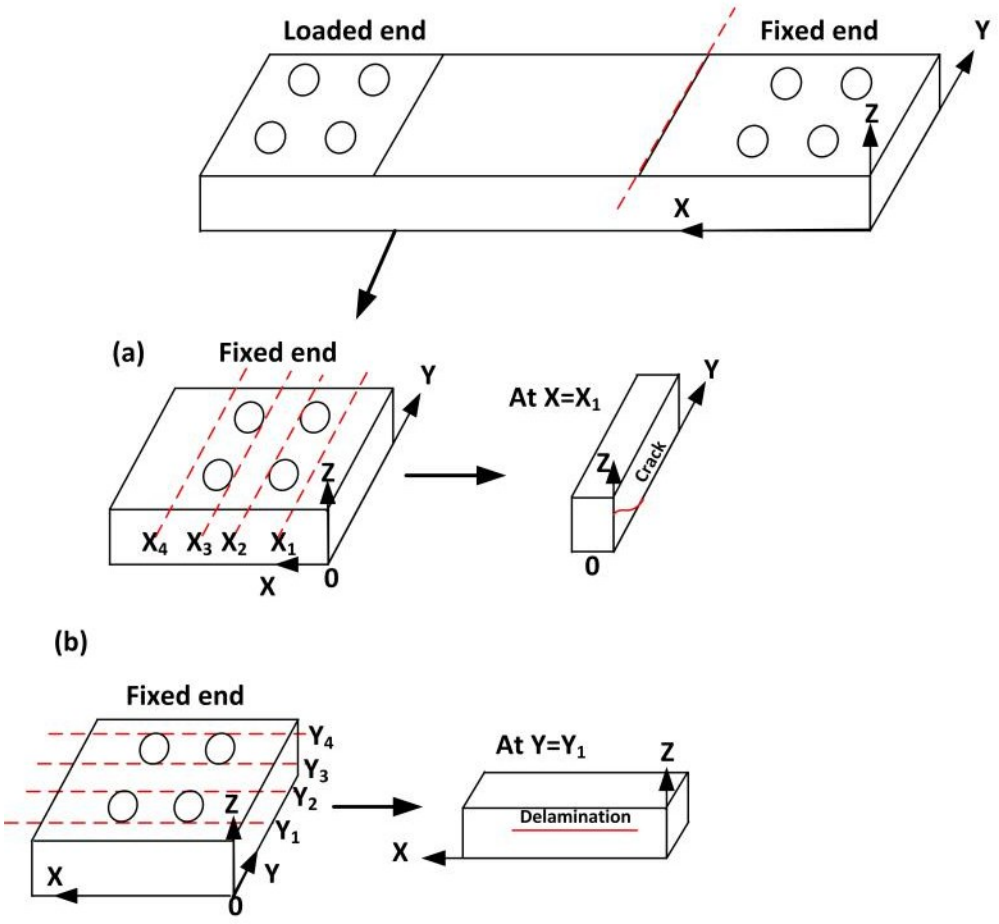


Figure 3.6. Sectioning of failed specimen at (a) different X positions and (b) different Y positions

### 3.2.1. **Flexural fatigue behavior of $[0]_{80}$ specimens**

In the fatigue life diagrams, the horizontal axis represents the number of cycles with a logarithm scale. The vertical axis on the left represents the bending load reduction ratio ($F/F_0$).

Figure 3.7 shows the load reduction ratio for unidirectional specimen loaded at four deflection levels: 61%, 65%, 70% and 75% of $U_{ult}$. The corresponding maximum displacements were 18.6mm, 20mm, 21.5mm and 22.8mm. At the beginning of each test, the buffer pad on the top surface of the specimen separated from the specimen at the supporting grip of the fixed end. When subjected to a bending deflection, the bond between the buffer pad

and the specimen was not strong enough to survive the fatigue cycling. The break of buffer pad led to a certain amount of load drop. The cycles when buffer pad broke depended on the bonding effect.

All curves in Figure 3.7 show two stages for the load reduction ratio. In the first stage, there is a gradual reduction of the load ratio. In the second stage, the rate of load drop increases. The number of cycles for the transition from step 1 to step 2 depends on the level of the maximum displacement.

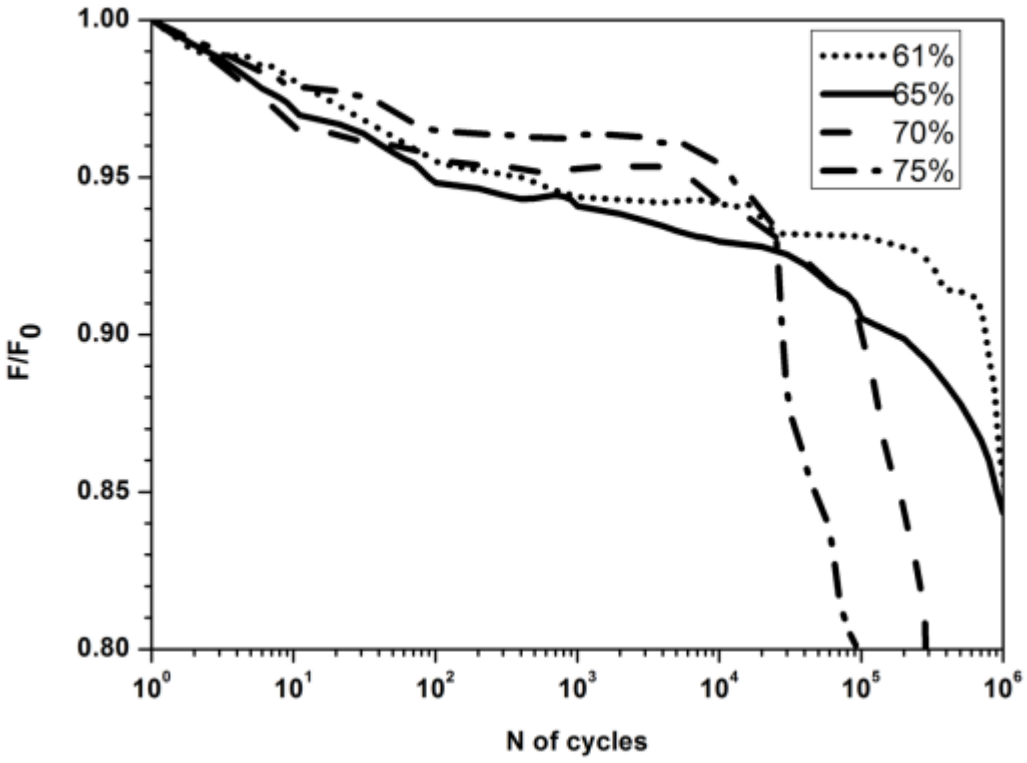


Figure 3.7. Load reduction ratio ($F/F_0$) versus the number of cycles for $[0]_{80}$ specimens

3.2.1.1 Deflection level 1: 61%

As shown in Figure 3.8, when the $[0]_{80}$ specimen was subjected to 61% of $U_{ult}$, the load decreased gradually during the whole fatigue lifetime. After 1 million fatigue cycles, which was defined as a run out, the total load drop was about 15%. No delaminations were observed on the side surfaces during the whole fatigue life. The surface temperature was not measured continuously through the 1 million cycles. The measurement indicated in Figure 3.8 started from 200 cycles to 10,000 cycles. It was observed that the temperature increased initially from 24℃ to 26℃. The temperature increase was mainly caused by the mechanical damping during the cycling of specimen. The energy cannot dissipate due to the low thermal conductivity, which results in temperature increase. After that, the temperature remained stable. It should be pointed out that the temperature was periodically measured after each 10,000 cycles increment and no significant increase was observed. From the beginning to 100 cycles, the load decreased about 5% due to the buffer pad debonding. After that, the load decreased gradually. Since no visible delamination and audible sound occurred during the test period, after the test, the specimen was sectioned at $X_1 = 2.0, X_2 = 2.8", X_3 = 4.05", X_4 = 4.55", X_5 = 5.05"$. A shear-out failure mode at the bolted joint was observed on the YZ cross-sections from $X_2 = 2.8"$ to $X_4 = 4.55"$. A typical photograph of this failure on the cross-section of $X_3 = 4.05"$ is shown in Figure 3.9. The width of the crack is the same as the diameter of the hole. The 3D distribution of the shear-out crack is shown in Figure 3.10. The height of the crack on each sectioned piece was located at $Z = 0.37"$ to $Z = 0.39"$, which was in the range of 51% to 54% of the total thickness (T). Failure started from the second bolt hole edge ($X = 2.75"$) toward the loaded end. The occurrence of this kind of failure did not cause any sudden load drops, sound and rapid temperature increase. Therefore, the initiation of the

shear-out crack was not detected.

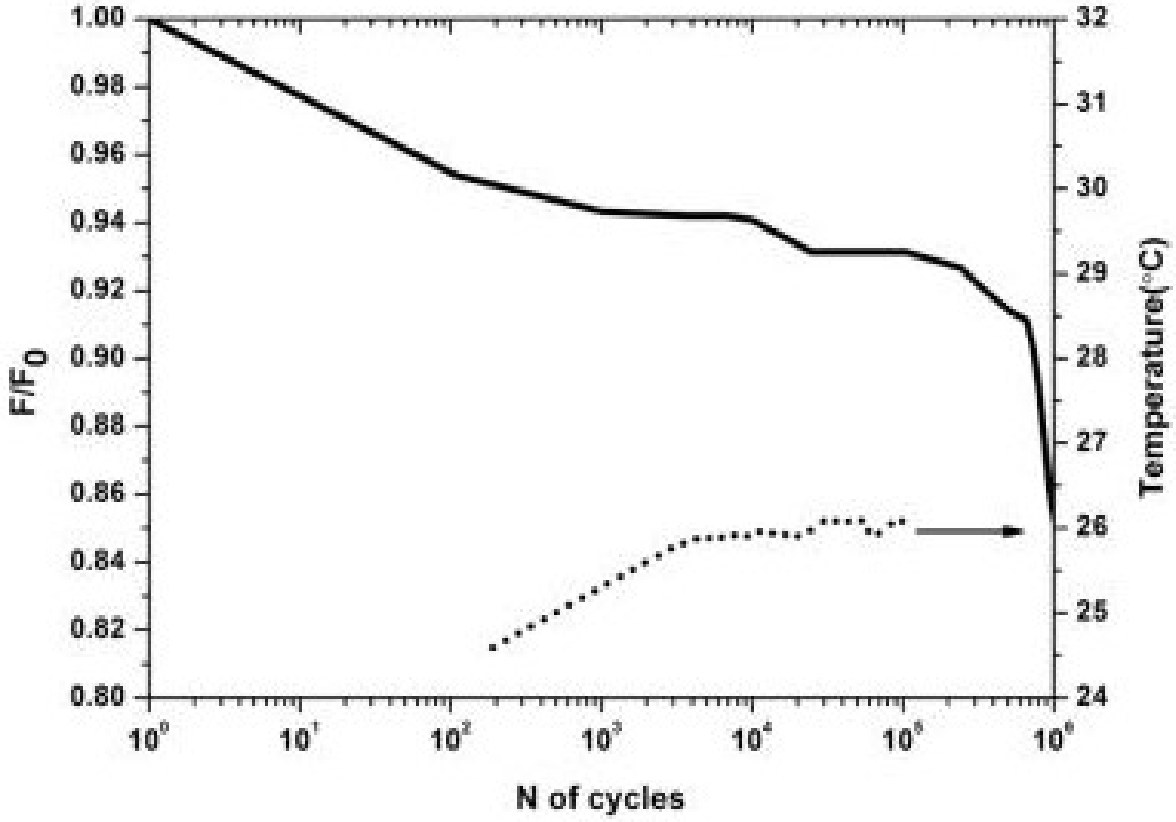


Figure 3.8. Load reduction ratio ($F/F_0$) and temperature increase at 61% deflection level

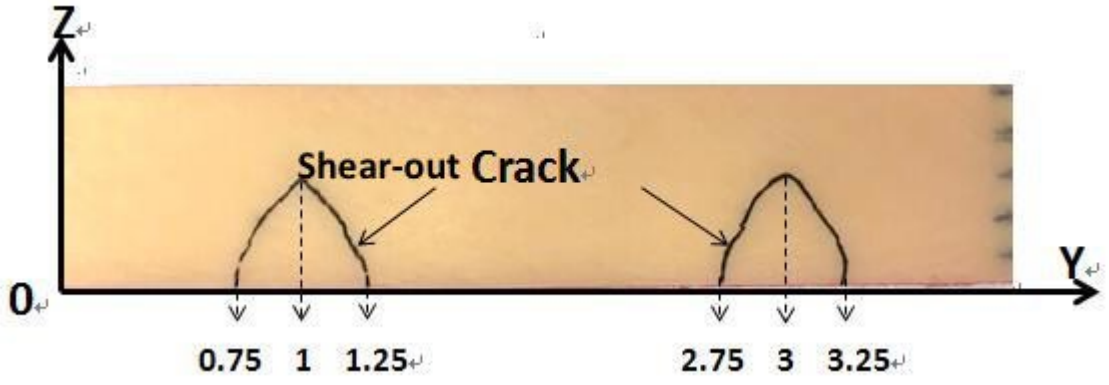


Figure 3.9. Typical crack caused by the shear-out failure of bolted joint at cross-section of $X_3 = 4.05"$

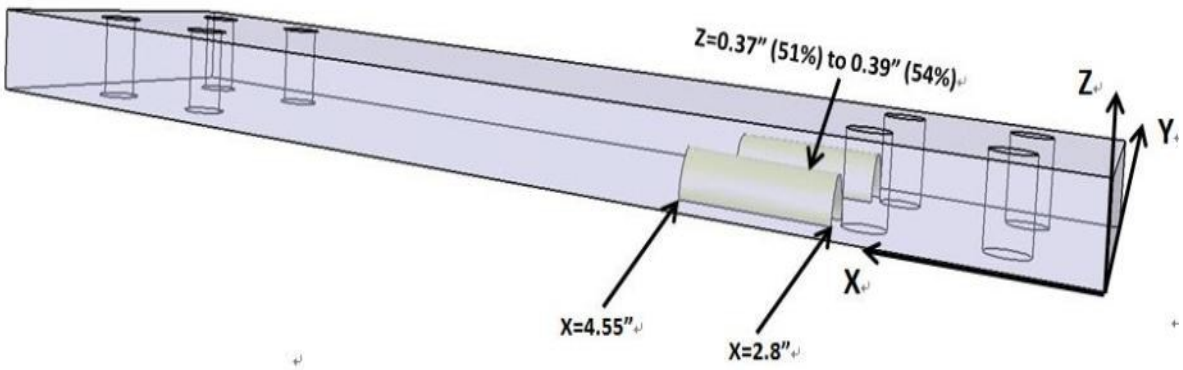


Figure 3.10. Schematic drawing of shear-out cracks of unidirectional specimen at 61% deflection level

3.2.1.2 Deflection level 2: 65%

Figure 3.11 shows the load drop and temperature variation for sample subjected to 65% deflection level. No visible delaminations were observed and total load drop was around 16%. The load degradation trend was similar to the deflection level of 61%. The buffer pad broke in the first 100 cycles with a load drop of 5%. The temperature started to rise up to 30℃ and became stable from 10,000 cycles. As the stress level became higher, the maximum temperature was 30℃ compared with the 26℃ at 61% level. The buffer pad debonding did not induce any temperature increase. The temperature increase was due to the mechanical damping as discussed previously. After the test, the specimen was sectioned at the following locations: $X_1 = 1.85", X_2 = 2.75", X_3 = 3.47", X_4 = 4.06", X_5 = 4.61", X_6 = 5.16", X_7 = 5.71"$. A similar shear-out failure mode as that at 61% level was also observed at the YZ cross-sections from $X_2 = 2.75"$ to $X_6 = 5.16"$. The 3D distribution of the shear crack is shown in Figure 3.12. The height of the crack on each sectioned piece was located at $Z = 0.33"$ to $Z = 0.39"$, Z/T was in the range of 45% to 49%.

From the shear crack distribution at 61% and 65% deflection levels, it was found this failure mainly appeared at the lower part of the specimen, which was under tension. The highest through-thickness locations (Z/T) of each shear-out crack on every sectioned piece are summarized in Figure 3.13. At 61% deflection level, shear-out cracks were observed on pieces $X_2$, $X_3$, $X_4$. At 65% deflection level, shear-out cracks were observed on pieces $X_2$, $X_3$, $X_4$, $X_5$, $X_6$. On each piece, there were two crack tips located at $Y = 1''$ and $Y = 3''$. They are distributed in the range of 45% to 54% (Z/T), mainly around the mid-thickness. The shear-out cracks are continuous along X direction within the observation range. The interlaminar shear has the potential to initiate the crack. When subjected to the low stress level but long fatigue cycles, shear-out failure in $0°$ layers is a common failure mode of the bolted joint.

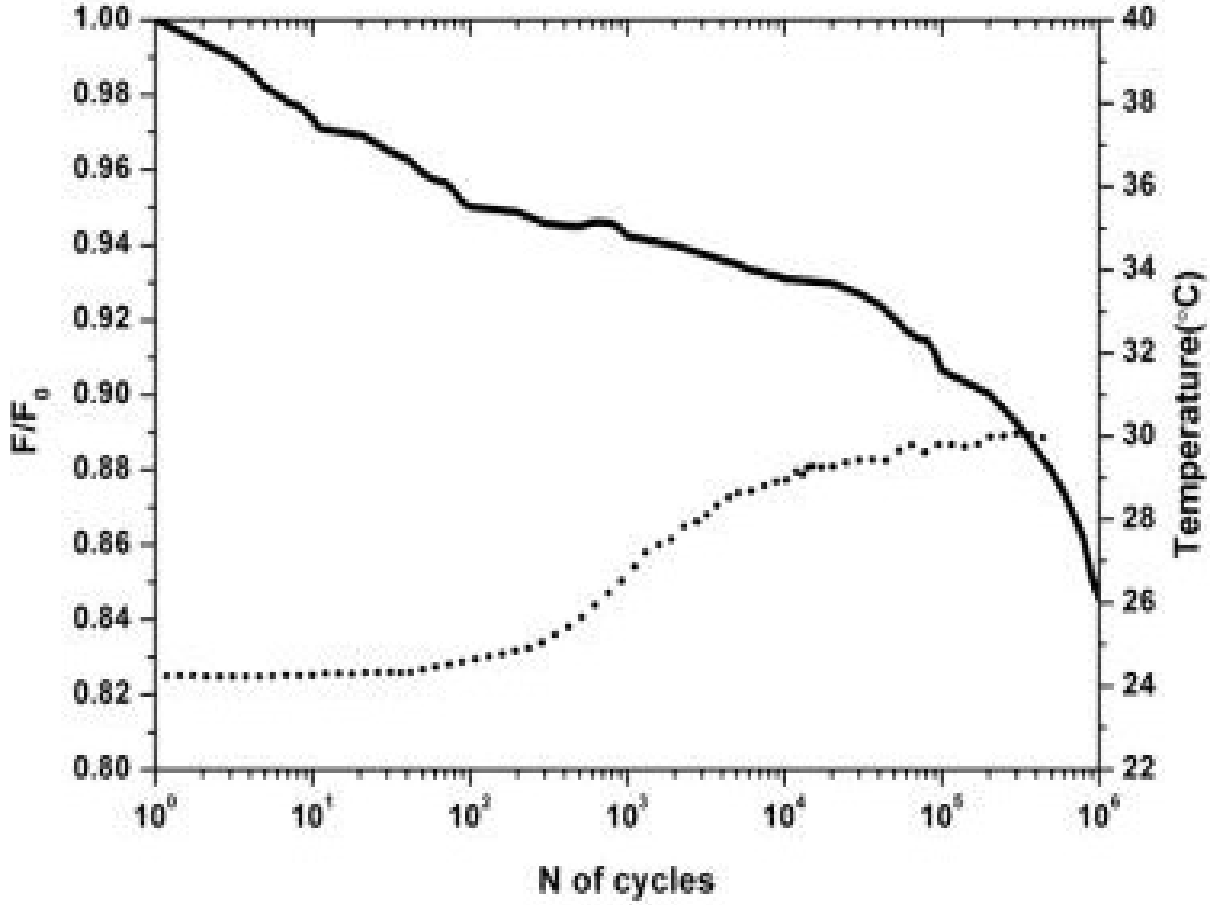


Figure 3.11. Load reduction ratio ($F/F_0$) and temperature increase at 65% deflection level

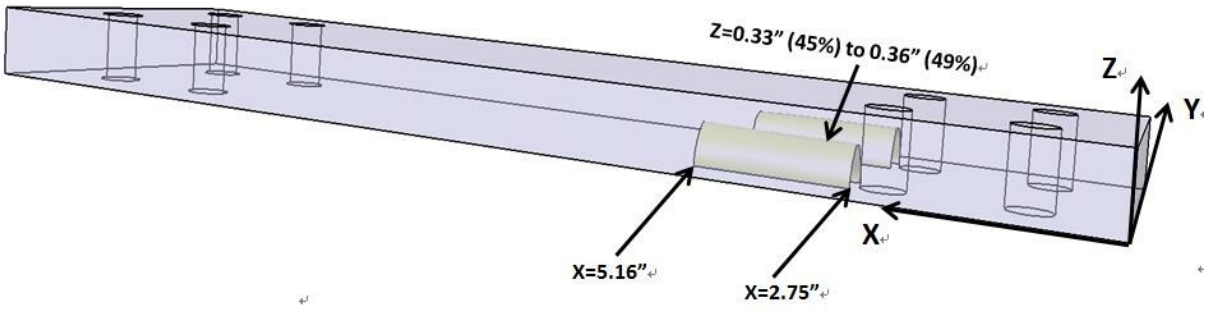


Figure 3.12. Schematic drawing of shear crack of unidirectional specimen at 65% deflection level

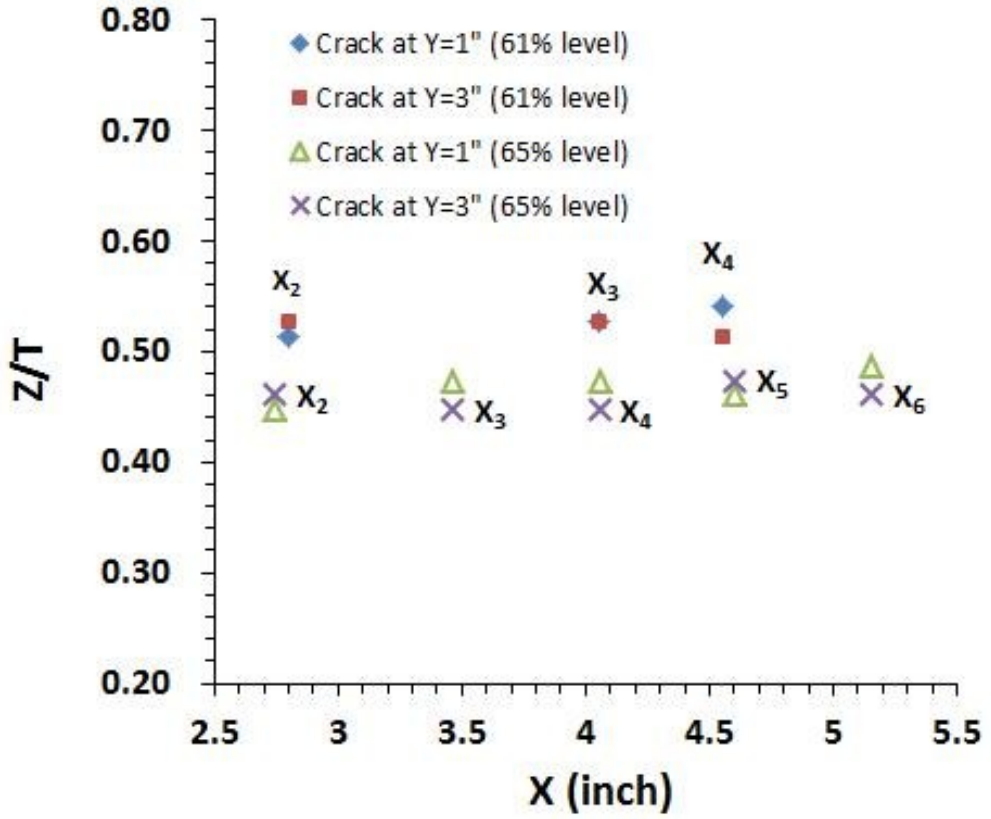


Figure 3.13. The through-thickness distribution of shear-out cracks on each sectioned piece of specimens at 61% and 65% deflection levels

3.2.1.3 Deflection level 3: 70%

Figure 3.14 shows the behavior of sample subject to 70% deflection level. The load dropped 5% during the first 60 cycles because of the break of the buffer pad. After that, the load experienced a stable period until 10,000 cycles with a temperature increase of 5℃ due to the mechanical damping. Then the load started to decrease until a visible delamination occurred on the side surface at 100,000 cycles. During this period, matrix cracks occurred and accumulated. In [62], it was mentioned in the development of fatigue damage, the matrix cracking occurs before the delamination and interfacial debonding. When a visible delamination appeared at

100,000 cycles, there was a sudden load drop as shown in Figure 3.15. This delamination occurred on side A as indicated with a solid line in Figure 3.16. The delamination created two surfaces at the damaged area. The friction between those two surfaces created a lot of heat, which resulted in the significant increase of temperature. Along with the delamination, part of the energy was released in the form of an audible sound. At 300,000 cycles, the load decreased to 20% of the initial value.

The region with the rectangle in Figure 3.5 is the area investigated in the following figures to discuss delaminations. They show the crack locations, propagation path and length on the two side surfaces (XZ plane) of specimens. The locations of the first bolt, second bolt and the grip (steel plate) are indicated in the figure. The two side surfaces of specimen are indicated with letter A and B in Figure 3.16. AL means the crack propagation toward the loaded end. The solid line shows the initiation length of the delamination, and the dotted line shows the propagation. The propagation of this surface crack toward the fixed end was not obvious. In Figure 3.16, the initial delamination on side A was at $Z = 0.43"$. It is 61% of the total thickness (T), which belongs to the compressive part. As the crack propagated, another delamination occurred on side B. It was at $Z=0.20"$ (Z/T=29%). The delamination on side B occurred during the period without supervision at night. Therefore the propagation was not recorded. The shear-out crack failure did not occur at this deflection level.

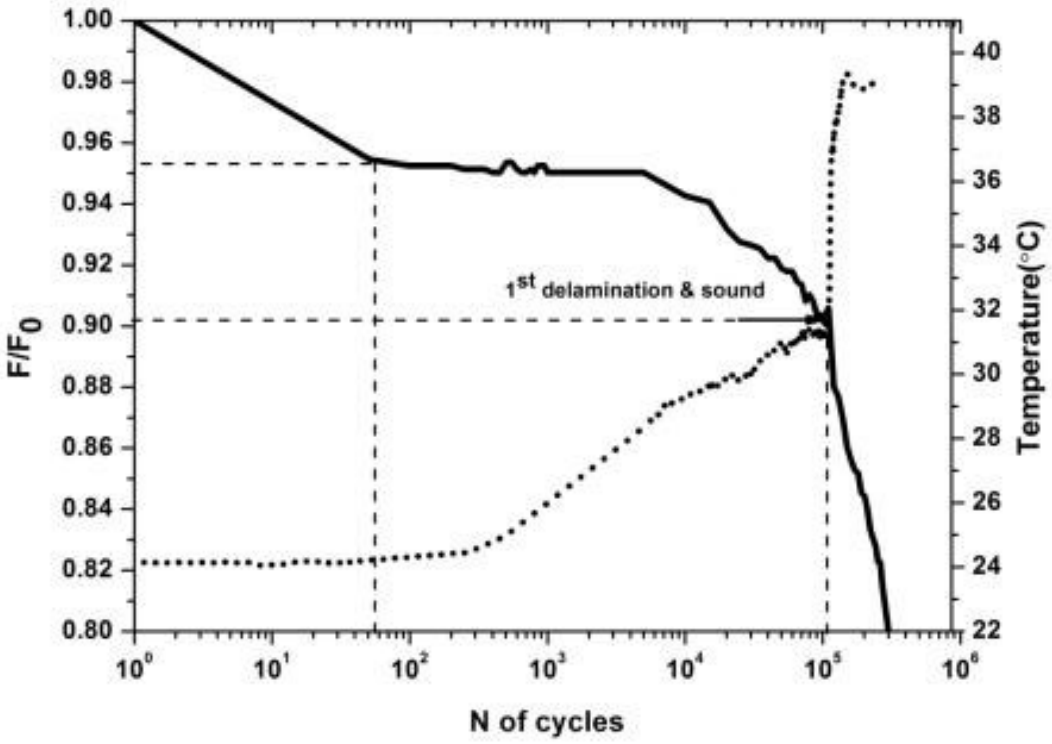


Figure 3.14. Load reduction ratio ($F/F_0$) and temperature increase at 70% deflection level

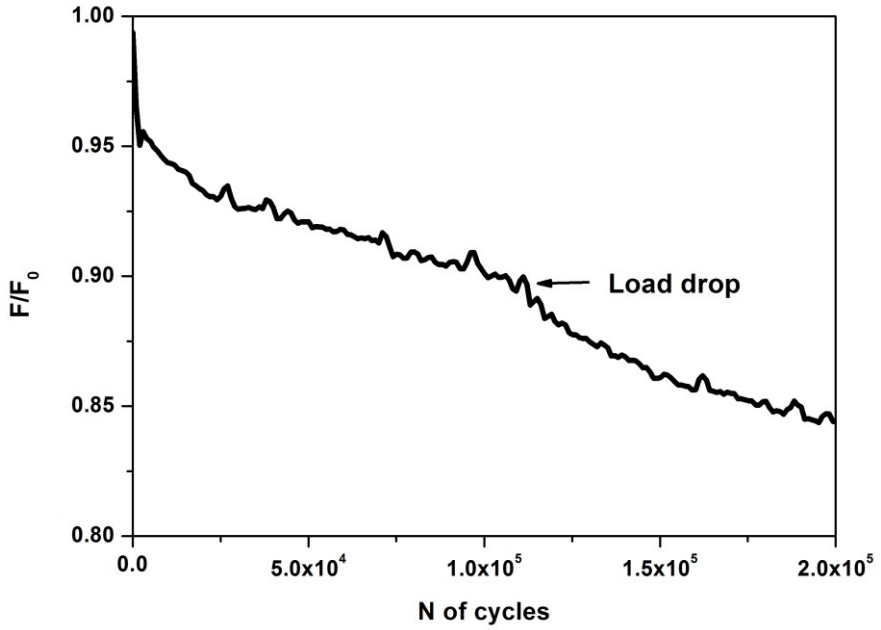


Figure 3.15. The load drop at the first delamination for unidirectional laminate at 70% deflection level

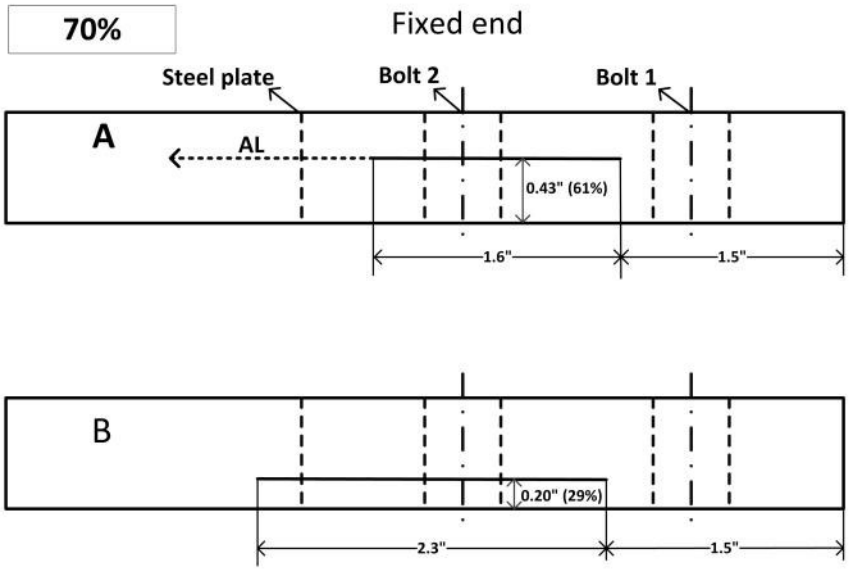


Figure 3.16. Delamination location on the side surface at 70% deflection level

3.2.1.4 Deflection level 4: 75%

Two replicates were carried out on this deflection level. The appearance of delamination was random. For one of the test specimens, the delamination occurred from inside instead of on the surface. The initiation of this inside delamination was detected by sound, load drop and temperature increase. From the previous experience, the area that might have delaminations was selected to measure the temperature variation. The temperature evolution is shown in Figure 3.17. A sudden temperature increase matched very well with the load drop resulted from the delamination. The load drop caused by the first delamination is shown in Figure 3.18. This first delamination occurred at around 26,000 cycles. The total fatigue life of this specimen was 110,000 cycles. For the other test specimen as a replicate, the first delamination occurred on the surface at 25,000 cycles with the fatigue life of around 110,000 cycles. The locations and propagations of the surface cracks on this test specimen are shown in Figure 3.19 and Figure 3.20. The load reduction curve had a very similar trend with the load curve in Figure 3.17.

In Figure 3.20, the horizontal axis of the graph presents the fatigue life ratio $N/N_f$, where N is the number of cycles and $N_f$ is the fatigue life cycles. The vertical axis presents the delamination length. The initiated length of the first delamination on side A was $2.5"$ and it happened at near 23% of the fatigue life. In Figure 3.19, the delamination is located at $Z = 0.39"(53\%)$. The propagations on two surfaces toward the loaded end are indicated as AL and BL, while the propagations on two surfaces toward the fixed end are indicated as AF and BF. The second delamination occurred on side B along with an audible sound at 58% of the fatigue life. It is located at $Z = 0.28"(38\%)$. The cracks on two side surfaces propagated to both directions along the length. They propagated more to the fixed end than the loaded end. When the delamination reached to the edge of the specimen, it continued expanding along YZ surface.

The delaminations on two side surfaces did not initiate symmetrically at the same time, they occurred randomly. This is because damage prefers to occur at a weaker region. If there are more defects existing at one side compared to the other side, the delamination will initiate there. During the manufacturing process, it is difficult to make samples with the perfectly same quality everywhere. At this deflection level, the shear-out crack failure did not occur.

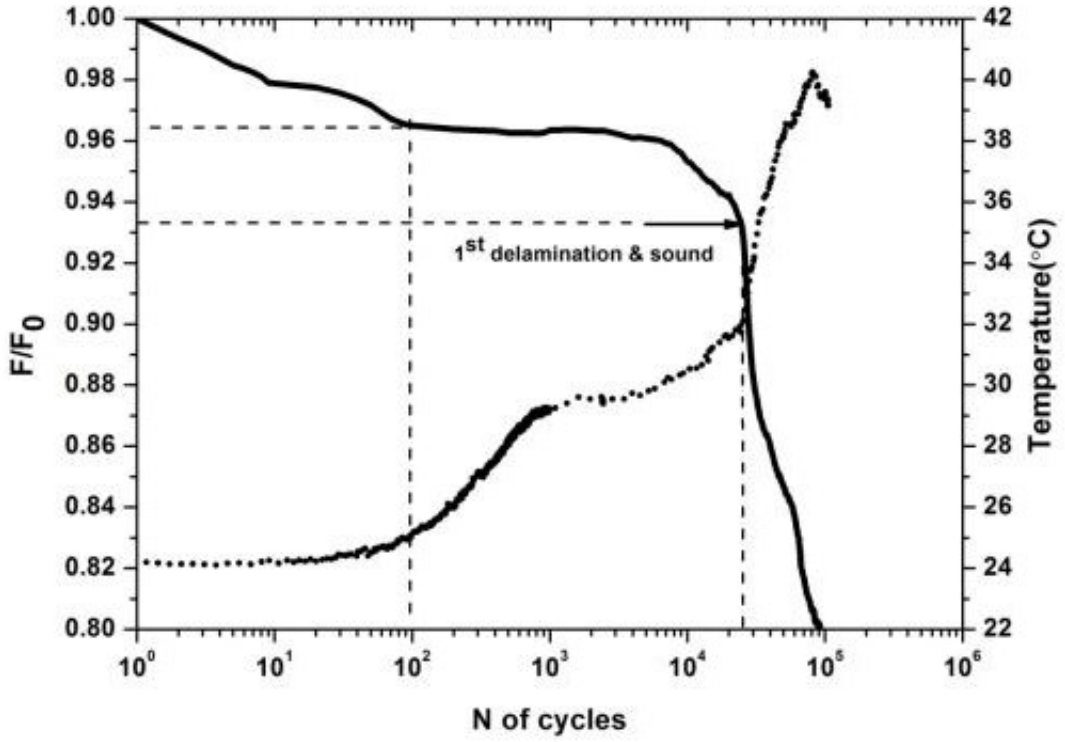


Figure 3.17. Load reduction ratio ($F/F_0$) and temperature increase at 75% deflection level

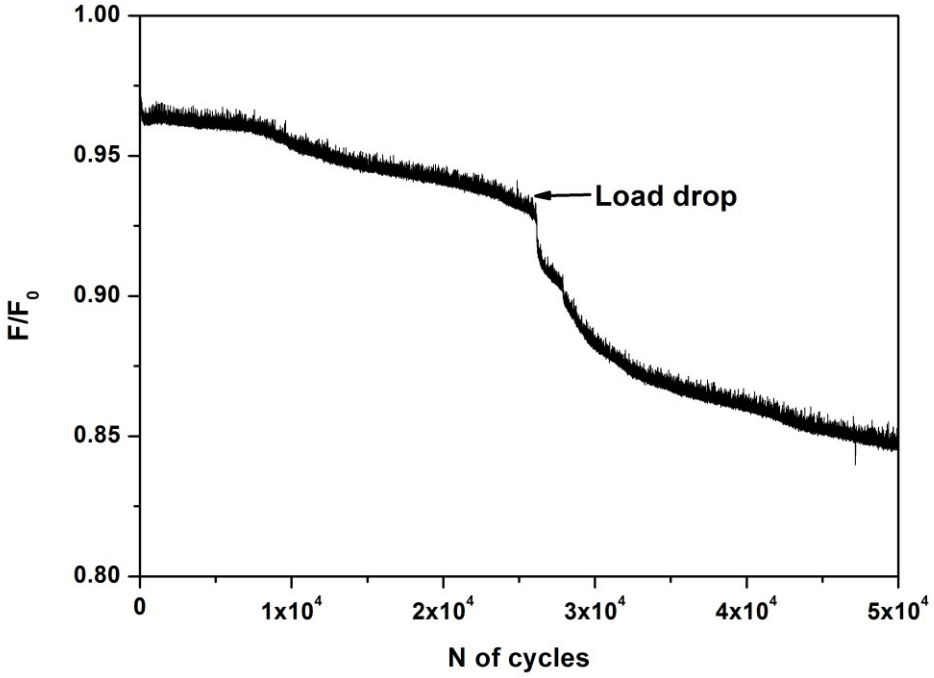


Figure 3.18. The load drop at the first delamination for unidirectional laminate at 75% deflection level

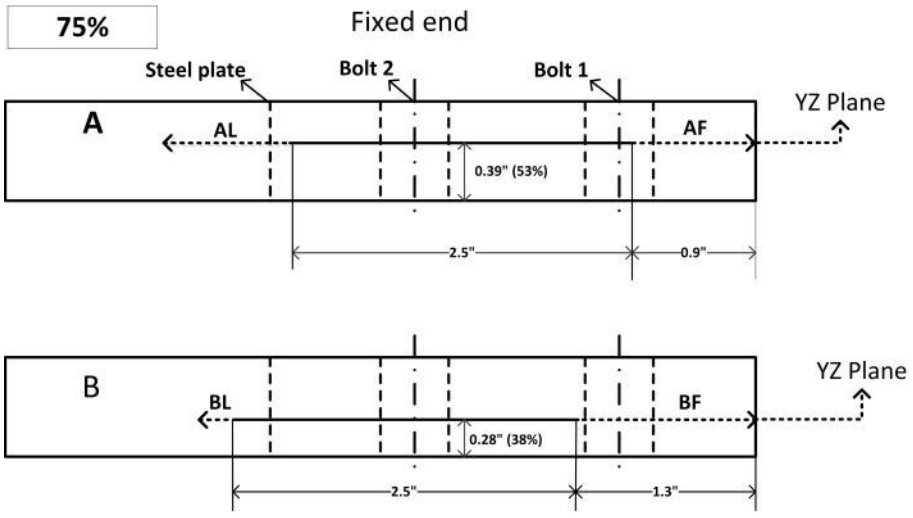


Figure 3.19. Crack location on the side surface of specimen tested at 75% deflection level

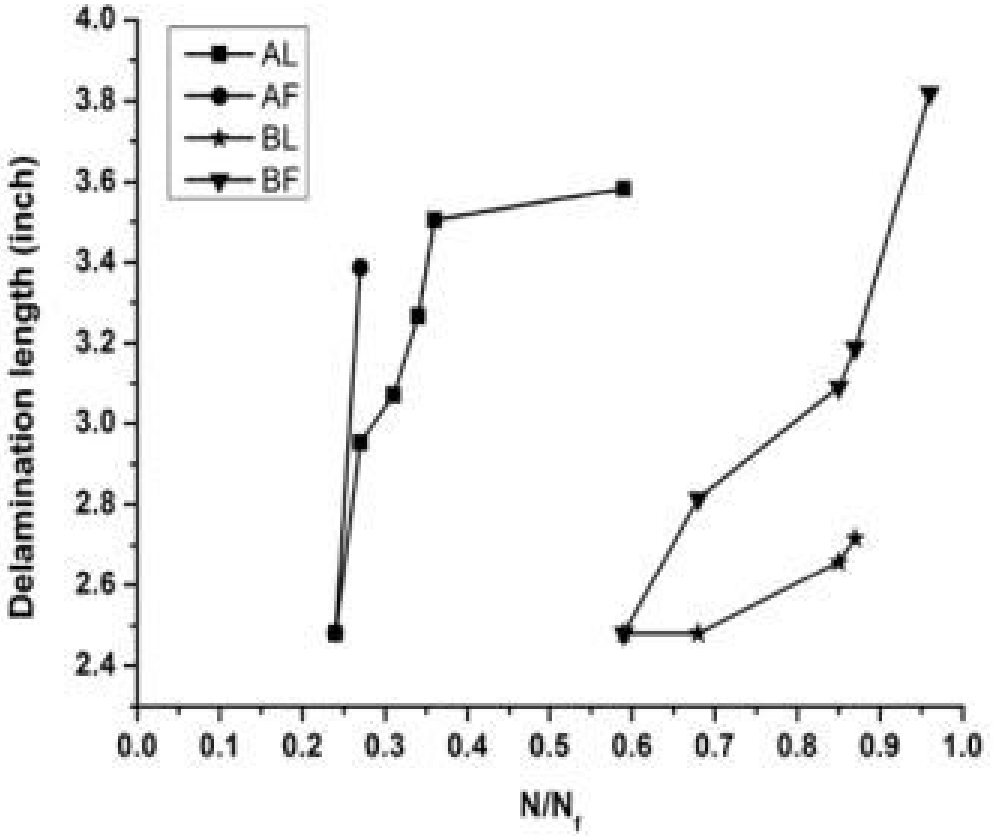


Figure 3.20. Crack propagations at 75% deflection level

3.2.1.5 Discussion

In unidirectional specimens, there are two types of failure: shear-out crack which occurs at different thickness levels, and delamination which occurs at the same thickness level. The shear-out crack failure always happens at lower deflection levels without the appearance of delamination. When the beam is subjected to a high stress level, delamination initiates. Then stress is relieved, the shear-out failure will not occur. Additionally, the shear-out failure needs long-term fatigue cycles to propagate, the delamination at high stress level initiates early, so there is not enough time for shear-out crack forming or propagating. From the observation of

shear cracks on each sectioned YZ planes, it was found out that the highest point of the crack was located at 45% to 54% of the total thickness level, which was around the mid-thickness level. The interlaminar shear stress has the potential initiating this crack. The surrounding bolted hole area is under through-thickness compression, which makes crack propagate transversely. Away from the hole area, the lower part of the specimen was subjected to in-plane tension. Edge effect also exists around the hole, which may result in the failure shape of the crack shown in Figure 3.9. When the beam was bended upward, the lower part of the specimen was always under tension, the crack propagated toward the loaded end.

The locations of the initial delaminations at both deflection levels of 70% and 75% are closer to the upper part of the laminate along the thickness direction. When the specimen was bended upward, the boundary conditions at top and bottom are different around the grip due to the high stress concentration. For this project, in the static numerical analysis under the same clamped-clamped loading condition, it is found that the maximum interlaminar shear stress does not remain at the same thickness level [63]. For example, at X= 2.75" (edge of the second bolted hole), the maximum interlaminar stress is at mid-thickness. At X=3.1", the maximum interlaminar stress is at position of Z/T=55%, which is the upper part of the specimen. This shift may cause the shear-out crack and delamination induced by interlaminar shear stress initiating at the observed thickness levels.

### 3.2.2. **Flexural fatigue behavior of $[0/90]_{20s}$ specimens**

The cross-ply specimens were tested under four deflection levels as presented in Figure 3.21: 45%, 54%, 63% and 72% of the ultimate displacement as determined previously in the static failure test. The delamination was observed on the test specimens at all the performed

deflection levels. Before 100 cycles, the first load drop was caused by the buffer pad debonding. For the two lower deflection levels namely, 45% and 54%, the first drop occurred earlier than the other two higher levels. This might be due to the poor bonding of the buffer pads, which was discussed in the manufacturing part. After that, the loads at those two levels decreased gradually until the delamination occurred. The specimens were run up to $10^6$ cycles. For the specimens at two higher deflection levels namely, 63% and 72%, after the initial load drops, the bending loads decreased more quickly because of the early delaminations.

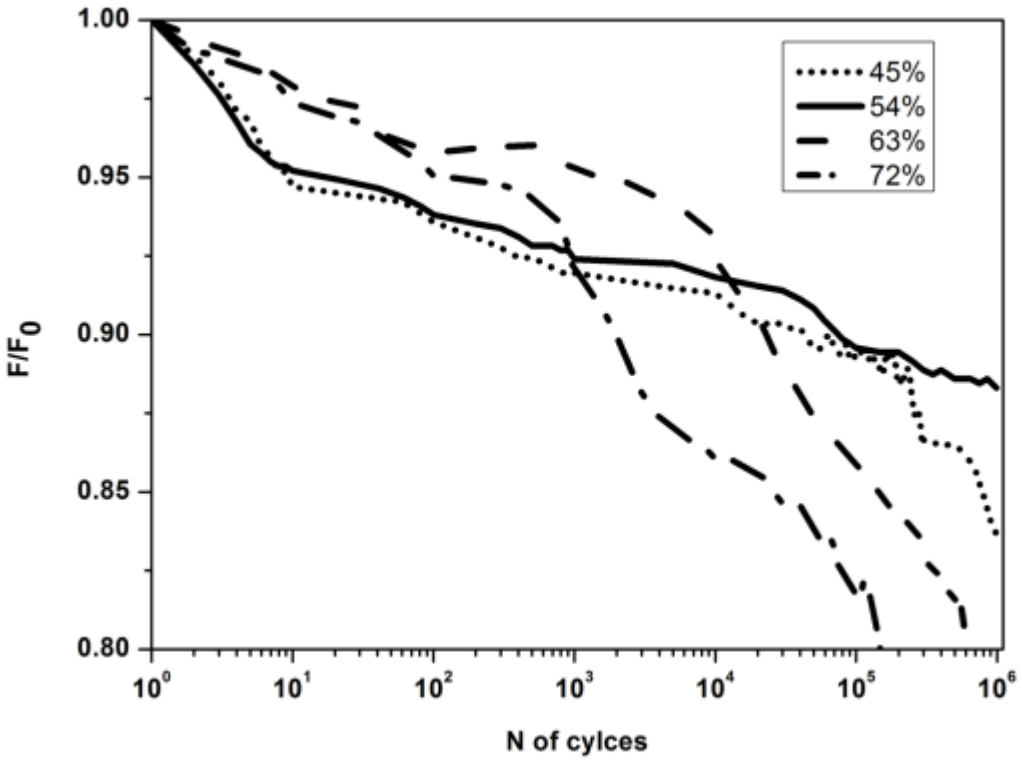


Figure 3.21. Load reduction ratio ($F/F_0$) versus the number of cycles for $[0/90]_{20s}$ specimens

3.2.2.1 Deflection level 1: 45%

As presented in Figure 3.22, the buffer pad broke at 10 cycles with a 5% load drop. After that it experienced a gradual decrease until the crack occurred. The first crack occurred at about 230,000 cycles on side B along with a temperature increase and the sound. The second crack on side A occurred between 250,000 and 280,000 cycles. As shown in Figure 3.25, the initial lengths of those two cracks were about 1.7"and 1.6" respectively. The cracks on both surfaces propagated to two directions. The growth to the fixed end was more than the loaded end. The existence of bolted holes made the area around them become weaker, which provided an easier way for the propagation of crack. The mode of cracks on cross-ply specimens is different from that of the unidirectional specimens. The crack on the surface appears in a zig-zag shape as indicated by the solid lines in Figure 3.23. The enlarged schematic drawing of this failure is shown in Figure 3.24. The positions of the zig-zag points on side A and side B are the same, namely 3.2" away from the fixed end. Along Z direction, the initiated cracks are located around the mid-thickness. Those two cracks on side A and side B occurred within 50,000 cycles and grew quickly, which resulted in a rapid load drop. The load drop at $10^6$ cycles was 15% of the initial state. The temperature recording at this level was not performed continuously on the same side surface, because there was only one thermal camera available in the lab. The recording always focused on side A. However, the first crack of this test specimen occurred on side B. The camera was moved to side B for the following recording. The temperature profile in Figure 3.22 shows a sudden increase from 26℃ to 29℃ at the point of damage initiation.

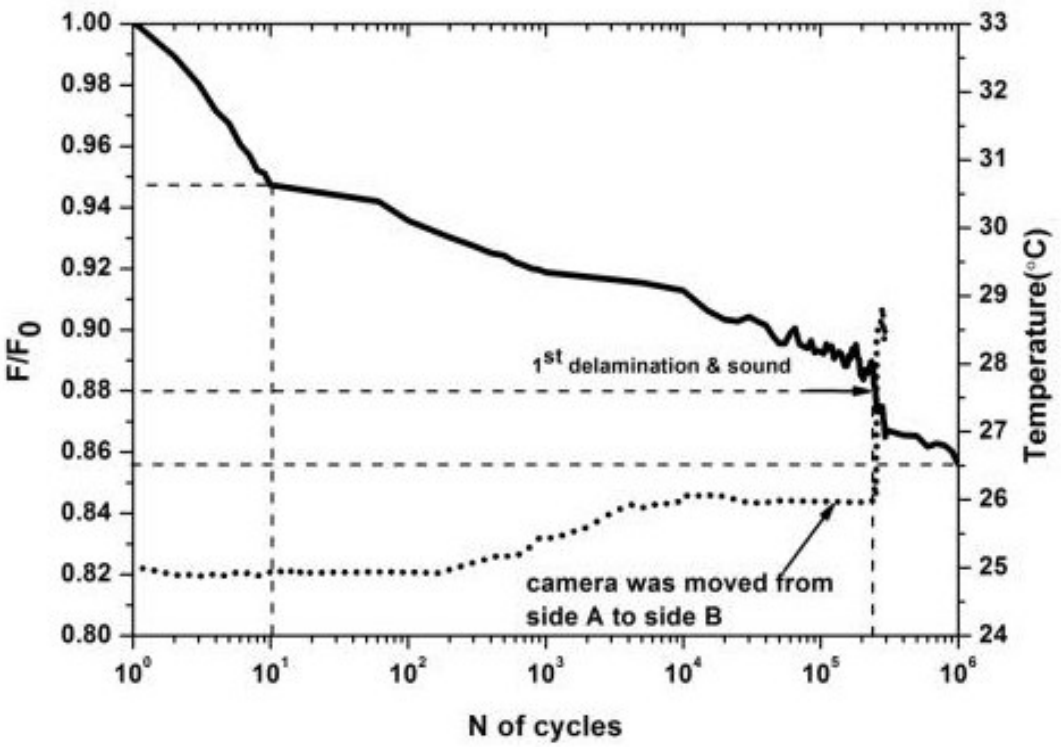


Figure 3.22. Load reduction ratio ($F/F_0$) and temperature increase at 45% deflection level

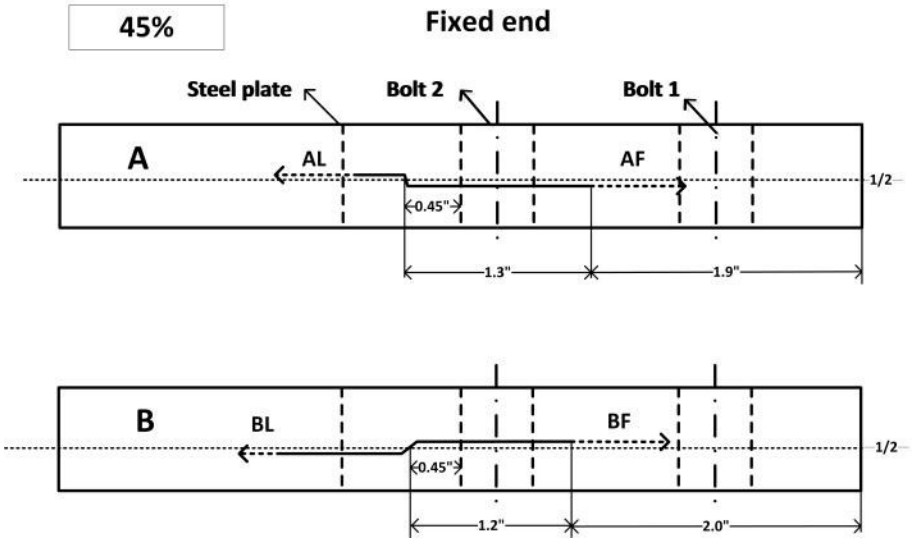


Figure 3.23. Crack location on the side surface of tested specimen at 45% deflection level

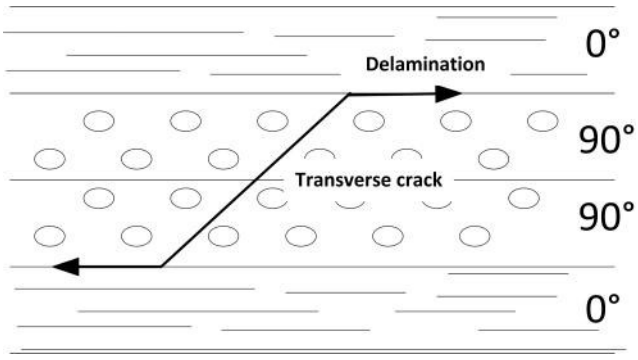


Figure 3.24. Schematic drawing of the zig-zag shaped failure at the mid-plane of the cross-ply specimen

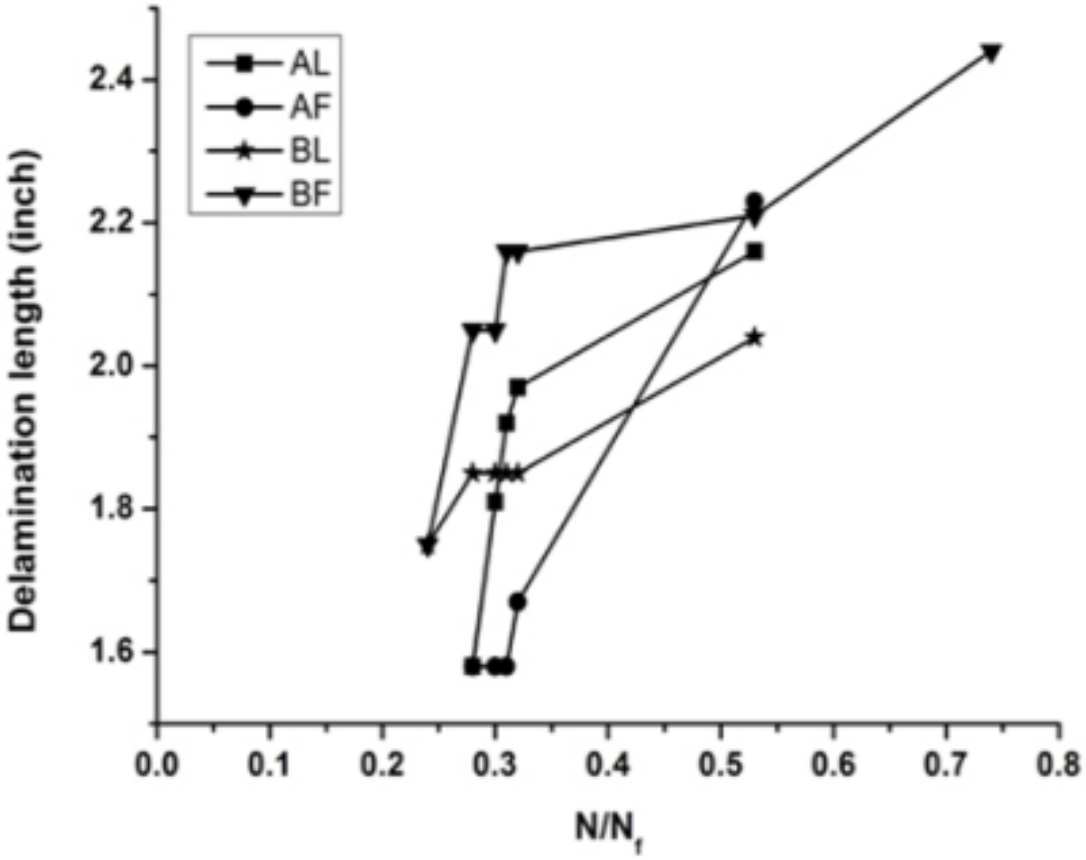


Figure 3.25. Surface crack propagations at 45% deflection level

3.2.2.2 Deflection level 2: 54%

At the deflection level of 54%, the buffer pad was debonded at 10 cycles and induced a 5% load drop. The first delamination was observed on the side A at around 90,000 cycles along with a temperature increase from 27.5℃ to 31.5℃ as shown in Figure 3.26. As shown in Figure 3.27 and Figure 3.28, the initiated length of this delamination was 0.47". The initial zig-zag point was 3" away from the fixed end. The occurrence of this crack did not come with an audible sound because of the small crack size. However, the initiation of the crack was clearly captured by the thermography. After the crack was initiated on the surface, the temperature remained around 31.5℃. The delamination size was smaller and the propagation of this delamination was less than that of 45% level. This was probably because the crack surrounding region was not as weak as that at 45% level. The surrounded 90° fibers gave better resistance to the crack propagation. When the specimen was run up to $10^6$ cycles, the total load reduction was 12%.

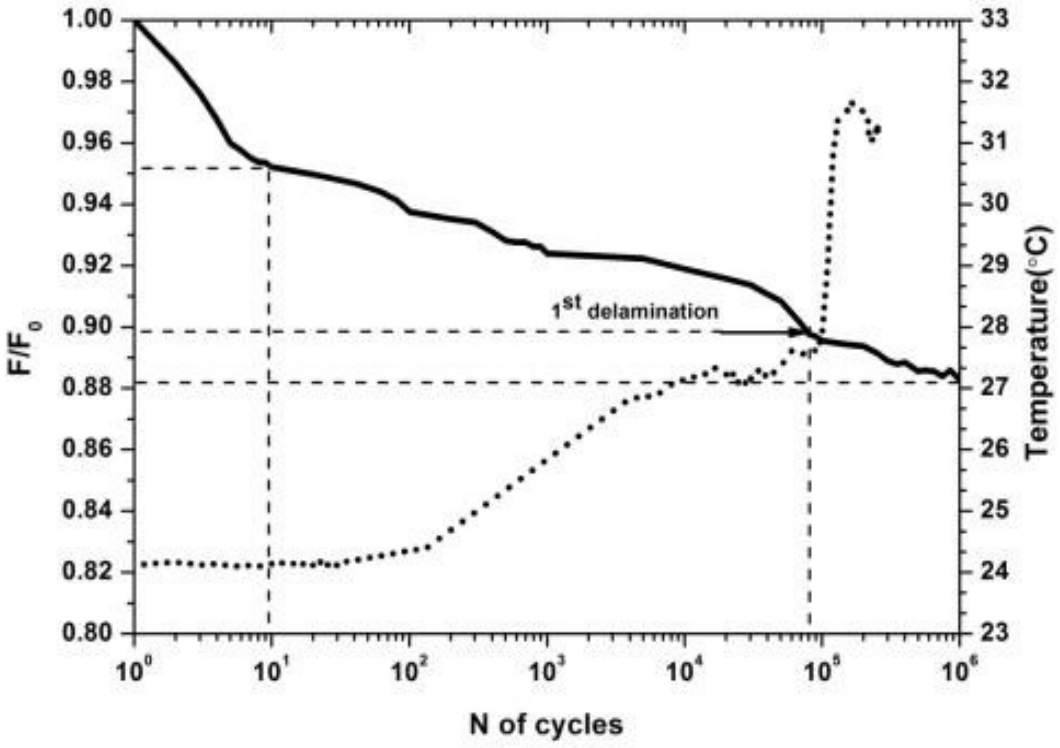


Figure 3.26. Load reduction ratio ($F/F_0$) and temperature increase at 54% deflection level

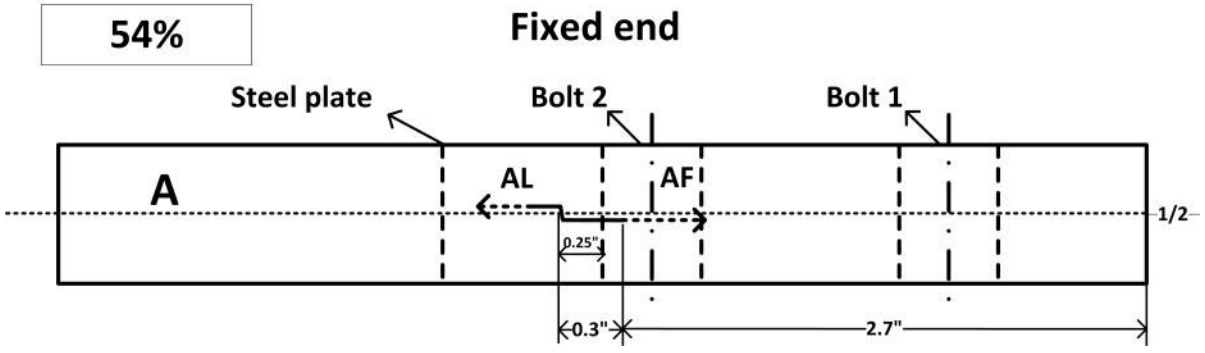


Figure 3.27. Crack location on the side surface of tested specimen at 54% deflection level

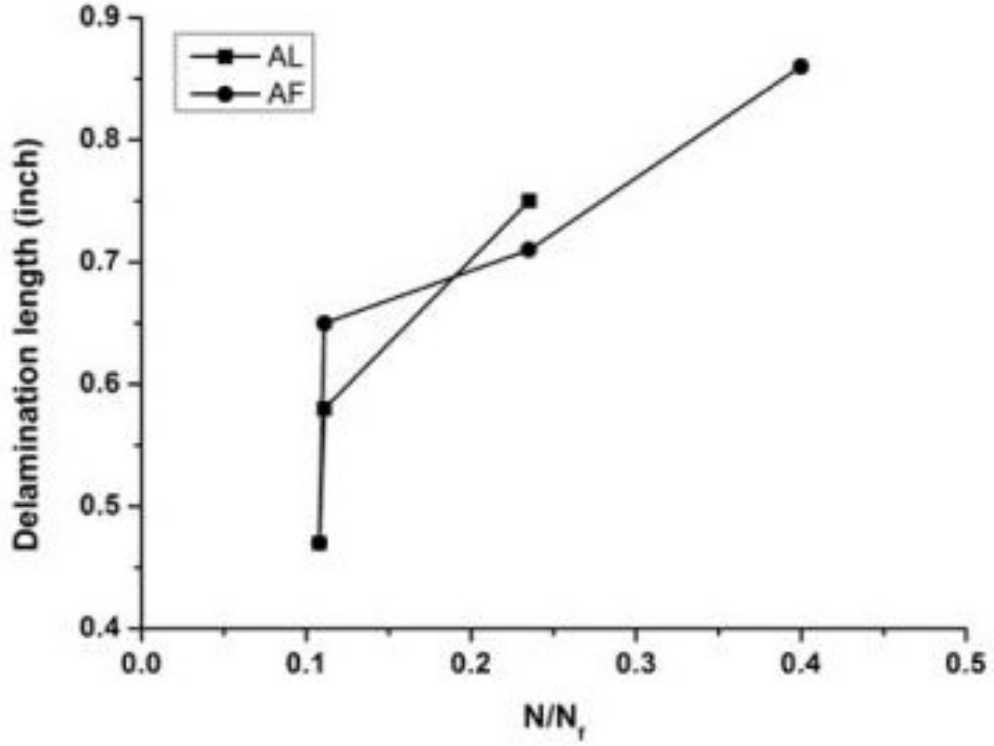


Figure 3.28. Surface crack propagations at 54% deflection level

3.2.2.3 Deflection level 3: 63%

At the deflection level of 63%, the buffer pad was debonded at 70 cycles with about 4% load drop. The temperature started to rise from 24℃ at 200 cycles to 28℃ at 2000 cycles due to mechanical damping. During this period, the load remained stable. Then the load started to decrease gradually for another 4% until the first crack occurred at about 14,000 cycles on side A as indicated in Figure 3.29. The initiation came along with an audible sound. Whenever the crack initiated, a rapid 10℃ increase of temperature happened along with a quick decrease in the structural stiffness. The load drop caused by this crack is shown in Figure 3.30. The total fatigue life at this level was 600,000 cycles. In Figure 3.31, the positions of the zig-zag points

on side A and side B are 3" and 2.5" away from the fixed end respectively. Figure 3.32 shows that the cracks propagated with a slow rate during the fatigue life. The crack on side A also extended on the YZ surface.

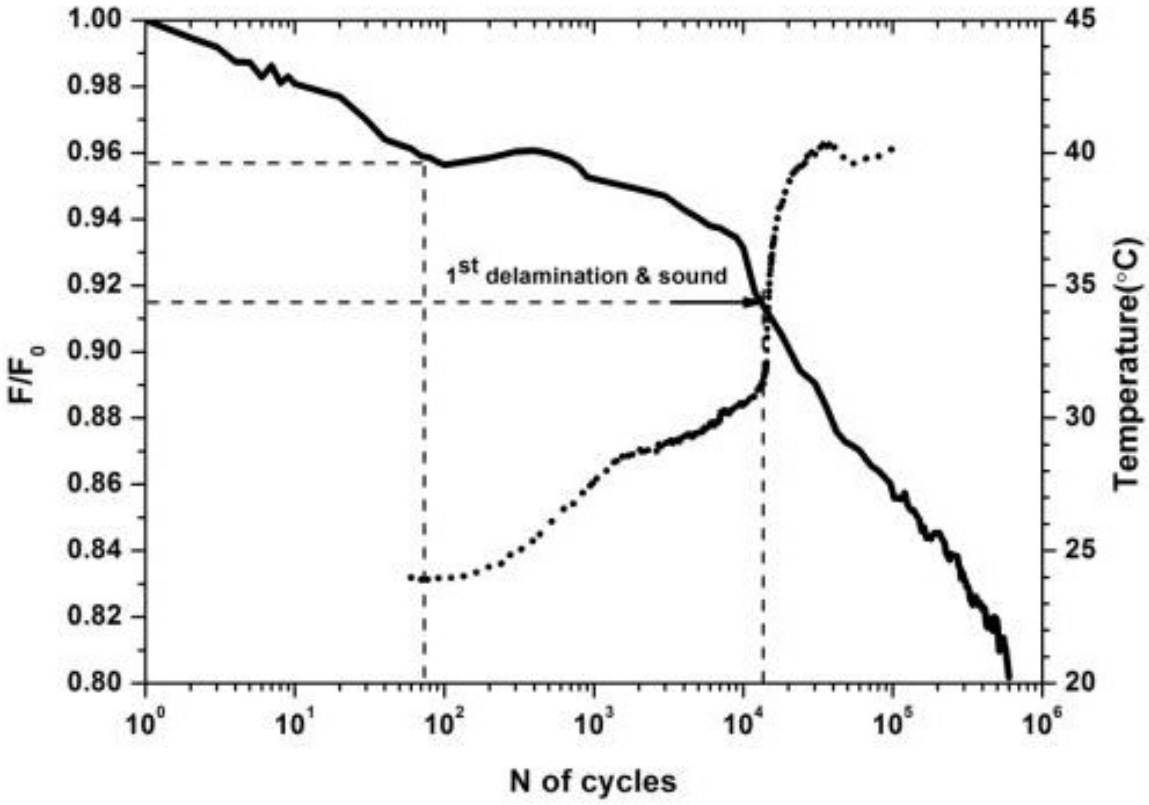


Figure 3.29. Load reduction ratio ($F/F_0$) and temperature increase at 63% deflection level

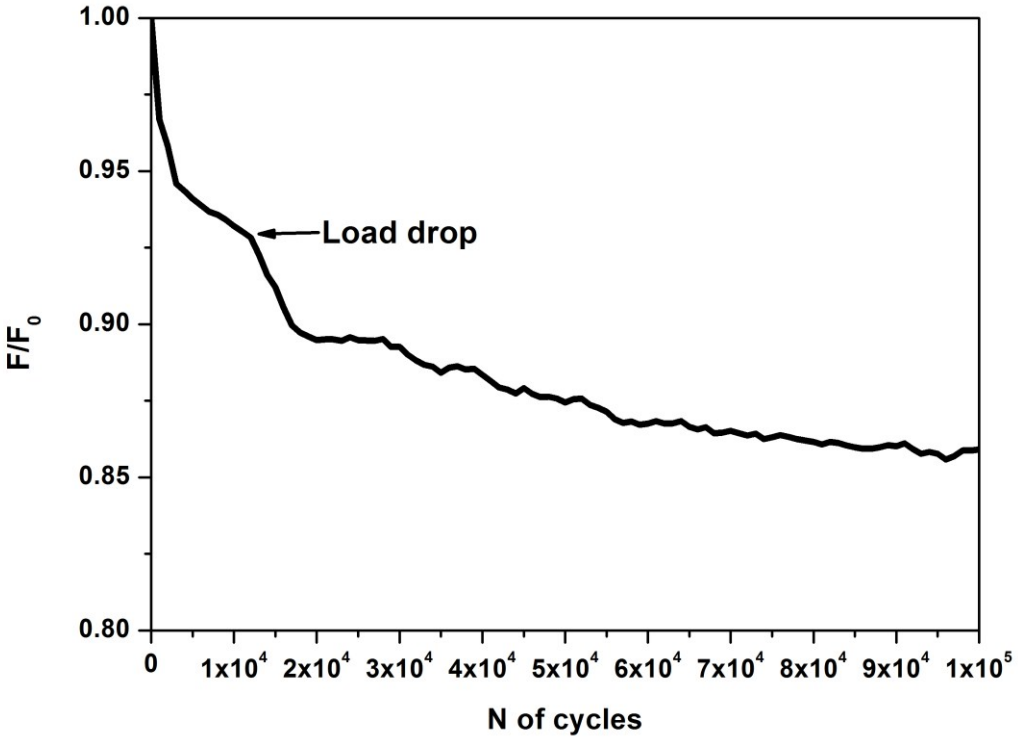


Figure 3.30. The load drop at the first delamination for cross-ply laminate at 63% deflection level

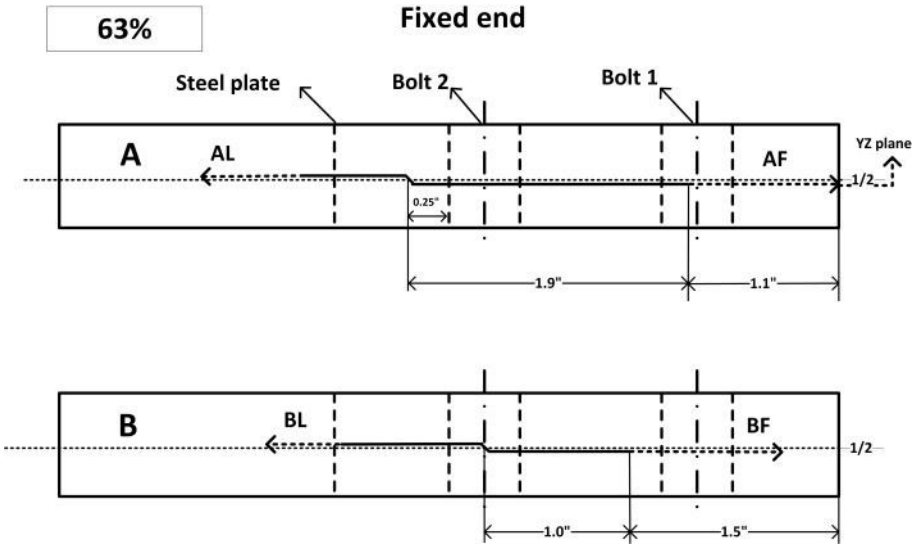


Figure 3.31. Crack location on the side surface of tested specimen at 63% deflection level

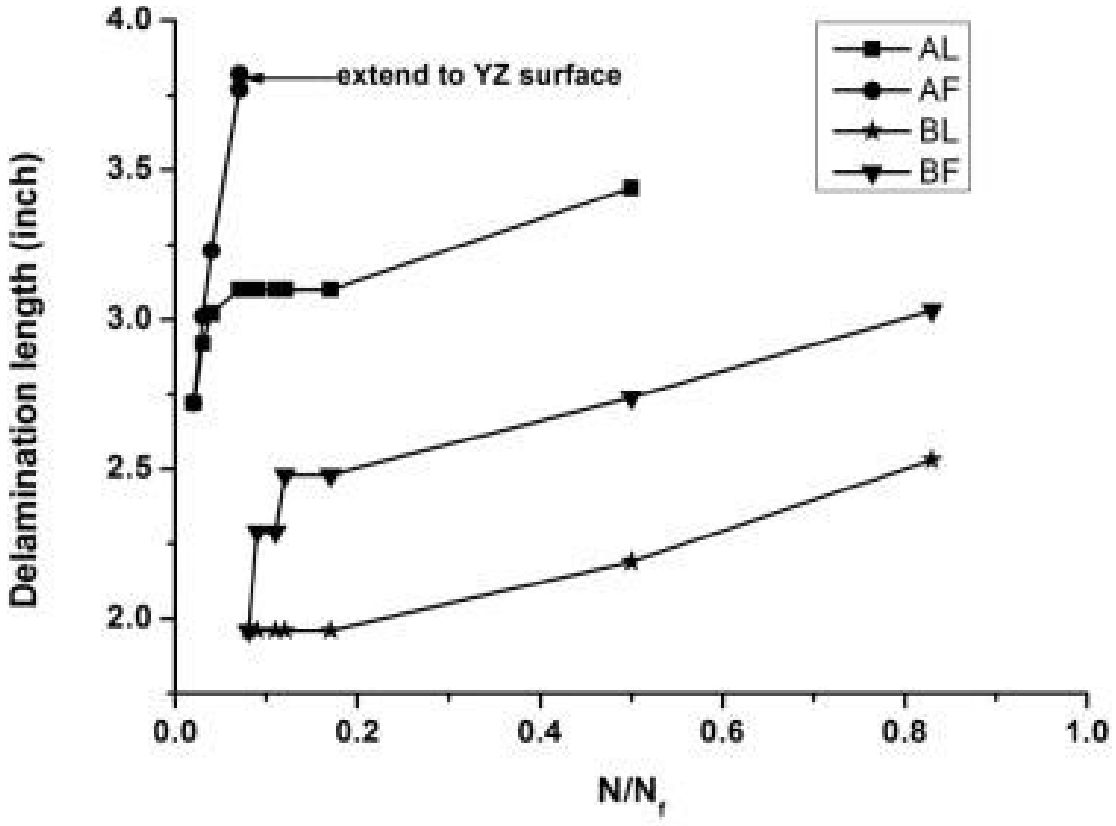


Figure 3.32. Surface crack propagations at 63% deflection level

3.2.2.4 Deflection level 4: 72%

Two replicates of fatigue test were performed at this deflection level. The thermography was conducted on one of the specimens. Figure 3.33 shows the typical curves at 72% level. After the first stage of 5% load dropping caused by the buffer pad debonding, the bending load experienced a continuous decrease of another 3% until the crack initiated at 1000 cycles. The temperature profile started from 400 cycles, it ascended continuously to 42℃. As the cracks propagated, the load continuously decreased until failure. The cracks on side A and side B occurred at almost the same time with similar length as shown in Figure 3.35. In Figure 3.34,

the zig-zag point on side A is 2.9" away from the fixed end, while the zig-zag point on side B is 2.52" away from the fixed end. The propagation of the crack on the surface only occurred during the first half of the fatigue life. The continuing load decrease meant that more delaminations might occur inside. The total fatigue life of this specimen was 170,000 cycles. For another replicated specimen, the first crack initiated at around 500 cycles, and the fatigue life was 160,000 cycles.

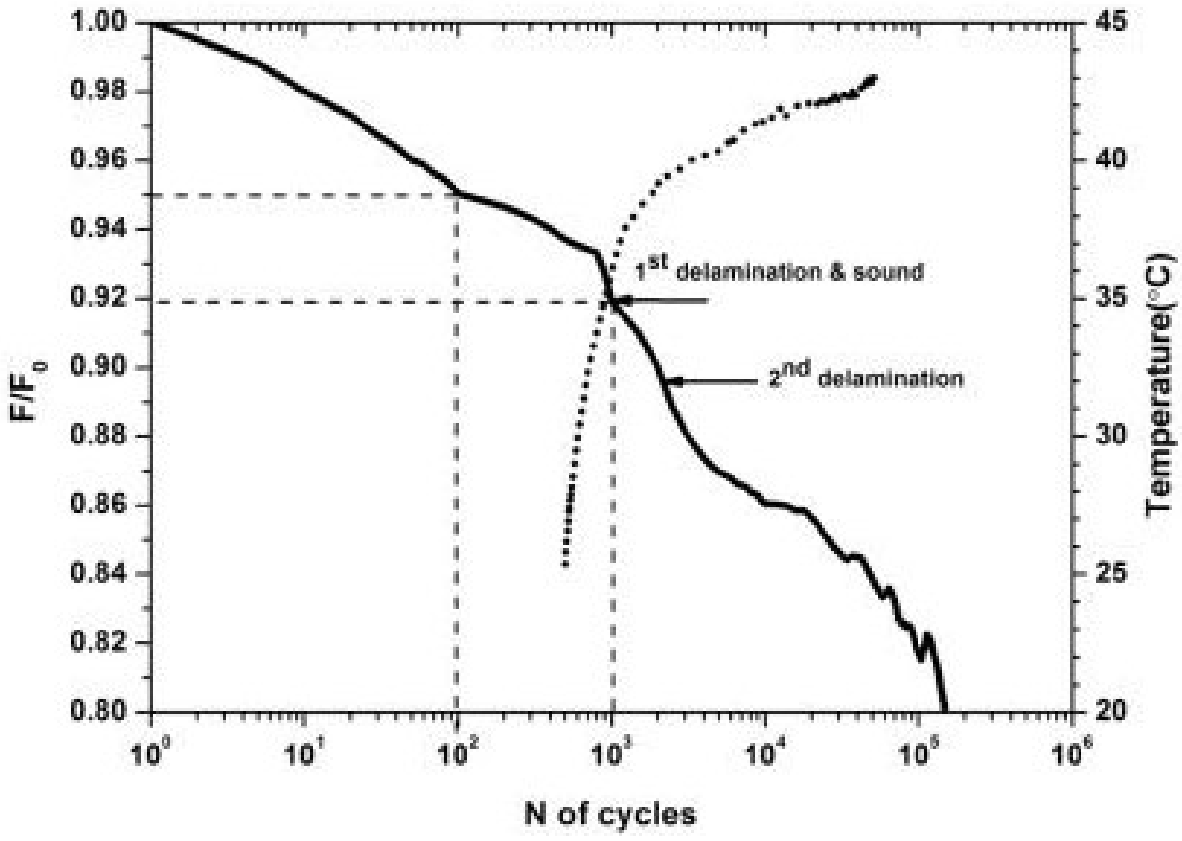


Figure 3.33. Load reduction ratio ($F/F_0$) and temperature increase at 72% deflection level

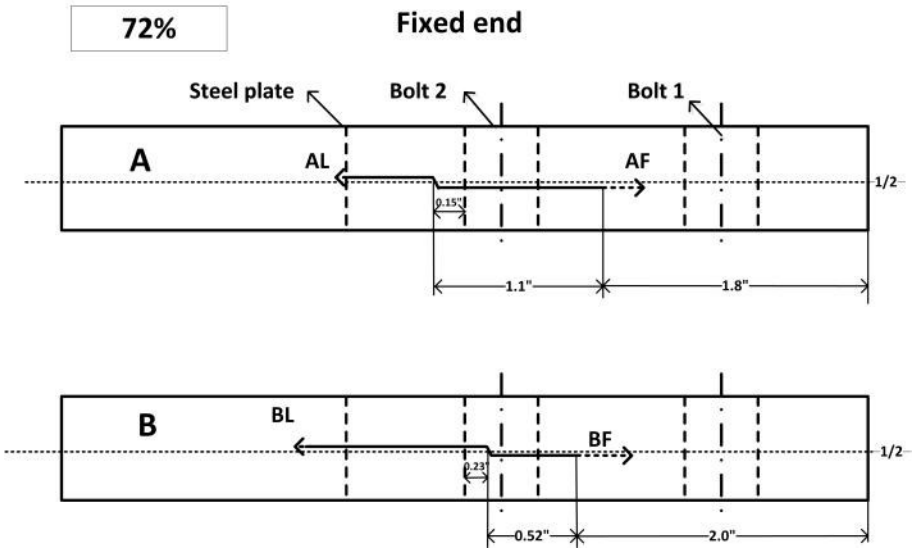


Figure 3.34. Crack location on the side surface of tested specimen at 72% deflection level

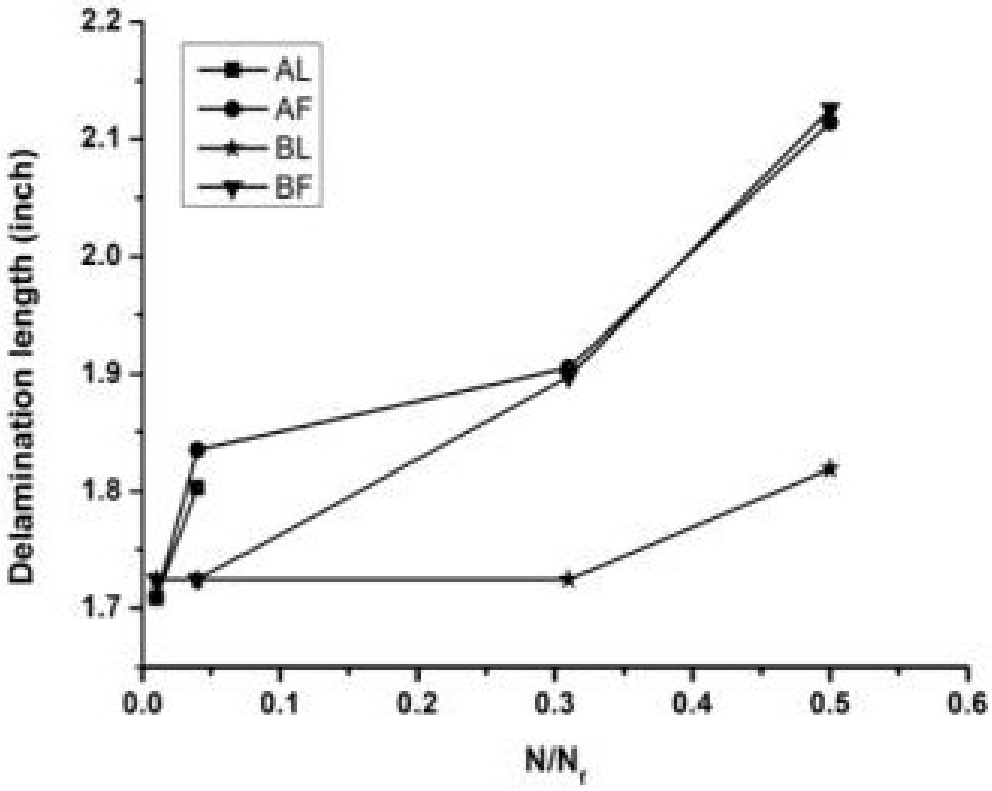


Figure 3.35. Surface crack propagations at 72% deflection level

3.2.2.5 Discussion

In all tested cross-ply specimens, there was no shear-out failure. This is due to the crack resistance of $90°$ fibers. Also for the cross-ply specimens, the appearance of delaminations inhibits shear-out failure as discussed previously.

At the mid-thickness level, the existence of symmetric $90°$ plies made the occurrence of transverse crack caused by interlaminar shear much easier as compared to the stacking of all $0°$ plies in the unidirectional specimen. The tips of the transverse crack induced delaminations at 0/90 interfaces. A zig-zag shaped failure was formed. Whenever the delamination occurred, the propagation rate was reduced by the resistance of $90°$ plies, which resulted in longer fatigue life as compared to the unidirectional specimen at similar deflection displacement. The initial zig-zag points were distributed between $X = 2.9"$ to $X = 3.2"$.

For both unidirectional specimen and cross-ply specimen, the initial length of the delamination did not have a consistent trend with the deflection levels. It depended more on the quality of the damaged area. In the manufacturing process, it is difficult to make a specimen with same qualities everywhere.

3.2.3. **Failure mode**

The optical microscope and digital camera were used to observe the failure modes of the failed test specimens after the fatigue tests. When the unidirectional specimen was subjected to lower stress level, it was possible to run up to high fatigue cycles without initiating a delamination. A shear-out failure in $0°$ layers of the bolted joint occurred as shown in Figure 3.36. This failure mode did not occur in the cross-ply specimens with the same fatigue life.

The existences of 90° fibers resist the crack propagation. When the stress level was higher, the delaminations occurred. For the specimens with delaminations, there were two types of failure mode: delamination and transverse cracks. Figure 3.37 and Figure 3.38 show the failure modes of $[0]_{80}$ specimen. In Figure 3.37, the extra parts at the top and bottom are the bonded buffer pads. The left image in Figure 3.37 presents the delamination on XZ surface. The right one presents the transverse crack on YZ surface. In Figure 3.38, the thickness of one ply is indicated. The left image shows the interlaminar delamination and intralaminar delamination. On the YZ plane, transverse cracks occurred. The cracks of $[0/90]_{20s}$ test specimens as shown in Figure 3.39 and Figure 3.40 have a zig-zag shaped failure. This type of failure mode is common in a sandwich structure under a dynamic three point bend loading[64]. When a sandwich panel was under the flexural response, the impact panel displayed transverse shear failure and delamination. The transverse cracking initially occurred at the core. Once the crack reached the face sheet, it started a delamination along the face-sheet-core interface. The sandwich case was also able to explain the laminate with cross-ply stacking sequences subjected to the similar loading condition. Similar to the core, the initial failure, the transverse crack was due to the high shear stress in the 90° plies. The tips of the crack led to delaminations at the adjacent 0°/90° interffaces. As the loading is continuously applied on the specimen, the concentrated stress on the crack tips led to more transverse cracks in 90° plies and subsequent interface delaminations at other adjacent thickness locations as shown in Figure 3.39.

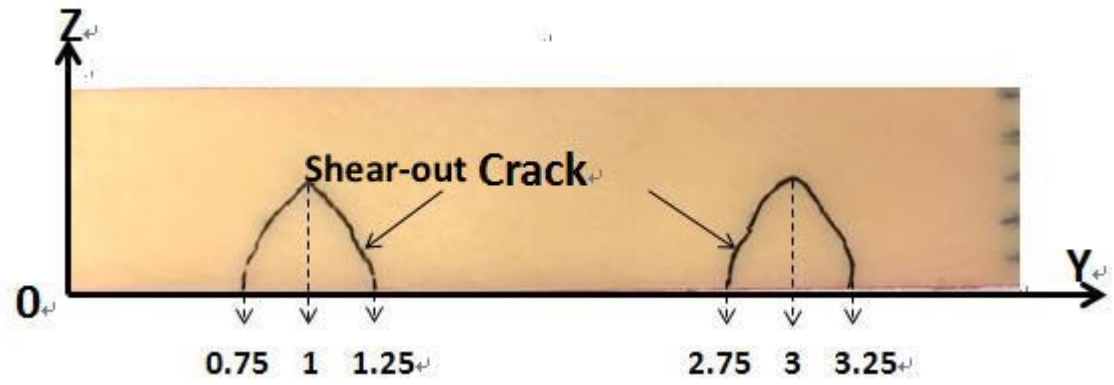


Figure 3.36. Shear-out failure mode of unidirectional specimens at 61% and 65% deflection levels

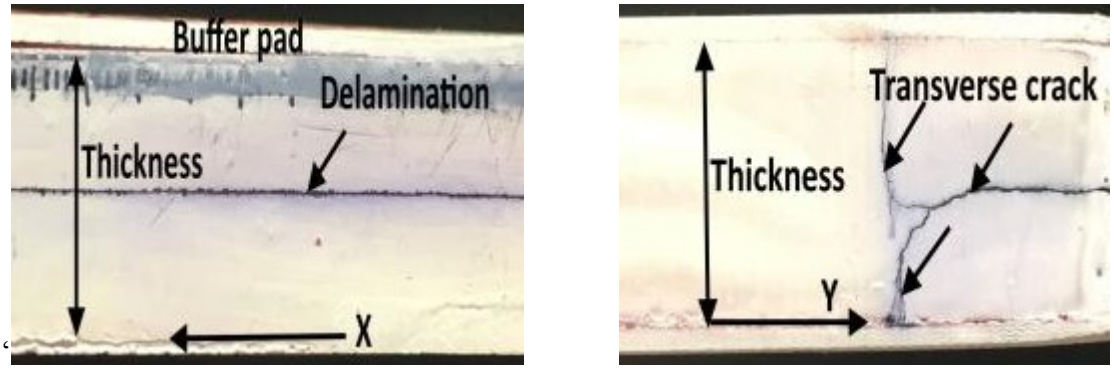


Figure 3.37. Digital images of the cracks of $[0]_{80}$ specimen at sections of $Y = 0.75"$ (left) and $X = 0.5"$ (right)

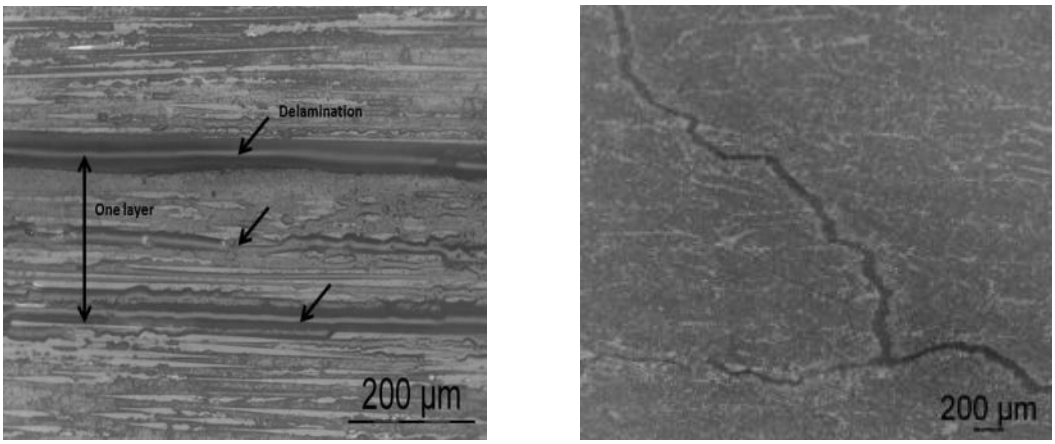

Figure 3.38. Microscopic images of the cracks of $[0]_{80}$ specimen on the XZ surface (left) and YZ surface (right)

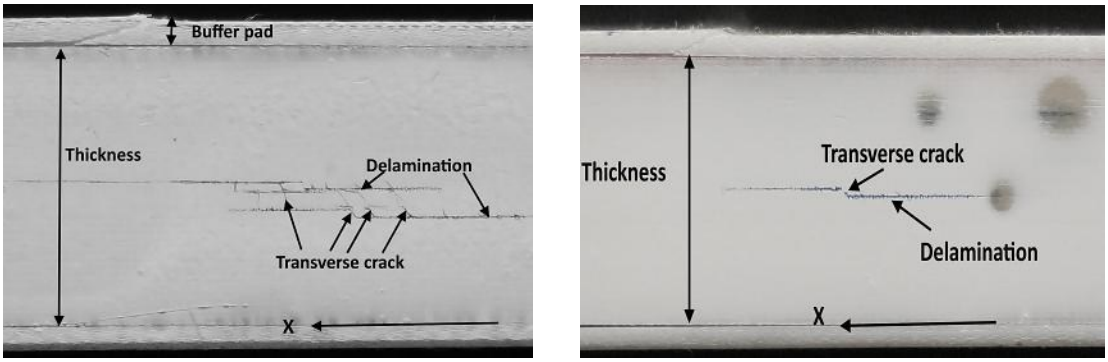


Figure 3.39. Digital images of the cracks of two $[0/90]_{20s}$ specimens at section $Y = 0.75"$

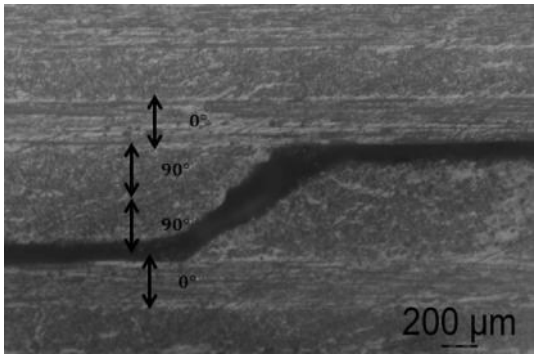


Figure 3.40. Microscopic image of the crack of $[0/90]_{20s}$ specimen

### 3.2.4. **Crack distribution at the damaged section**

Two unidirectional specimens tested at 75% deflection level were sectioned at different Y positions. The delaminations were observed on every XZ cross-sections. In Figure 3.41, each point refers to the through-thickness (Z) location of each delamination on the sectioned cross-sections. On one cross-section, there might be more than one delamination, which comes to several points appearing at one Y position. The dotted lines indicate the positions of the bolted holes. It shows that delamination occurred at different thickness levels. It was in the

range of 33% to 67% of the total thickness. Combining with the previous results of the observed surface delaminations, the delaminations of unidirectional specimens were distributed in the range of 29% to 67% of the total thickness. One of the specimens was then sectioned at $X = 0.7"$ to observe the transverse cracks on YZ plane. By measuring the length of each crack and connecting those cracks together, a 3D crack distribution was obtained as shown in Figure 3.42. It was found that more than one crack initiated at various thickness around the bolted holes area. This was maybe due to the effect of bolt joint. The higher strain was produced when getting closer to the bolted holes. The bolted force caused large deformation in the transverse direction[65]. It could lead to transverse cracks on YZ plane and make the crack travelled more easily along the thickness direction.

The cross-ply specimens at 63% and 72% deflection levels were sectioned along different Y positions. The Z positions of the transverse crack on every XZ cross-section were measured as shown in Figure 3.43. They are mainly distributed at the mid-thickness locations, some cracks around the bolt area occurred at other thickness levels due to the high stress concentration. Figure 3.44 and Figure 3.45 show the X positions of the transverse crack on each XZ cross-section of the tested specimens at 72% and 63% deflection levels. Combining with the transverse crack locations on the XZ surfaces of the other non-destructive tested specimens at 45% and 54% levels, the transverse crack mainly distributed between X=2.1" to X=3.2". From the previous discussion at each deflection level, the initial observed transverse cracks located between X=2.9" to X=3.2". The locations of bolt 1 and bolt 2 are also indicated in the figures. It can be found out that all the transverse cracks initiated around the bolt 2 (X=2.25" to X=2.75"). As a reference, the grip is at X=3.5". At mid-plane, X=3.1" was found to be the maximum interlaminar shear stress location in the static bending stress

analysis[65]. Therefore, the interlaminar shear stress could be considered to have the largest potential of initiating those transverse cracks at mid-plane. After measuring the length of each crack, a 3D distribution is shown in Figure 3.46.

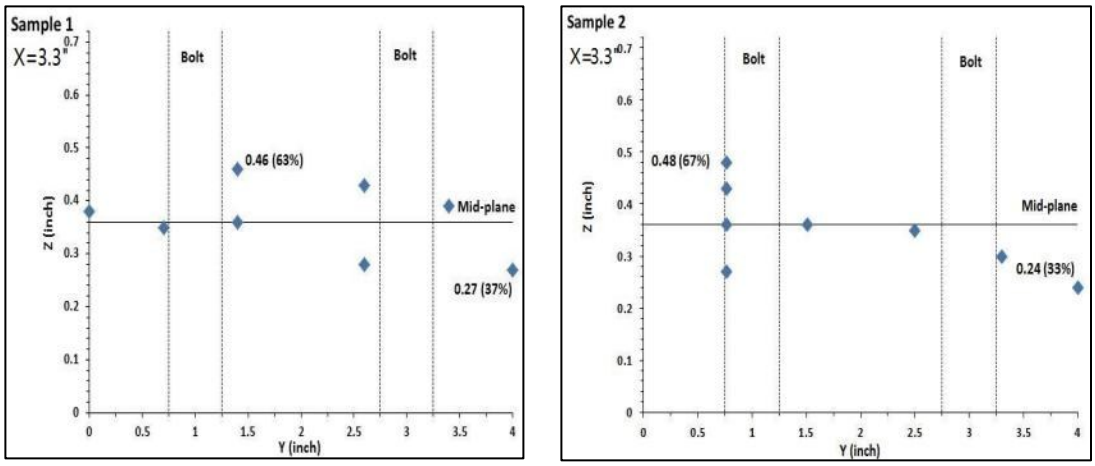


Figure 3.41. Crack through-thickness distribution of two unidirectional specimens at 75% deflection level

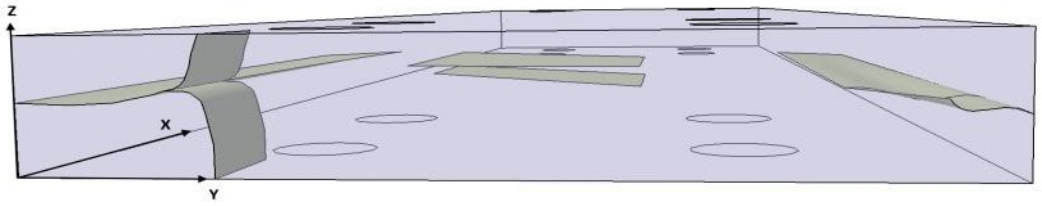


Figure 3.42. Crack 3D distribution of unidirectional specimen at 75% deflection level

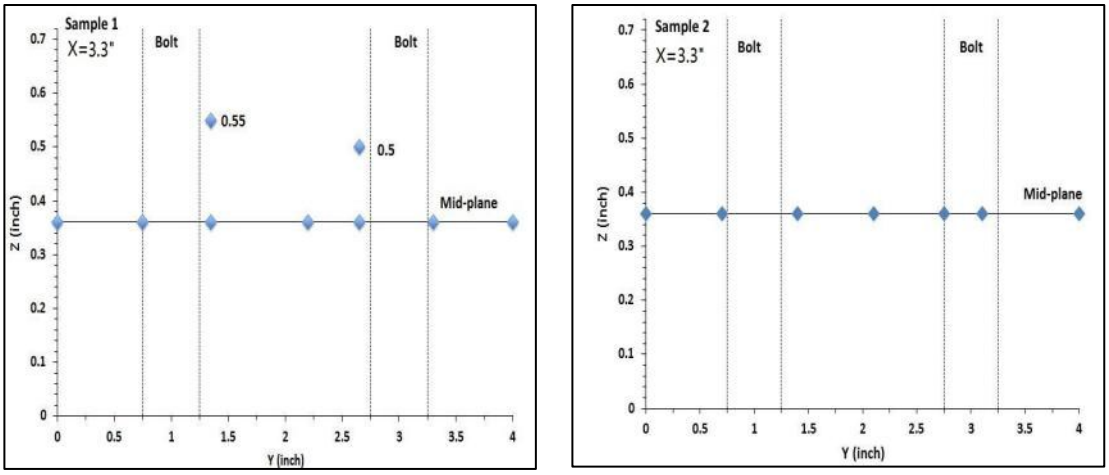


Figure 3.43. Transverse crack through-thickness distribution of cross-ply specimens at 72% deflection level

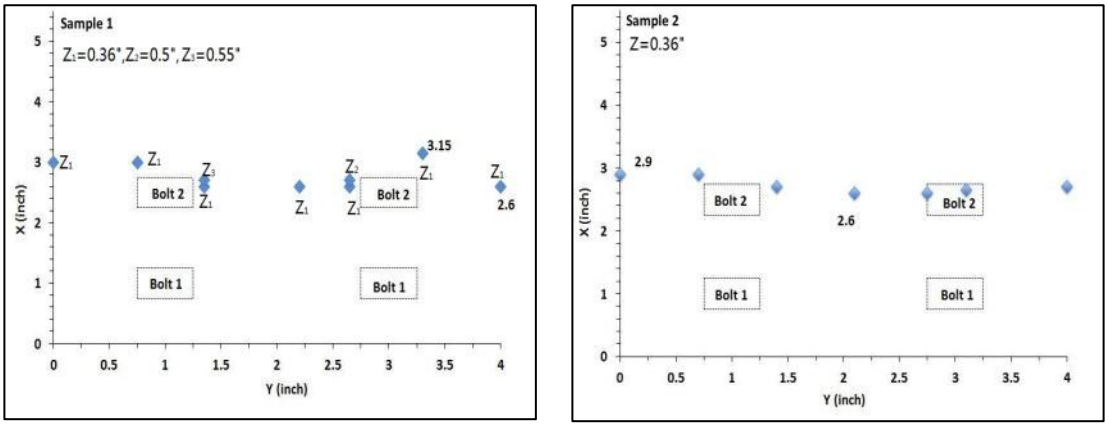


Figure 3.44. Transverse crack distribution along X direction of two cross-ply specimens at 72% deflection level

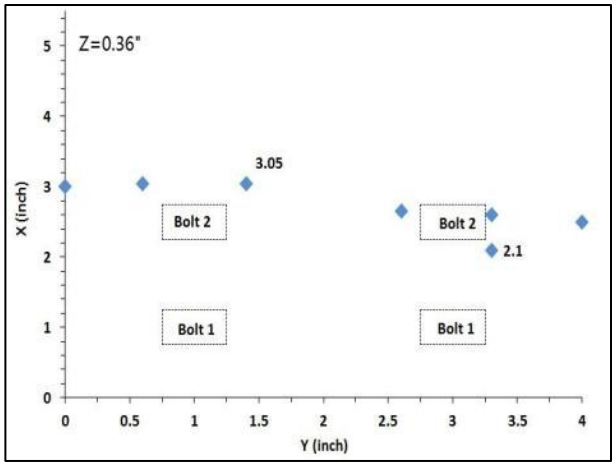


Figure 3.45. Transverse crack distribution along X direction of cross-ply specimens at 63% deflection level

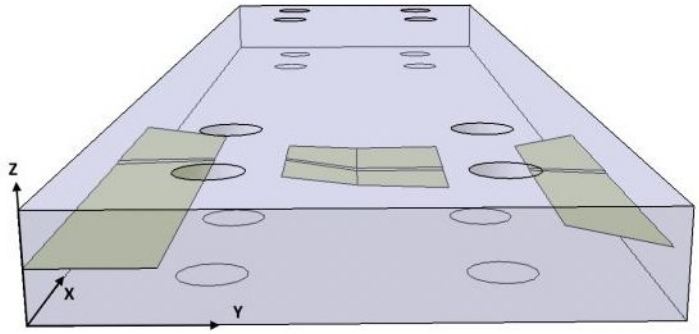


Figure 3.46. Crack 3D distribution of cross-ply specimen at 72% deflection level

## 3.3. Summary

Four deflection levels of flexural fatigue tests were performed on laminates of the stacking sequence $[0]_{80}$ and $[0/90]_{20s}$. When subjected to different deflection levels, the first delaminations were initiated at different periods of the fatigue life. The first delamination here referred to the damage that was visible and caused degradation to the structure stiffness. As the flexural fatigue test in this study was controlled by the displacement, the first delamination initiation cycles of every test specimen with the corresponded specimen displacement are summarized in Figure 3.47. The fatigue life diagram is displayed in Figure 3.48. When the

maximum upward deflection displacement was lower than 17mm, either unidirectional specimen or cross-ply specimen was able to run up to $10^6$ cycles. At the two lower deflection levels, the unidirectional specimens did not initiate delaminations and had fatigue lives up to $10^6$ cycles. The shear-out cracks on YZ plane due to the bolted joint occurred at the lower levels of unidirectional specimens. Compared with the cross-ply specimens at the two relative lower deflection levels, they also had fatigue lives up to $10^6$ cycles, but with delaminations initiated at different periods. At the similar bending displacement, 21.5mm for unidirectional specimen and 21.1 mm for cross-ply specimen, the unidirectional specimen had the first delamination at the same time with the cross-ply specimen but having much shorter fatigue life. The cross-ply stacking sequence had better resistance to the delamination resistance. Table 3.3 gives a summary about the major results of the fatigue tests.

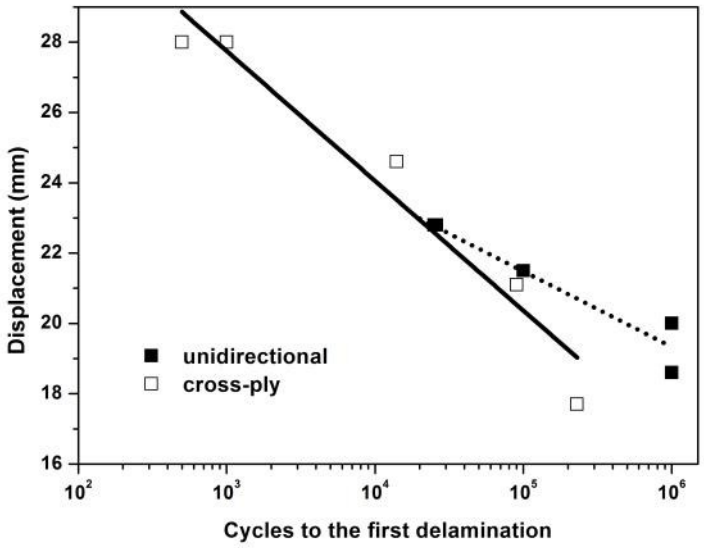


Figure 3.47. Cycles to first crack of $[0]_{80}$ and $[0/90]_{20s}$ test specimens at different displacements

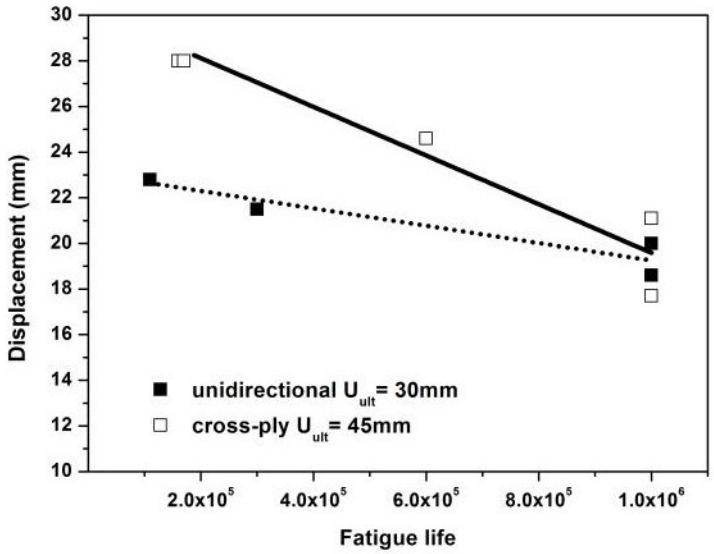


Figure 3.48. Fatigue life diagram of $[0]_{80}$ and $[0/90]_{20s}$ test specimens at different displacements

| $[0]_{80}$ | 61% | 65% | 70% | 75% |
|---|---|---|---|---|
| **Crack initiation** | Not detected | Not detected | 100,000 | Sample 1: 26,000 |
| | | | | Sample 2: 25,000 |
| **Fatigue life (20% load drop)** | $10^6$ | $10^6$ | 300,000 | Sample 1: 110,000 |
| | | | | Sample 2: 110,000 |
| **Initial crack location and length (inch)** | Not detected | | L=1.6" X=1.5" to X=3.1" Z/T= 61% | L=2.5" X=0.9" to X=3.4" Z/T= 53% |
| **Failure mode** | Shear-out crack (variable elevation planes) of bolted joint | | Delamination (same elevation plane) | |
| **Crack distribution (inch)** | X = 2.75" to 5.16" Z/T= 45% to 54% | | Z/T= 29% to 67% | |
| **$[0/90]_{20s}$** | **45%** | **54%** | **63%** | **72%** |
| **Crack initiation** | 230,000 | 90,000 | 14,000 | Sample 1: 1000 |
| | | | | Sample 2: 500 |
| **Fatigue life (20% load drop)** | $10^6$ | $10^6$ | 600,000 | Sample 1: 170,000 |
| | | | | Sample 2: 160,000 |
| **Initial crack location and length (inch)** | L=1.7" X=2.0" to X=3.7" | L=0.47" X=2.7" to X=3.17" | L=2.7" X=1.1" to X=3.8" | L=1.7" X=2.0" to X=3.7" |
| **Failure mode** | Zig-zag shaped failure (transverse crack at middle 90° layers with 0/90 interface delaminations) | | | |
| **Crack distribution** | X = 2.1" to 3.2" Initial transverse crack at: X = 2.9" to 3.2" | | | |

Table 3.3. Summary of fatigue test results

# Chapter 4. Conclusion

In this study, it was possible to manufacture 80 plies glass fiber epoxy laminate following the recommended procedure from the company. It was found that performing debulking process every 3 plies for 5 minutes was effective in removing large and irregular voids before curing for thick laminate. Resin bleeding was an important issue, which needed to be well controlled during the bagging procedure.

A preliminary investigation on the flexural fatigue behavior of thick unidirectional and cross-ply laminates with bolted holes has been done. A clamped-clamped boundary condition was used to perform the bending fatigue tests. Four deflection levels were studied for each stacking sequence. The cross-ply specimens were more flexible than the unidirectional specimens.

During the fatigue test, four stages of load drop were observed: buffer pad debonding, matrix cracking and nucleating, delamination initiation and crack propagation. The thermography was an effective method for in-situ delamination detection by showing obvious temperature increasing trend during the fatigue test. The initiation of a delamination could be detected by four methods: sound, sudden load drop, rapid temperature increase and visual observation.

With the bolted load introduced on the fixed end, cracks preferred to initiate around the bolted holes area. The flexural fatigue behavior and crack distributions of two types of specimens are summarized below:

1) Unidirectional specimens:

- At lower displacement levels, the unidirectional specimens had shear-out cracks

during the long term fatigue cycles ($10^6$ cycles) around the bolted joint. The shear-out cracks in 0° layers initiated around the mid-thickness region (45% to 54% of the total thickness) due to the high interlaminar shear stress and then propagated at the lower part of the laminate, which was subjected to tensile stress.

- At higher displacement levels, the unidirectional specimens had delaminations instead of the shear-out cracks. The delaminations are distributed along the thickness direction in the range of 29% to 67% of the total thickness. The initiated delaminations were near the upper part of the laminate (53% to 61% of the total thickness), which was close to the compressive surface.

2) Cross-ply specimens:

- The cross-ply specimens could initiate a delamination at lower displacement. They did not have the shear-out failure mode when the specimens were also run up to $10^6$ cycles. When delaminations occurred, the cross-ply specimens had better resistance to the delamination propagation than the unidirectional specimens, which gave longer fatigue life.
- The cross-ply specimens had a zig-zag shaped failure mode. A transverse crack initiated at the middle 90° layers. The tips of the transverse crack led to adjacent interface delaminations. Along the longitudinal direction, the transverse cracks are mainly located in the range of 2.1"to 3.2" away from the fixed end, which was the area between the second bolted hole and the grip. The initiated transverse cracks are mainly located between 2.9"to 3.2" away from the fixed end. The interlaminar shear stress has the potential to initiate the transverse crack.

# Chapter 5. Contribution and Future Work

From the experimental work on the thick laminate in this study, the following contributions have been made:

1) The fatigue life diagrams of $[0]_{80}$ and $[0/90]_{20s}$ including the cycles to the first crack were provided. The information can be used to the fatigue life prediction.
2) The failure modes and crack distribution of thick unidirectional and cross-ply laminates under flexural fatigue loading were investigated.
3) Thermography provides a possible way for observing the crack initiation, which can make the experimental results closer to the numerical studies.

For further investigations on this project, the work can be considered from the following aspects:

1) The thermal residual stress of the thick laminate caused by the curing process can be taken into consideration for the further improvement of the specimen mechanical properties.
2) More repeated fatigue tests at variable bending deflection levels can be conducted to complete the diagram of bending displacement with fatigue life. The results from the diagram can be applied to validate fatigue life prediction model.
3) The boundary condition in the present fatigue tests was clamped-clamped. Fatigue tests can be performed under the cantilever boundary condition to compare the fatigue behavior.

# List of papers:

- Wen X and Hoa, S., “Flexural Fatigue Behavior of Thick Glass/Epoxy Composite Flex Beam”, in Proceedings of International Workshop on Mechanical Behavior of Thick Composites. March, 2016, Montreal, Canada, published by DEStech Publications, Inc.
- In preparation of a Journal paper “Flexural Fatigue Behavior of Thick Glass/Epoxy Composiet Beam”.

# Reference:


1. Stringer, L.G., Optimization of the wet lay-up/vacuum bag process for the fabrication of carbon fibre epoxy composites with high fibre fraction and low void content. Composites, 1989. 20(5): p. 441-452.
2. Mouritz, A.P., Ultrasonic and interlaminar properties of highly porous composites. Journal of composite materials, 2000. 34(3): p. 218-239.
3. Hoa, S.V., Principles of the manufacturing of composite materials. 2009: DEStech Publications, Inc. p. 174-175.
4. Bogetti, T.A. and Gillespie, J.W., Two-dimensional cure simulation of thick thermosetting composites. Journal of Composite Materials, 1991. 25(3): p. 239-273.
5. Twardowski, T.E., Lin, S.E., and Geil, P.H., Curing in thick composite laminates: experiment and simulation. Journal of composite materials, 1993. 27(3): p. 216-250.
6. Hojjati, M. and Hoa, S.V., Model laws for curing of thermosetting composites. Journal of composite materials, 1995. 29(13): p. 1741-1761.
7. Kim, J.S., Development of an autoclave cure cycle with cooling and reheating steps for thick thermoset composite laminates. Journal of composite materials, 1997. 31(22): p. 2264-2282.
8. Oh, J.H., Cure cycle for thick glass/epoxy composite laminates. Journal of composite materials, 2002. 36(1): p. 19-45.
9. Young, W.-B., Compacting pressure and cure cycle for processing of thick composite laminates. Composites science and technology, 1995. 54(3): p. 299-306.
10. Olivier, P. and Cavarero, M., Comparison between longitudinal tensile characteristics of thin and thick thermoset composite laminates: influence of curing conditions. Computers & Structures, 2000. 76(1): p. 125-137.
11. Ruiz, E. and Trochu, F., Numerical analysis of cure temperature and internal stresses in thin and thick RTM parts. Composites Part A: Applied Science and Manufacturing, 2005. 36(6): p. 806-826.
12. Bheemreddy, V., Huo, Z., Chandrashekhara, K., and Brack, R.A., Process modeling of cavity molded composite flex beams. Finite Elements in Analysis and Design, 2014. 78: p. 8-15.
13. Bheemreddy, V., Huo, Z., Chandrashekhara, K., and Brack, R.A. Process optimization of composite flex beams using neural networks, in Proceedings of International SAMPE Technical Conference, Society for the Advancement of Material and Process Engineering 2013, Long Beach, California.
14. Zhang, Z. and Friedrich, K., Artificial neural networks applied to polymer composites: a review. Composites Science and technology, 2003. 63(14): p. 2029-2044.
15. El Kadi, H., Modeling the mechanical behavior of fiber-reinforced polymeric composite materials using artificial neural networks—A review. Composite Structures, 2006. 73(1): p. 1-23.
16. Rai, N. and Pitchumani, R., Rapid cure simulation using artificial neural networks. Composites Part A: Applied Science and Manufacturing, 1997. 28(9): p. 847-859.
17. Jahromi, P.E., Shojaei, A., and Pishvaie, S.M.R., Prediction and optimization of cure cycle of thick fiber-reinforced composite parts using dynamic artificial neural networks. Journal of Reinforced Plastics and Composites, 2012. 31(18): p. 1201-1215.
18. Reifsnider, K., Fatigue behavior of composite materials. International Journal of

Fracture, 1980. 16(6): p. 563-583.
19. Pascoe, J.A., Alderliesten, R.C., and Benedictus, R., Methods for the prediction of fatigue delamination growth in composites and adhesive bonds–a critical review. Engineering Fracture Mechanics, 2013. 112: p. 72-96.
20. Stelzer, S., Brunner, A.J., Argüelles, A., Murphy, N., and Pinter, G., Mode I delamination fatigue crack growth in unidirectional fiber reinforced composites: Development of a standardized test procedure. Composites Science and Technology, 2012. 72(10): p. 1102-1107.
21. Stelzer, S., Brunner, A.J., Argüelles, A., Murphy, N., Cano, G.M., and Pinter, G., Mode I delamination fatigue crack growth in unidirectional fiber reinforced composites: Results from ESIS TC4 round-robins. Engineering Fracture Mechanics, 2014. 116: p. 92-107.
22. Brunner, A.J., Stelzer, S., Pinter, G., and Terrasi, G.P., Mode II fatigue delamination resistance of advanced fiber-reinforced polymer–matrix laminates: Towards the development of a standardized test procedure. International Journal of Fatigue, 2013. 50: p. 57-62.
23. Sims, J.L., Tisdale, P.R., and Powell, E.A., Composite flapping flexure, U.S. Patent No. 6,708,921. 23 Mar. 2004.
24. LaIonde, S. Investigation into the Static and Fatigue Behaviour of A Helicopter Main Rotor Yoke Made of Composite Materials. 2000. Master thesis: McGill University, Montréal.
25. Cairns, D.S., Mandell, J.F., Scott, M.E., and Maccagnano, J.Z., Design and manufacturing considerations for ply drops in composite structures. Composites Part B: Engineering, 1999. 30(5): p. 523-534,http://dx.doi.org/10.1016/S1359-8368(98)00043-2.
26. Botting, A.D., Vizzini, A.J., and Lee, S.W., Effect of ply-drop configuration on delamination strength of tapered composite structures. AIAA journal, 1996. 34(8): p. 1650-1656.
27. Muni, G.B., Salpekar, S.A., and O'Brien, T.K., Fatigue delamination onset prediction in unidirectional tapered laminates. Composite Materials: Fatigue and Fracture (Third Volume), 1991. 1110: p. 312.
28. Murri, G.B., O'Brien, T.K., and Salpekar, S.A., Tension fatigue of glass/epoxy and graphite/epoxy tapered laminates. Journal of the American Helicopter Society, 1993. 38(1): p. 29-37.
29. Hoa, S.V., Daoust, J., Du, B.L., and Vu‐Khanh, T., Interlaminar stresses in tapered laminates. Polymer Composites, 1988. 9(5): p. 337-344.
30. Daoust, J. and Hoa, S.V., Parameters affecting interlaminar stresses in tapered laminates under static loading conditions. Polymer Composites, 1989. 10(5): p. 374-383.
31. Fish, J.C. and Lee, S.W., Delamination of tapered composite structures. Engineering Fracture Mechanics, 1989. 34(1): p. 43-54.
32. Shim, D.-J. and Lagace, P.A., Mechanisms and structural parameters affecting the interlaminar stress field in laminates with ply drop-offs. Journal of composite materials, 2006. 40(4): p. 345-369.
33. Samborsky, D.D., Wilson, T.J., Agastra, P., and Mandell, J.F., Delamination at Thick Ply Drops in Carbon and Glass Fiber Laminates Under Fatigue Loading. Journal of Solar Energy Engineering, 2008. 130(3): p. 031001-031001,10.1115/1.2931496.
34. Murri, G.B., O'Brien, T.K., and Rousseau, C.Q., Fatigue life methodology for tapered

composite flexbeam laminates. Journal of the American Helicopter Society, 1998. 43(2): p. 146-155.
35. Murri, G.B., Schaff, J.R., and Dobyns, A.L. Fatigue and damage tolerance of a hybrid composite tapered flexbeam, in Proceedings of American Helicopter Society, Forum. 2001.
36. Murri, G.B. and Schaff, J.R., Fatigue life methodology for tapered hybrid composite flexbeams. Composites Science and Technology, 2006. 66(3–4): p. 499-508,http://dx.doi.org/10.1016/j.compscitech.2005.06.010.
37. Pawar, P.M. and Ganguli, R., On the effect of progressive damage on composite helicopter rotor system behavior. Composite Structures, 2007. 78(3): p. 410-423.
38. S.Vali-shariatpanahi, Determination of through thickness properties for composite thick laminate in ICCM17. 2009: Edinburgh, Scotland.
39. Schubel, P.M., Luo, J.J., and Daniel, I.M., Through-thickness characterization of thick composite laminates. Society for Experimental Mechanics, 2006.
40. Daniel, I.M., Luo, J.-J., Schubel, P.M., and Werner, B.T., Interfiber/interlaminar failure of composites under multi-axial states of stress. Composites Science and Technology, 2009. 69(6): p. 764-771,http://dx.doi.org/10.1016/j.compscitech.2008.04.016.
41. Daniel, I.M., Luo, J.-J., and Schubel, P.M. Mechanical and Failure Characterization of Textile Composites, in Proceedings of 16th International Conference on Composite Materials (ICCM16). 2007.
42. Daniel, I.M., Cho, J.M., Werner, B.T., and Fenner, J.S. Mechanical behaviour and failure criteria of composite materials under static and dynamic loading, in Proceeding of 17th international conference on composite materials (ICCM17). 2009, Edinburgh, UK.
43. Govender, R.A., Louca, L.A., Fallah, A.S., Pullen, A., and Nurick, G.N., Determining the through-thickness properties of thick glass fibre reinforced polymers at high strain rates. Journal of Composite Materials, 2011: p. 0021998311415444.
44. Park, D.C. and Lee, D.G., Through-thickness compressive strength of carbon–phenolic woven composites. Composite Structures, 2005. 70(4): p. 403-412,http://dx.doi.org/10.1016/j.compstruct.2004.09.001.
45. Kim, B.C., Park, D.C., Kim, B.J., and Lee, D.G., Through-thickness compressive strength of a carbon/epoxy composite laminate. Composite Structures, 2010. 92(2): p. 480-487,http://dx.doi.org/10.1016/j.compstruct.2009.08.032.
46. Bing, Q. and Sun, C.T., Specimen size effect in off-axis compression tests of fiber composites. Composites Part B: Engineering, 2008. 39(1): p. 20-26,http://dx.doi.org/10.1016/j.compositesb.2007.02.010.
47. DeTeresa, S.J., Freeman, D.C., and Groves, S.E., The effects of through-thickness compression on the interlaminar shear response of laminated fiber composites. Journal of composite materials, 2004. 38(8): p. 681-697.
48. Lim, T.S., Kim, B.C., and Lee, D.G., Fatigue characteristics of the bolted joints for unidirectional composite laminates. Composite Structures, 2006. 72(1): p. 58-68,http://dx.doi.org/10.1016/j.compstruct.2004.10.013.
49. Khashaba, U.A., Sallam, H.E.M., Al-Shorbagy, A.E., and Seif, M.A., Effect of washer size and tightening torque on the performance of bolted joints in composite structures. Composite Structures, 2006. 73(3): p. 310-317,http://dx.doi.org/10.1016/j.compstruct.2005.02.004.
50. Gorjipoor, A., Ganesan, R., and Hoa, S., Effect of Washer Size and Clamping Torque on

Thick Composite Bolted Joints, in CANCOM Canadian International Conference on Composite Materials. 2015: Edmonton, Alberta, Canada.
51. Gorjipoor, A., Ganesan, R., Hoa, S.V., and Shadmehri, F. Stress Analysis of a Thick Composite Laminate with a Bolted Joint, in Proceedings of the Tenth Joint Canada-Japan Workshop on Design, Manufacturing and Applications of Composites. 2015, Vancouver, Canada, published by DEStech Publications, Inc.
52. Boey, F.Y.C. and Lye, S.W., Effects of vacuum and pressure in an autoclave curing process for a thermosetting fibre-reinforced composite. Journal of materials processing technology, 1990. 23(2): p. 121-131.
53. Koushyar, H. Effects of variation in autoclave pressure, cure temperature, and vacuum-application time on the porosity and mechanical properties of a carbon/epoxy composite. 2011. Master thesis: Wichita State University.
54. Mamani, S. and Hoa, S.V. Temperature Measurement in Autoclave Manufacturing Process for Thick Glass/Epoxy Composite Laminate in Proceedings of International Workshop on Mechanical Behavior of Thick Composites. March, 2016, Montreal, Canda, published by DEStech Publications, Inc.
55. Standard, A., D2584-11, 2000. Standard Test Method for Ignition Loss of Cured Reinforced Resins. ASTM International.
56. Standard, A., D2734 - 09, 2009. Standard Test Methods for Void Content of Reinforced Plastics. ASTM International.
57. Sartorius. User's Manual. Density Determination Kit; Available from: www.sartorius.com.
58. Chambers, A.R., Earl, J.S., Squires, C.A., and Suhot, M.A., The effect of voids on the flexural fatigue performance of unidirectional carbon fibre composites developed for wind turbine applications. International Journal of Fatigue, 2006. 28(10): p. 1389-1398,http://dx.doi.org/10.1016/j.ijfatigue.2006.02.033.
59. Heer, C.S., Flexural Test Set Up, in Project report 2013, Mechanical Engineering, Concordia University.
60. Fortin-Simpson, J., Static Flexural Bending Behaviour of Thick Glass/Epoxy Laminates, in Project report 2015, Mechanical Engineering, Concordia University.
61. Fortin-Simpson, J., Gorjipoor, A., and Hoa, S. Effect of Boundary Conditions on the Cantilever Bending of Thick Glass Fiber Reinforced Polymer (GFRP) Composite Plates, in Proceedings of International Workshop on Mechanical Behavior of Thick Composites. March, 2016, Montreal, Canada, published by DEStech Publications, Inc.
62. A. R. Bezazi, a.A.E.M., b J.-M. Berthelot,b and B. Bezzazi, Flexural Fatigue Behavior of Cross-Ply Laminates: An Experimental Approach. Strength of Materials, 2003. 35(2).
63. Gorjipoor, A.,Private communications,2016.
64. Thorsson, S.I., Xie, J., Marek, J., and Waas, A.M., Matrix Crack Interacting with a Delamination in an Impacted Sandwich Composite Beam. Engineering Fracture Mechanics, 2016,http://dx.doi.org/10.1016/j.engfracmech.2016.04.003.
65. Gorjipoor, A., Finite Element Modeling of Thick Composite Laminate Subjected to Bolt Joints and Flexural Bending Loads, in Project report 2015, Mechanical Engineering, Concorida University.